Dynamic Modeling of Two-Phase Heat and Vapor Transfer Characteristics in a Gas-to-Gas Membrane Humidifier for Use in Automotive PEM Fuel Cells

by

Alan Dunlavy

A thesis submitted to the Graduate Faculty of
Auburn University
in partial fulfillment of the
requirements for the Degree of
Master of Science

Auburn, Alabama
December 18, 2009

Approved by

Song-Yul Choe, Chair, Associate Professor of Mechanical Engineering
Sushil Bhavnani, Professor of Mechanical Engineering
Daniel Mackowski, Associate Professor of Mechanical Engineering
Lewis Payton, Associate Research Professor of Mechanical Engineering

Abstract

Due to the recent negative outlook on the availability of cheap, long term energy supplies from non-renewable resources, several technologies have been proposed and revisited as possible solutions to the current energy crisis. Along with alternative fuels, such as ethanol and biofuels, and clean energy resources, such as wind and solar power, Hydrogen proton exchange membrane (PEM) fuel cells have been seen as one of these options capable of replacing fossil fuels for power, especially in the automotive industry.

However, because the technology is relatively new in comparison to combustion engines, there are many unique problems that must be overcome in order for it to be considered a viable substitute. One of the most concerning issues with the PEM fuel cell is its membrane water production and management. When the chemical reaction takes place in the fuel cell, liquid water is produced, which must be removed in order for the fuel cell to continue functioning and maintain a high level of performance. However, there are typically two situations that arise due to poor water management: flooding and dehydration. Flooding occurs under a heavy load (high power output) when the fuel cell generates an excess of water which blocks air channels within the gas diffusion media, causing poor performance. Conversely, dehydration occurs as a result of severe drying of the membrane due to imbalance between water take-up and back diffusion. This is also

bad for fuel cell performance since the membrane needs to be humidified in order to maintain proton transfer. Thus, the humidifier has come to be seen by researchers as a regulation device, capable of supplying water to the membrane under many different electrical loads and input conditions.

In this study, the background and current state-of-the-art of the membrane humidifier are discussed with special attention paid to heat and vapor transfer phenomena. In addition, a model is proposed that describes the operation of the humidifier and predicts its response to various inputs such as humidity, flow rate, and temperature. Lastly, several static and dynamic experiments are undertaken to simulate the real-world operations of the humidifier and were used for comparison with the results of the model.

Acknowledgements

The author would like to thank Dr. Song-Yul Choe for his constructive advice and guidance in regards to both research and study in the graduate program at Auburn University. Additional thanks are extended to Dr. Sushil Bhavnani, Dr. Daniel Mackowski, and Dr. Lewis Payton for offering their spare time, support, and even materials throughout the research process. Special thanks are given to the author's colleagues, Jong-woo Ahn and Jinglin He, who spent countless hours in the office assisting his modeling efforts along with Jiahua Li, who donated much of his time during the experiments.

Finally, the author would like to thank his parents, without whom a healthy appreciation for learning of all kinds would not have been realized. Their encouragement and support has been nothing less than priceless.

Table of Contents

List of Figures

List of Tables

Nomenclature

Alphabets:		*Units*
A	Area	m^2
a	Water activity	
b	Constant	
B	Baffle spacing	m
C	Mass Concentration	kg/m^3
D	Diameter	m
E	Energy	Joules
f	Friction Factor	
G	Mass Velocity	$kg/(m^2\ s)$
H	Enthalpy	kJ/kg
h	Heat Transfer Coefficient	$W/(m^2\ K)$
I	Pumping Power	W
Ja	Jakob number	
k	Thermal Conductivity	W/(m K)
L	Length	m
M	Mass	kg
$\dot{m}$	Mass Flow Rate	kg/sec
N	Number of Tubes	
Nu	Nusselt number	
P	Tube Pitch or pressure	m or kPa / atm or W

Pr	Prandtl number	
Q	Heat transfer rate	W
R	Thermal Resistance	K/W
r	Radius	m
Ra	Rayleigh Number	
Re	Reynolds Number	
RH	Relative Humidity	%
S	Wetted Perimeter	m
T	Temperature	K or ^{o}C
t	Thickness	m
U	Overall Thermal Resistance	K/W
V	Fluid Velocity	m/s
V'	Volumetric Flow Rate	l/min
u	Internal energy	Joules
x	Axial location	m

Greek Symbols:

λ	Water Content	
ρ	Density	kg/m^3
μ	Dynamic viscosity	Pa s
ν	Kinetic viscosity	m^2/s
ω	Humidity ratio	

Superscripts, subscripts:

1	In
2	Out

avg	Average
c	Cross-Sectional
cond	Condensation
cv	Control volume
d	Diagonal
D	Characteristic Length
e	Equivalent
h	Hydraulic
i	Tube-Side
L	Longitudinal
l	Liquid
m	Mass
max	Maximum
mem	Membrane
o	Shell-Side
S	Longitudinal
sat	Saturation
T	Transverse
trans	Transfer
u	Internal Energy
v	Vapor
xf	Cross flow
z	Shell-Side or Tube-Side

1. INTRODUCTION

In recent years the demand for clean, renewable energy has become an important political, economic, and social topic not only in the United States, but also throughout the world as the demand for energy steadily increases and its non-renewable supply is continuously expended. This trend is no more evident than in the commitment of current research into such industrial technologies as wind, solar, and geothermal power, along with carbon-reducing techniques, to name a few. However, for consumer (and to a lesser extent commercial) automotive purposes which constitute a significant portion of energy consumption, much of the research has been conducted with the purpose of examining the feasibility of alternative fuels like ethanol or bio-fuels in combustion engines and hydrogen in proton exchange membrane (PEM) fuel cells, the latter of which is of interest in this paper. This relatively new technology is intended to either completely replace the combustion engine altogether or be used as an auxiliary power source by which the efficiency of other available technologies can be increased.

1.1. MOTIVATION OF CURRENT RESEARCH

The appeal of the fuel cell in the context of the energy situation is its high efficiency relative to the internal combustion engine (ICE), which, being a heat engine produces a lot of waste heat. Whereas the ICE, which includes the bio-fuel and ethanol-

fueled variants, uses a combustion process generating heat to propel the vehicle, the fuel cell uses a purely chemical reaction to power an electric motor along with all of the other electrical loads of the vehicle. Furthermore, because the byproducts of the reaction are water and heat, the fuel cell is highly desirable when compared to the ICE from both an engineering and environmental standpoint. However, as is the case with most of the alternative power technologies available today, the PEM fuel cell suffers from a lack of long term real-world application and is thereby prone to problems that limit its use and effectiveness as an alternative to the more widely used heat engine. At the forefront of these troubles is the difficulty of maintaining the proper hydration level in the polymer membrane, which is essential to the operation of the fuel cell. Thus, the impetus for the research into the gas-to-gas membrane humidifier is to gain technical knowledge into its workings so that its use as a vital component of the PEM fuel cell system can be realized and make the hydrogen fuel cell a viable alternative to traditional power devices.

1.2. OUTLINE OF RESEARCH OBJECTIVES

Current research conducted at the Auburn University Advanced Propulsion Laboratory involves the formulation of an improved mathematically and thermodynamically relevant model of a gas-to-gas tube-and-shell type humidifier intended to be used in PEM fuel cell applications. Whereas previous modeling has included the use of relatively basic thermodynamic relations, the new study seeks to obtain the heat and vapor transfer characteristics of the humidifier experimentally and propose a new model that more closely reflects the real-world operation of the device while also improving the relations and assumptions that are used. The model can then be

compared to previous simulation results and the experimental data in order to demonstrate its superiority.

In addition, there are several types of data that must be collected in order to effectively explain the unique characteristics of the humidifier:

1. Wet outlet temperatures and relative humidity
2. Total heat and mass transfer rates
3. Tube and shell-side pressure drop calculation

As a result of the research, a new model is proposed that more accurately explains the complex nature of the humidifier and can be used to predict and evaluate how changes to the design or operating conditions of the device affect its performance.

2. LITERATURE REVIEW

2.1. BACKGROUND

The membrane in a fuel cell is typically made of a polymer known as Nafion™ which is a proprietary material of the Dupont Company. This material, arranged along with other thin materials in what is known as a stack, allows the transfer of protons that are produced from the oxidation of hydrogen on the anode side of the stack, while inhibiting the passage of its electrons. The phenomenon by which this occurs is due to the Nafion™'s makeup, which is a sulfonic acid (SO_3H) that allows protons in the membrane to travel from one acid site to another because they are lacking in protons due to their chemical composition. Thus, the membrane material is very conductive of cations and resistive to electrons [33] . In turn, the electrons that do not pass through the membrane can be routed to an electric motor to drive the wheels of a vehicle. Meanwhile, the protons that pass through the Nafion™ eventually exit the membrane and make contact with a flow of air on the opposite side of the membrane. The oxygen in the air then combines with the protons that have passed through causing water to form. Under normal, static conditions the water can be removed without much difficulty and the production of electricity can be sustained. However, due to the fluctuating nature of the requirements of the automotive fuel cell (in the form of variable motor load) the amount of water produced changes often so that, without a control device, the membrane either

floods or dehydrates, both of which are highly detrimental to the function and performance of the fuel cell.

The first situation occurs when the current density in the fuel cell is increased and the amount of water on the cathode side becomes large. The resulting elevated water content is commonly known as *flooding* and can block the gas flow channels, thereby limiting the amount of oxygen that can reach the membrane to continue the reaction. Alternately, stack *dehydration* occurs when load is decreased without an increase in humidity in the air flow on the cathode side of the membrane. In this case, the membrane water content is reduced to a point at which the membrane can no longer sustain proton transport. Therefore, the root interest of the research in question has been focused on the technical understanding of the membrane gas-to-gas humidifier which is intended to effectively and efficiently maintain the proper humidity level within the membrane of the fuel cell stack.

2.1.1. PRINCIPLES OF FUEL CELL OPERATION

In order to appreciate the appeal of the fuel cell it is important to realize how the device works with respect to the combustion engine, which it is intended to replace. The fuel cell reaction function is a purely chemical process which involves no moving parts and produces a source of electrical energy that can be used by an electric motor for propulsion or for any other load that the vehicle might require. The fuel, hydrogen, is provided on one side of a proton exchange membrane (or PEM) which, as the name suggests, allows the passage of protons while at the same time inhibiting the passage of

electrons. On the other side of the membrane, oxygen is reduced in the catalyst layer to form water.

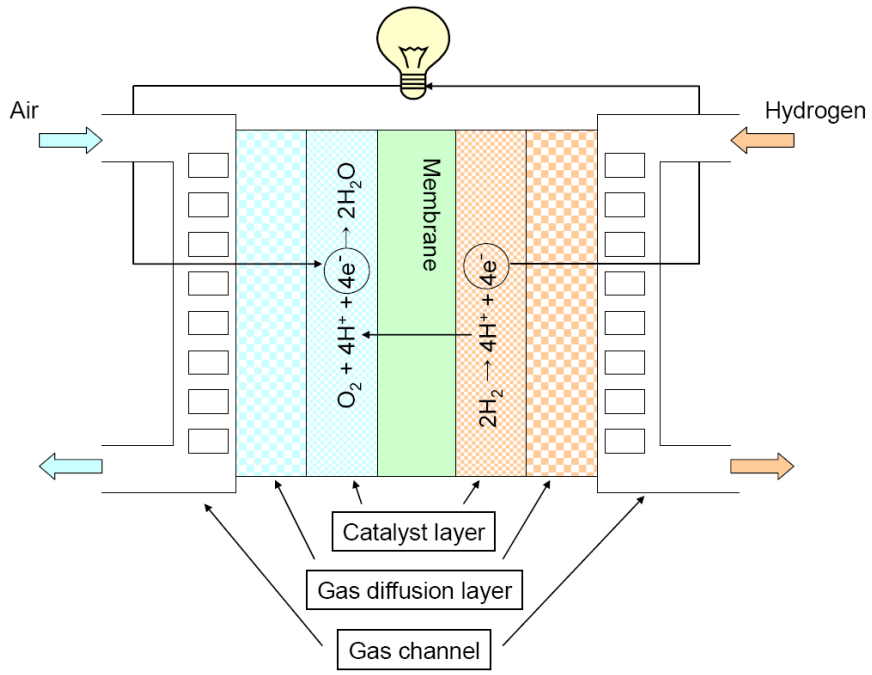

Figure 1 PEM Fuel Cell Diagram [1]

Most recently, this has been accomplished using a fluorocarbon polymer referred to as Nafion™ because of its superior proton exchange properties at the operating conditions typically seen by the hydrogen fuel cell.

Although the fuel cell reaction can take place using a single membrane, the typical fuel cell design consists of multiple cells, arranged back-to-back and connected in series so that the electrical power of the total system is augmented. This arrangement is collectively referred to as a stack since the individual cells are stacked next to each other, producing a modular device that can be used in specific power generation applications. The greater the power demand from the fuel cell, the larger the number of cells is needed.

2.1.2. COMPONENTS OF SYSTEM

Typically, the stack consists of four main components, applied to each cell in the system: the gas channels, gas diffusion layers, catalyst layers, and membrane [1]. The gas channels are located in the bipolar endplates, which serve as a housing for the fuel cell stack and also transport the reactant gases to and from the location of the chemical reaction. Currently, this component is most often made out of graphite, making up a substantial fraction of the total weight of the stack [2]. However, there is also research being done so that an alternative material, such as metal foam, could replace this and decrease weight and cost significantly (see Section 2.2.1). After the endplates, the reactants are transported through the gas diffusion layer so that they may be dispersed evenly towards the catalyst layer. Finally, at the catalyst layers, the oxidation and reduction of the reactants occur so that the protons are produced and transported through the membrane.

However, these components describe the makeup of the fuel cell itself which is described extensively in other studies. More relevant, and central to this thesis, are the fuel cell components responsible for the air supply which consist of the stack, gas-to-gas humidifier, and blower.

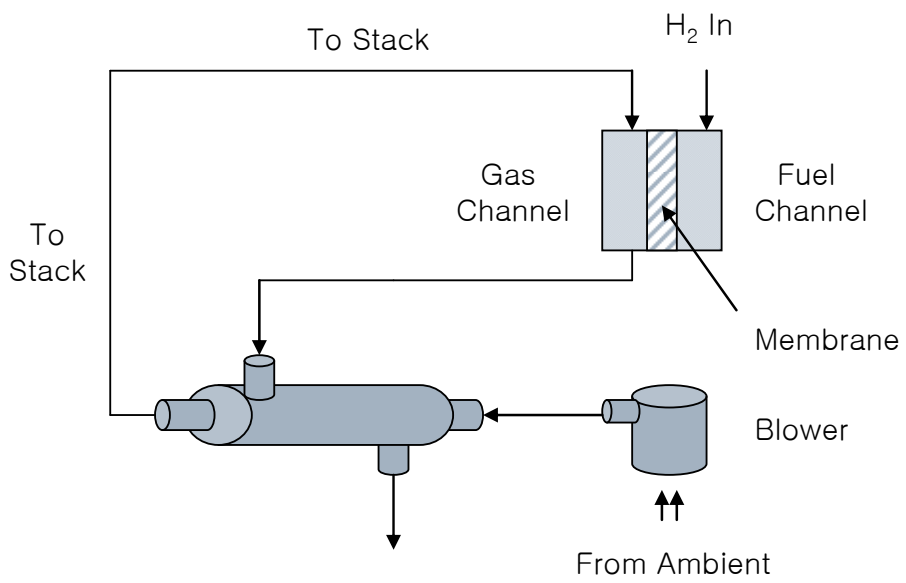

Figure 2: Location of Humidifier in Fuel Cell System

As described in Figure 2, the blower is used to provide the bulk flow of air to the humidifier so that the heat and vapor exchange takes place. In fact only one blower is required since the ambient air going into the humidifier will eventually enter back into it in what is known as the exhaust channel. Nonetheless, the air from the blower will enter into the humidifier where it is heated and humidified by the air coming from the fuel cell. After leaving the humidifier, the air is then at a specific temperature and humidity that is in theory suitable for the stack reaction to continue. The air then enters the fuel cell, where it comes into contact with the membrane and combines with the hydrogen protons from the fuel channel. From there, the process is completed when the air again enters the humidifier to humidify the incoming dry air.

2.2. HUMIDIFICATION TECHNOLOGY

Due to its overwhelming effect on the performance of the fuel cell, the water content in the membrane is a key area of concern in the design and modeling of the fuel cell system. As early as 1993, researchers such as Nguyen, et al [3], were beginning to outline the need for a water management system to maintain a proper level of humidity within the membrane of the stack.

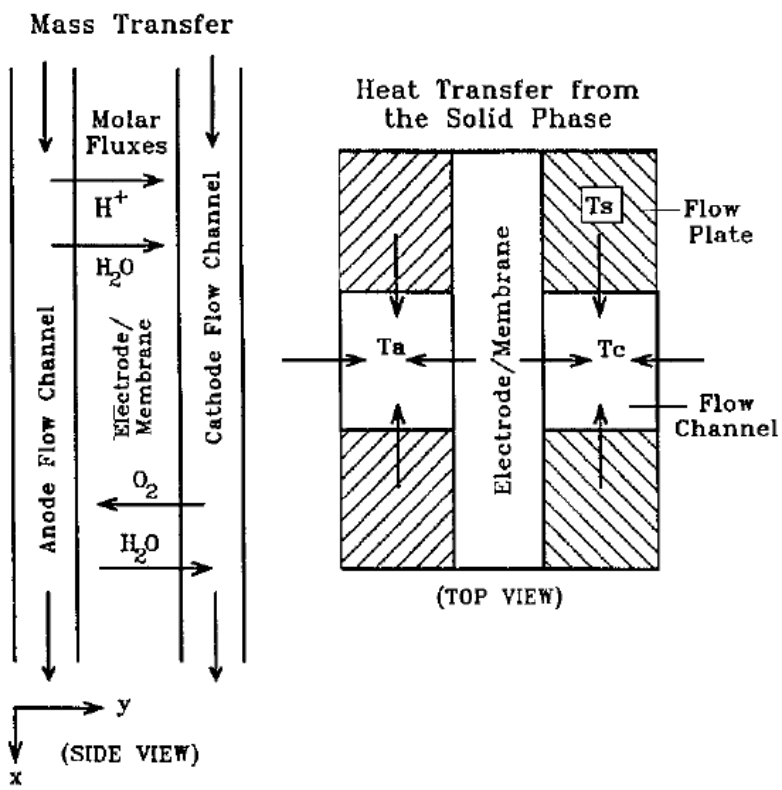

Figure 3: Proton Movement and Back Diffusion in Membrane [3]

Results from that study, along with others, noted that as the current density of the fuel cell increases, the amount of water generated on the cathode side increases as well as the rate of back diffusion toward the anode side. Furthermore, moisture content in the

membrane is directly related to the proton conductivity in the membrane. When the proton conductivity increases in the membrane, a high ohmic overpotential results whereby heat generation occurs in the membrane and power is produced. Moreover, and to the point, since the uptake of protons is dependent upon membrane moisture, an additional regulatory device is required to control the relative humidity of the air flow to ensure that the transfer of moisture out of the membrane is neither too great nor too small.

With this in mind, many different technologies have been proposed to deal with the problem of maintaining the ideal stack moisture content. They can be classified into two main categories: *internal* and *external* to the system, and two sub-categories, *active* and *passive*, indicating the component's ability to regulate its own performance.

2.2.1. INTERNAL METHODS

Obviously, the concept of internal humidification involves a situation where the PEM fuel cell is adequately humidified without the use of any external device. This situation generally results in a simple humidification process when compared to various external methods, while the effectiveness of such a setup is typically reduced when compared to the latter. In this area of research, there are three main technologies that exist:

In 1996, M. Watanabe, et al [4], explored the possibility of *self-humidification* for PEM fuel cells. Because back diffusion was a problem for fuel cells with large membrane thicknesses, there has been research into fuel cells with thinner, more efficient membranes that can decrease the effects of back diffusion. However, as the membrane

thickness is decreased, uncontrolled crossover of hydrogen protons becomes a problem. Thus, the self-humidification technology works by dispersing nanocrystallites of platinum and hydroscopic oxides of TiO or SiO into the membrane to help suppress the crossover effects of fuel cells with thin membranes. However, while this method is simple to do, it is difficult to control, is generally applicable for only low power and temperature situations, and causes a dry-out effect in the membrane at elevated load requirements.

Another method researched is the *absorbent wicks humidification* technique whereby excess humidity located in the fuel cell exhaust gas stream is wicked over to the entering dry reactant gas. In his paper, Ge [5] investigated the possibility of using materials such as polyvinyl alcohol (sponge), absorbent cotton cloth, and absorbent cotton paper to achieve the humidification. The results of the research gave a viable alternative to other methods by being self-regulating and the PEM fuel cell with the method was stable under high current densities when dry H_2 and air were fed. However, the drawbacks of such a design were that the method tends to make the complete sealing of the fuel cell a problem and the wicks will not absorb water once saturation is reached. Thus, the method appears to improve general water distribution throughout the fuel cell, while being limited to situations where the wicks remain below saturation.

Similarly, with *metal foam humidification*, it is possible to achieve humidification of both the air and hydrogen with the use of specifically-designed materials. Kumar, et al [2], looked into the possibility of replacing conventional materials in the bipolar endplates of the fuel cell to reduce the cost and weight of the total system and allow for enhanced self-humidification in the process by reducing the permeability of the material.

The reasons for the research stemmed from the fact that the graphite endplates currently used in fuel cells account for up to 80% of the total weight of the stack and are very time consuming and costly to produce. So, with the use of new, lightweight materials such as metal foams, the job of the endplates and humidification of the reactant gases can be done for less time and money. Furthermore, a recent U.S. Patent [6] has noted very high thermal conductivity using the foam (as high as 187 W/mK) that lends itself to greater heat transfer efficiency. Unfortunately, the main drawback of such a method is the corrosion of metal in the foam and the limited reduction in permeability that makes the material desirable.

However, a very similar technology exists with the same advantages as the metallic foam, except that the material is graphite, which does not suffer from the corrosion problems that the metal foam does [7]. Again, the advantage of the material is that it is very lightweight, while serving the same purpose as the traditional structure typically used in fuel cell stacks today.

2.2.2. EXTERNAL METHODS

Research into the field of external humidification appears to have been the overriding topic in recent years due to a large amount of papers being available within the past decade. Devices of this type use some means of indirectly managing the water within the fuel cell with some external architecture. While most of these mechanisms are capable of sufficiently humidifying the fuel cell, they tend to be more complicated when compared to their internal counterparts. Nonetheless, they are among the most promising

techniques available in the future to make fuel cells realistic alternatives to current technologies and consist of eight main methods:

The concept of *dew point humidification* (or *bubbling*) was discussed by Evans in his 2003 publication [7]. The straightforward method consists of air that is bubbled into a container of water, which causes it to become saturated when it leaves the chamber. Although the method is capable of producing a very high dew point at low gas flow rates, the effect is diminished at higher flow rates. Furthermore, the control of temperature and humidity, especially at the mentioned high flow is not very controllable. This fact, along with the method's need for a reservoir of water, makes its use as a humidification technique largely limited to experimental work.

In the same paper, Evans discussed also the methods of *evaporation humidification* as well as *steam injection humidification*. The evaporation humidification method (alternately referred to as liquid injection) involves the insertion of high pressure atomized water into the pipes entering the gas and fuel channels via fogging nozzles. The pipe then enters an expansion chamber where strip heaters are used to again heat the now vapor/air mixture. However, the method suffers from the same problems as the bubbling technique and also incurs complications due to its piping apparatus. Likewise, the steam injection (or vapor injection) method is done in a similar way—water is heated until it turns into steam and is passed along to the gas channels of the fuel cell. Because the air is delivered in the vapor phase the gas temperatures and humidity are easy to control, do not lose heat due to evaporation, and can be used for larger fuel cell systems. Unfortunately, the method suffers from parasitic energy consumption to produce the steam and is costly relative to the previously mentioned external designs.

Wood, et al [9], proposed a method of *direct water injection with interdigitated channels* in which specifically designed channels are used to directly inject water into the flow channels in order to precisely control their humidity levels. As it turns out, this technique is extremely effective in managing the water content in the fuel cell membrane. As opposed to conventional injection of water, the interdigitated channels provide higher fuel cell efficiency due to superior hydration of the membrane (and subsequently high conductivity) as water comes into direct contact with the anode/membrane interface. Also, the tolerance for excess injected water is increased using the design and the excess water may be used for other purposes, such as evaporative cooling if necessary. However, similar to the normal water injection scheme, the method is made less desirable by requiring a tank for water and depending on a complicated design scheme to achieve its purpose.

Another external humidification involves the use of an *enthalpy wheel* that seeks to absorb moisture from the air exiting the fuel cell and transfer it to the relatively dry air entering the fuel cell. The method was discussed in Carlson's, et al [10], publication regarding the cost analysis of a complete fuel cell system.

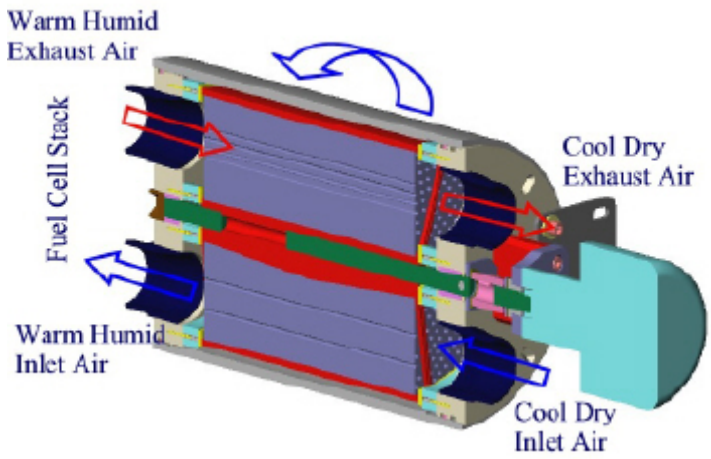

Figure 4: Enthalpy Wheel Diagram [10]

As seen in Figure 4, the device employs the use of an electric motor to turn the housing of a desiccant capable of absorbing and distributing humidity in the presence of vapor gradients. The material exchanges both latent and sensible heat between the two flows of air, which are separated by face seals. As opposed to some of the previous technologies listed, the enthalpy wheel enjoys very good operation and a compact design. Furthermore, Radov, et al [11], notes that pressure drop within the device is typically quite low, which is one of its positive attributes. On the other hand, the main drawbacks to such a system are that the reactant gases should be preheated and that a motor is required to physically turn the wheel and exchange vapor and heat.

Similar to the enthalpy wheel is the membrane humidifier, which can take a variety of forms. The *plate type membrane humidifier* is one that consists of sandwiched membranes that contain various flow channels for the humid and dry air flows [12]. A typical feature of these types of humidifiers is the sliding plate, which can be used to control the heat and humidity going into the fuel cell. Thus, instead of there being

essentially two flows of air, the sliding plate can block one of those channels and transfer heat with one channel and vapor with the other.

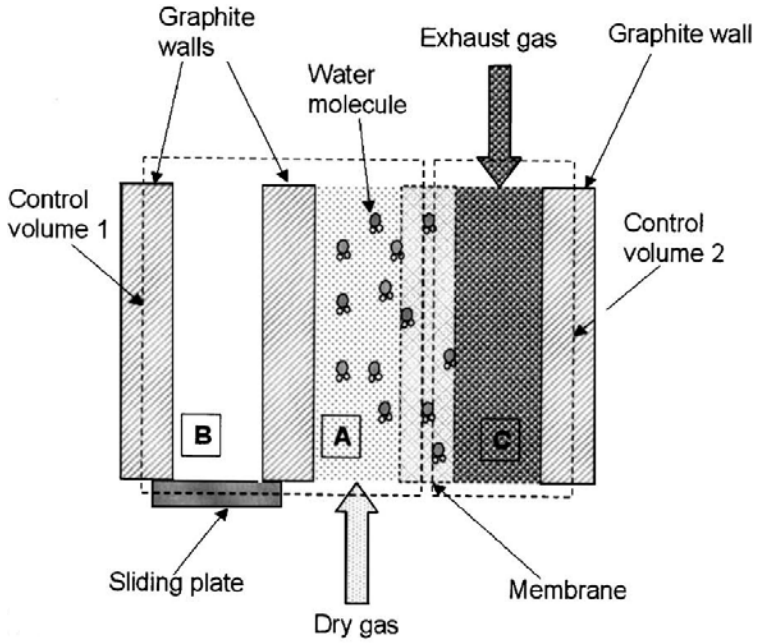

Figure 5: Plate Humidifier Diagram [13]

The main advantages of the plate type humidifier are that, other than the sliding plate, it requires no moving parts, no additional energy, and no additional control architecture.

The *liquid-to-gas membrane humidifier* is another variation of the overall membrane humidifier scheme. In this method a membrane separates a flow of liquid and gas, whereby the liquid humidifies the dry gas channel that is routed towards the fuel cell. This type of device is pretty straightforward in its design and it is quite capable of humidifying dry gas to near saturation at high flow rates [14], but there are several drawbacks to its real-world application. Just as other humidification techniques using water as a humidifier suffered from complexity and added weight, so does the liquid-to-

gas humidifier. Because the water must be circulated on one side of the membrane, a reservoir and pump are needed, making the system less than ideal for lightweight applications such as automotive fuel cells. Additionally, a heater is needed to keep the water at a high temperature due to heat loss due to phase change within the membrane and there is a significant possibility of leakage if the system is not sealed properly.

On the other hand, the *gas-to-gas membrane humidifier* suffers from none of those drawbacks that the previous device does. Zhang, et al [15], notes that the gas-to-gas variant works in much a similar way as a typical heat exchanger, but with the metal walls replaced with the *hydrophilic* Nafion™ membrane. Its advantages as a heat and vapor exchanger include the fact that it requires no moving parts, no additional energy input, and works quickly under normal circumstances. In addition, the membrane humidifier is capable of being used as a heater for the fuel cell stack when subzero conditions exist. As the reaction in the fuel cell begins, heat is generated which travels to the exhaust channel of the humidifier. Then, due to heat transfer between the tube-side and shell-side of the device, the outlet air is both heated and humidified so that the air going back into the fuel cell can be used to increase the temperature further. This type of heat scavenging is another positive aspect of the gas-to-gas humidifier. For these reasons, and the fact that it does not require costly or heavy equipment to operate, the gas-to-gas humidifier is seen by many as the most efficient method of fuel cell humidification available.

2.2.3. ACTIVE AND PASSIVE CONTROL

A humidifier with passive control does not utilize any sort of external control to maintain membrane moisture content within the stack. The idea in this type of setup is

that the humidifier itself is the regulating component in the system whereby the heat and vapor going into the fuel cell (out of the humidifier) is directly dependent upon the heat and vapor coming out of the fuel cell (into the humidifier). Thus, the ability to regulate the heat and humidity in the fuel cell is ultimately limited by the steady-state operation of the fuel cell at a specific flow rate. This limitation is due to the fact that the flow rates of the exhaust inlet and dry inlet are always approximately equal for a given fuel cell power output. Furthermore, because neither the wet outlet temperate nor humidity is able to be changed very rapidly, control systems of this sort tend to have very long response times to changes in fuel cell outlet temperature and humidity. Figure 6 represents this type of control.

On the other hand, active control describes a situation in which the performance of the device, such as the humidifier, is dependent not upon the performance of the fuel cell but rather on either a user input or input via some sort of designed control architecture. In the case of the fuel cell humidifier, the active control component is a bypass valve which can be used to vary the flow rate of the exhaust inlet (fuel cell outlet). When the valve opens, some of the air coming from the fuel cell is routed out of the system into the ambient so that only a specific fraction of the total air flow makes its way back to the humidifier exhaust inlet. Moreover, because the humidifier outlet conditions are significantly affected by the inlet flow rates, the wet outlet humidity and temperature can be quickly and directly controlled by the programmed use of the bypass valve. In fact, the outlet humidity and temperature are proportional to the exhaust inlet flow rate so that when it decreases, the wet outlet humidity and temperature decrease as well.

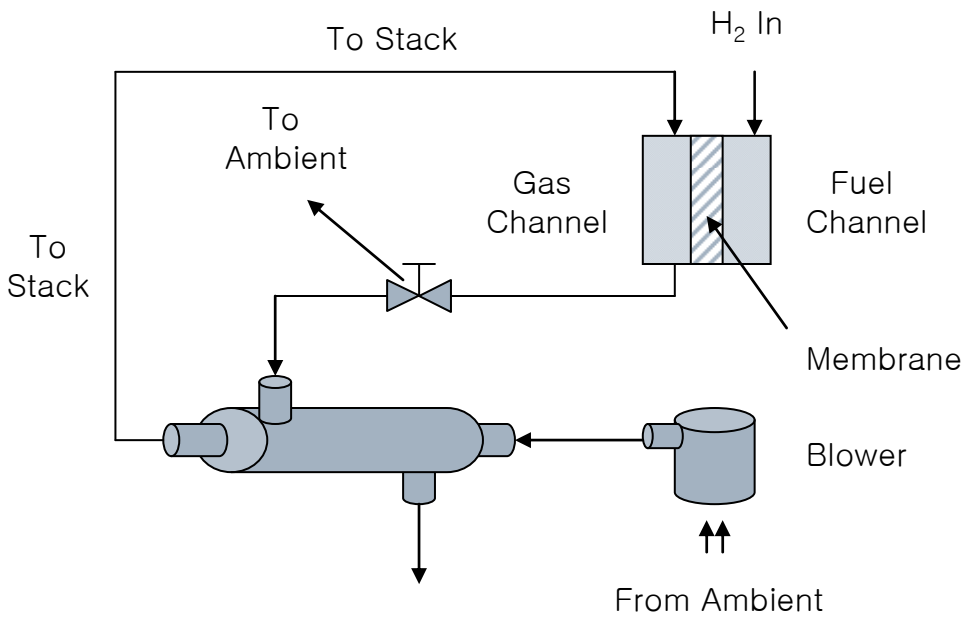

Figure 6: Diagram of Actively-Controlled Exhaust Flow Rate

**Note the bypass valve in the middle of the figure that is used to vary the exhaust inlet flow rate.

2.2.4. GAS-TO-GAS HUMIDIFIER

While the technologies described above each have their own positive and negative attributes, the tube and shell membrane humidifier has proven to be one of the most suitable for the automotive application. Specifically, the gas-to-gas membrane humidifier is of interest in this paper due to its superior qualities for the equipment requirements, which include heating and humidifying air for the fuel cell with minimal power and space consumption. Among its attributes is its ability to efficiently and accurately maintain proper fuel cell membrane humidity using no moving parts, no additional power supply,

and no required user input. Interestingly, the device uses the same membrane material as is used in the PEM fuel cell, only utilized in a different manner. Whereas the fuel cell membrane is used to transport protons from the anode side to the air side of the stack, in the humidifier the Nafion™ functions as a heat and vapor exchanger by using gradients of the energy and mass to drive the respective transport phenomena.

However, in contrast to its liquid-to-gas counterpart, the gas-to-gas humidifier conducts moisture in the vapor phase rather than the liquid phase, meaning that any liquid water that is present at the wet outlet should be a result of condensation within the tube-side channel or piping alone. Additionally, since the heat and vapor mass transfer occur via essentially chemical processes (as in the PEM fuel cell), the device does not need any mechanical means to physically transport the energy or mass, making the gas-to-gas humidifier the most practical technology for the management of membrane humidity in automotive fuel cell applications.

2.2.4.1. DESIGN

Due to its being partly a heat exchange device, the design of the membrane humidifier closely resembles that of many common heat exchangers that would be found in industrial applications. Among the main categories of exchangers are the tube-and-annulus (which consists of a *single* tube inside of a larger diameter annulus), plate type (consisting of sandwiched plates with channels for air flow), and shell-and-tube. While the latter is the design type used in this study, all humidifiers consist of some inlet and

outlet flow channels which correspond to the humid air flow and the air flow that is to be humidified.

The internal flow path, henceforth denoted as the tube or tube side, actually consists of several hundred very small tubes, randomly spaced and located in the membrane material. During humidification, the dry flow of air travels through these channels, gaining moisture in the process. Furthermore, because the tube side flow in the humidifier is also the relatively cool side, it is also the means by which heat is received from the external flow. Conversely, the external flow path contains the hot, humidified air during normal operation and is known as the shell, shell side, or annulus. The shell side air flow is directed around the membrane and tube during humidification, transferring heat and vapor into the internal flow. This type of humidifier, while not a pure heat exchanger, operates on the same basis as a shell-and-tube heat exchanger, which is common enough to constitute its own class of heat exchange devices. Thus, the humidifier used in this study is referred to as a shell-and-tube humidifier and will be the focus of all subsequent discussion.

As well as geometrical considerations, there are other factors such as flow configuration that affect the performance and function of the humidifier. There are three main flow arrangements typically seen in a shell-and-tube apparatus: counter-flow, parallel-flow, and cross-flow. Each type of scheme differs in the direction of the internal and external bulk flows during operation, causing the heat transfer, and consequently the vapor transfer, to vary. The counter-flow heat exchanger indicates an arrangement in which the internal and external bulk streams travel coaxially, but in directly opposite directions.

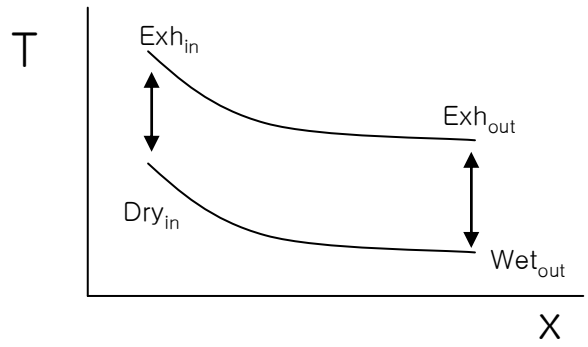

Figure 7: Counter-Flow Inlet and Outlet Temperatures

This type of setup is common in practice as it tends to provide excellent heat transfer characteristics relative to its alternative, parallel-flow. In this situation, the temperature differences of the outlets and inlets of the device remain equal, although the temperatures involved are higher on the hot inlet side.

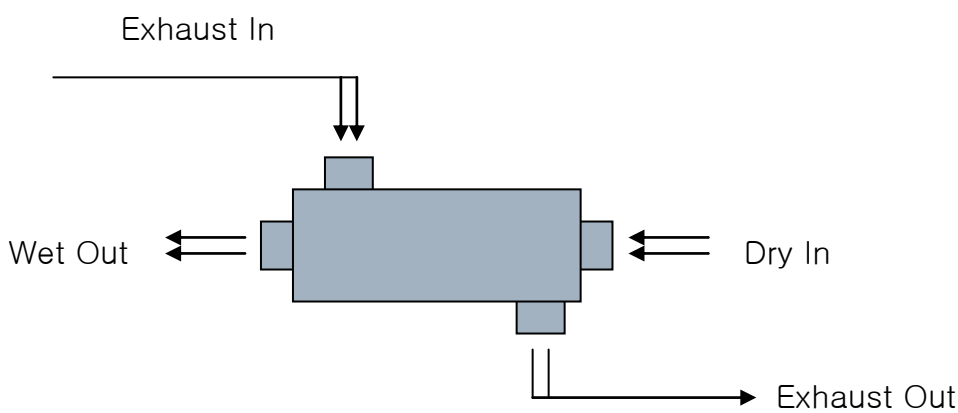

Figure 8: Arrangement of Counter-Flow

While parallel-flow is similar to counter-current flow in that the bulk fluid streams are coaxial, the parallel current distributes both the internal and external flows in the same direction.

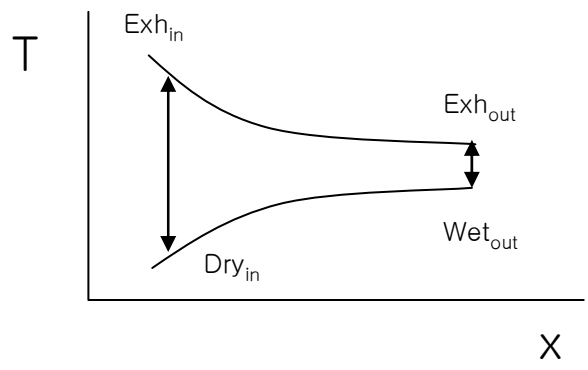

Figure 9: Parallel-Flow Inlet and Outlet Temperatures

This type of arrangement results in poorer heat transfer results when compared to the counter-flow scheme, as the temperature difference at the outlets of the hot and cold flows is smaller than that of the inlet of the two flows. Consequently, it is less common than the counter-flow arrangement.

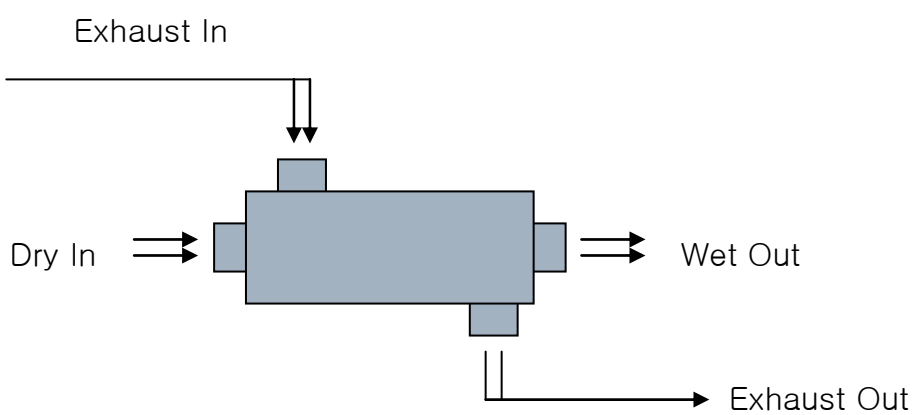

Figure 10: Arrangement of Parallel-Flow

However, a heat exchanger employing a cross-flow pattern exhibits the greatest heat transfer properties of all three mentioned arrangements. In this configuration, the flows of fluid travel perpendicularly to each other, usually with the external air flow transferring a large amount of heat to the internal flow. This type of heat exchanger is

common in applications where the hot fluid condenses onto the tube wall because the heat transfer area associated with cross flow can be considerably large. In fact, this is often the case as some cross-flow designs employ a *tube bank* arrangement, which is similar to the multiple tube design of the humidifier. In this situation, the external air is directed through the tube bank so that the effective heat transfer area is the total surface area of all of the tubes in the bundle.

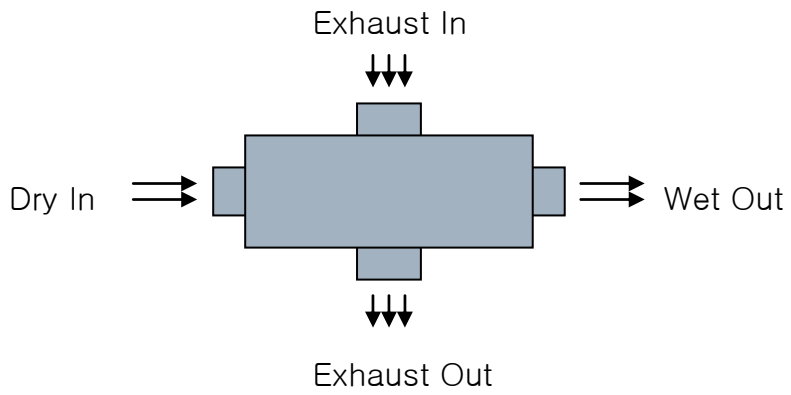

Figure 11: Arrangement of Cross-Flow

Finally, from the standpoint of design, there are flow regime considerations that are principle to the design of the membrane humidifier. Because of its partial function as heat exchanger, the performance of the gas-to-gas humidifier is subject to the influence of turbulent or laminar flow conditions on its heat transfer characteristics. These regimes often bring about very different results, with turbulent flow exhibiting superior energy transfer when all other variables are held constant. In heat exchanger design, this dependence upon flow regime affects its geometry considerably, as an annulus and tube must be of the appropriate shape and frontal area in order to demonstrate the desired flow characteristics under specific flow rates. Compounding this is the fact that channels with large frontal areas may need to be quite long in order to exhibit fully developed flow, an

assumption which simplifies the thermodynamic modeling of the device. Nonetheless, it is often impossible to obtain laminar or turbulent flow characteristics for all flow rates, and so a justification of design based on a specified range of flow rates for which the humidifier or heat exchanger will be used is usually made, resulting in various geometries. Furthermore, space requirements may extensively dictate the shape and length of the device, meaning that a uniform model and simulation of the heat and vapor transfer process may be difficult to obtain. It is therefore often important to have experimental data that may be used to verify any models that are produced.

2.2.4.2. PRINCIPLE OF OPERATION

The humidifier operates on the basis of temperature and vapor gradients within the membrane, which drive heat and moisture from areas of high levels of concentration to areas of lower levels of concentration. This property is manifested in the propensity of the Nafion material to dehumidify and cool a wet, hot flow of air, thereby humidifying and heating the other flow of air with which the membrane is in contact. In contrast to porous membranes and other vapor transport mechanisms, the Nafion material actually absorbs water vapor due to its unique chemical properties and, as such, does not transfer water in the liquid form [14]. This, as mentioned previously, is particularly important for maintaining moisture content in the fuel cell as no additional liquid water from the shell-side is introduced to fuel cell gas channel which could possibly lead to flooding.

However, it is also significant in the fact that water vapor is actually more efficient in transferring moisture in the case of the membrane humidifier, as any liquid water in contact with the membrane must undergo a phase change before adding

humidity to dry air. Interestingly, for the case of the liquid-to-gas humidifier, the liquid-to-vapor phase change in the flow of dry air requires that heat is added to the liquid water (meaning heat is lost from the dry air), which decreases the net amount of heat transfer experienced by the dry side. This fact causes there to be a need for a heater to preheat the water going to the humidifier—something which the gas-to-gas humidifier does not require.

2.3. REVIEW OF PREVIOUS RESEARCH

Because of the increased interest in fuel cell technology many papers have been put forth over the past decade and longer that investigate the characteristics of the membrane humidifier and how it can successfully be used for water management purposes in the fuel cell system. However, there are a few papers that have been the basis of most other subsequent papers and should be noted in order to give a complete review of the humidifier modeling schemes that are commonly used. Because of the novel nature of the materials used in the gas-to-gas humidifier, several unique correlations have been employed that help to describe the qualities of this specific device as opposed to other conventional technologies.

A very often cited author in the field of humidifier and fuel cell model is Zawodzinski whose work was one of the first to describe the behavior of Nafion 117 when exposed to water [16]. Because of the direct relationship between the performance of the Nafion membrane and the performance of the humidifier, this work has been extensively used to determine how effective the humidifier can be under various

operating conditions. He found that the amount of water that could be absorbed into the membrane was directly related to the water content on either side of the membrane.

Another paper that is often used is that of Springer [17] in which he describes the relationship between membrane humidity and perceived water content, which is discussed in Section 3.2. Because the water content is very important to the vapor transfer within the membrane, the experimental correlation between the two values has been influential to the modeling of the membrane humidifier. The water content, λ, is a dimensionless quantity defined as the mole ratio of water present in the membrane to sulfonic acid SO_3, which is the membrane material [17]. In the results, Springer found that a water content value of around 14.4 corresponds to a situation in which water vapor at saturation is in contact with the membrane. Furthermore, a value of approximately 16.8 is given for situations where the mole fraction of water exceeds saturation adjacent to the membrane. Thus, the outcome appears to be a paradox which is unique to the Nafion® membrane of the humidifier.

Several papers from D. Chen were published that describe in detail the dynamic [1] and static, as well as non-minimum phase [19], behaviors of membrane humidifiers that are very similar to the one researched in this study. Because of the extensive knowledge of fuel cell components of this author, her works are widely cited by those who wish to model critical components of the fuel cell, such as the humidifier. Furthermore, the study showed very good agreement with the experimental and simulated data for the conditions considered. Consequently, the publication of Park [20] relied heavily on the modeling theory of Chen, which produced excellent and accurate results for the conditions considered. However, the shortcomings of Chen's work are that it does

not go into detail about the heat and vapor transfer aspects of the liquid content on the shell-side of the humidifier. While the basic correlations exist, it is unclear what specific quantities were used for the heat transfer especially, which is necessarily different from the correlations that are used in the gas-to-gas humidifier. Nonetheless, one main aspect (the membrane activation energy) of the experimental findings of the works was discussed in detail is able to be applied to situations in which not only a single phase condition exists, but also where a two phase situation exists as well. This happens to be the case for the experimental conditions in this study and is discussed at length in Section 3.2.

2.3.1. PRIOR MODELING

Research prior to the current study at Auburn University was done by Sang-Kyun Park, et. al., and involved utilizing available theoretical equations along with applicable assumptions to generate a thermodynamically based model for the purpose of predicting humidifier outlet conditions at various inlet states. The inlet conditions consist of three main variables (temperature, relative humidity, and flow rate) which, when uniquely combined, determine specific static output conditions (temperature and relative humidity). The study consists of both static and dynamic simulation of the model under several variable inputs and a comparison to experimental data for the purpose of verifying the model. Static tests consist of experiments in which the measured data is collected after some steady state, or equilibrium is reached in the system under specific inputs. Thus, in that situation the data is not time dependent. By contrast, the dynamic tests consist of experiments in which the collected data is collected without reaching a

steady state so that, when it is plotted, shows a time-dependent trend. Nonetheless, both simulations of the model were performed in Matlab Simulink while the experimental data for comparison were provided by Perma Pure LLC. Although it is meant to predict the performance of its real world counterpart, the model is solely theoretically based, using existing equations for its representation of the actual performance. Thus, it is highly dependent upon the quality of the assumptions made and the correct application of its correlations.

2.3.2. ASSUMPTIONS

The assumptions made in the previous mathematical modeling of the humidifier are seven-fold:

First, the ideal gas law is applicable for all flows in the system. While the shell-side flow often contains a relatively high humidity compared to the tube-side, both flows are nevertheless air and as such are subject to the governing law.

Second, kinetic and potential energy losses are not considered. The low pressure nature of the humidifier allows for neglecting any kinetic energy loss due to pressure drop, while the lack of any major changes in elevation of the system trivializes any potential energy consideration.

Third, and importantly, the model assumes no heat (or vapor) losses. Despite being easy to control in the modeling, this assumption is not so easily achieved in practice as it is necessary to have a large amount of insulation around the heat exchanger. However, even when well insulated, heat loss to the surroundings is often unavoidable

and phase change within the device itself is a possibility regardless of the amount of insulation applied.

Fourth, the specific heat capacities in the system are assumed to be constant. This assumption simplifies calculations in the heat transfer that might be complicated by temperature variations.

Fifth, the effects of liquid phase species are not considered in the model. The model assumes all fluid within the shell-side and tube-side flows are either air or vapor. This allows for the neglecting of condensation and water droplet inundation from the fuel cell, which is a new area of research that is addressed in the current study.

Sixth, the previous model considers the humidifier to consist of two control volumes, separated by a single membrane. These two control volumes are the exhaust flow in the annulus and the tube side dry flow. While the actual humidifier contains in effect multiple separate flow volumes made up of the several hundred internal tubes, the model reduces these to a single tube and shell configuration in which the tube side diameter is derived from the sum total frontal area of all of the internal tubes combined. Unfortunately, this assumption will be shown to be inappropriate due to its effect on the calculated heat transfer within the device.

Seventh, and finally, the hydraulic diameters, D_h, of the control volumes are taken to be the inner diameters of each channel (thus, the inner diameter of the single tube and the outer diameter of the membrane thickness). This quantity is useful for determining the heat transfer coefficient on each side of the membrane, which can be used to calculate the overall heat transfer within the device. Typically, the hydraulic diameter is known via direct measurement or data from the manufacturer of the device. However, since the

diameter of the single tube is rather abstract, the selection of hydraulic diameter is somewhat arbitrary. Consequently, the single-tube configuration allows for uniform modeling conditions since the distances and heat transfer areas in the supposed thermal resistance representation are well defined, although it does not necessarily reflect the actual characteristics of the humidifier.

2.3.3. THERMODYNAMICS

Naturally, the method for predicting the heat transfer within the humidifier is thermodynamically based, with the conservation of energy and mass making up key criteria in the design. Also, the ideal gas law, which as stated before is applicable for the gas-to-gas device, is necessary for the calculation of humidity ratios in the tube and shell side flows. Because of the assumption that the humidifier is made up of two control volumes, energy and mass balances are the first principles used.

The energy balance is based on the idea that the change in internal energy in a control volume is equal to the change in energy due to heat minus the change in energy due to work, commonly written in the form

$$\dot{m}_{out} H_{out} = \dot{Q} + \dot{m}_{in} H_{in} - \left(\dot{m}u + \dot{u}m\right) \qquad (2\text{- }1)$$

which is a rate equation where the value of H is the enthalpy the value $\dot{m}$ is the mass flow rate. However, for a given control volume, there will also be heat and energy transferred across the boundary so that there is an additional term representing the transfer of energy within the system. That is, the heat located in a control volume at any given time is equal

to the sum total of heat moving in, heat moving out, and the difference in internal energy in the control volume. Mathematically, this can be described by the First Law, as

$$\dot{m}_{out} H_{out} = \dot{Q} + \dot{m}_{in} H_{in} - (\dot{m}u + \dot{u}m) + \dot{m}_{trans} H_{trans} \tag{2- 2}$$

Similarly, in order to bring about an energy balance, a mass balance is necessary to quantify the amount of mass in each control volume. The amount of mass at a given time is made up of either air or vapor (since no liquid water is assumed present). This gives rise to the balance equation:

$$\dot{m}_{total} = \dot{m}_{vapor} + \dot{m}_{dryair} \tag{2- 3}$$

Here the total amount of mass can consist of both species, air and water, where the percentage of each in a given flow is known by the humidity ratio. The humidity ratio is a measure of the amount of vapor in a sample of air given by the ratio of vapor mass to dry air mass at a given pressure [12], which can be expressed by

$$\omega = \frac{m_{vapor} p_{vapor}}{m_{dryair} p_{dryair}} \tag{2- 4}$$

or in the case where the vapor pressure is equal to the dry air vapor,

$$\omega_{cv1} = \frac{m_{vapor,cv1}}{m_{dry\,air,cv1}} \tag{2- 5}$$

and

$$\omega_{cv2} = \frac{m_{vapor,cv2}}{m_{dry\,air,cv2}} \tag{2- 6}$$

Using these equations and the fact that the dry air flow rate is equal to the mass flow rate at inlet or outlet for a given control volume, the rate of vapor mass is given by

$$\dot{m}_{vapor} = \dot{m}_{total} - \dot{m}_{dryair} \tag{2- 7}$$

which is a rearranged version of equation (). Applying the definition of humidity ratio [12] and the substituted value of vapor mass flow gives

$$\omega = \frac{\left(\dot{m}_{total} - \dot{m}_{dryair}\right)}{\dot{m}_{dryair}} \tag{2- 8}$$

which can be simplified to

$$\left(\dot{m}_{dryair}\omega\right) = \dot{m}_{total} - \dot{m}_{dryair} \tag{2- 9}$$

whereby the equation is reduced to the two known values of total mass flow and humidity ratio. The unknown value is the dry air flow, which can be isolated on one side of the equation to show

$$\left(\dot{m}_{dryair}\omega\right) + \dot{m}_{dryair} = \dot{m}_{total} = \dot{m}_{dryair}\left(1+\omega\right) = \dot{m}_{total} \tag{2- 10}$$

A final simplification shows that the dry air mass can be represented as a function of the two known values, total mass flow rate and humidity ratio. The mass rate of the vapor, $\dot{m}_{vapor}$, can be found by simply subtracting the mass rate of the dry air, $\dot{m}_{dry\ air}$, from the total mass flow rate, $\dot{m}_{total}$, which is either known at the beginning of an experiment or, in the case of the previous modeling, assumed at the start of a simulation.

2.3.4. HEAT TRANSFER

By abbreviating the actual humidifier into two control volumes the thermodynamic representation is simplified into a common system, whereby the heat transfer properties can be modeled as radial thermal resistances. The truncated model results in three resistances which correspond to the annulus, tube, and membrane (or wall).

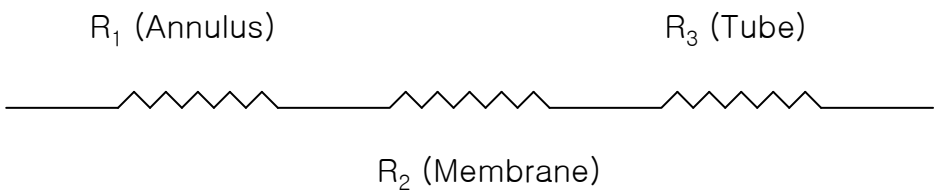

Figure 12: Single-Tube Thermal Resistances

Together these make up an overall thermal resistance with an overall heat transfer coefficient that can be used to describe the heat transfer characteristics. This overall thermal resistance model is commonly described by

$$\frac{1}{UA} = \frac{1}{h_i A_i} + \frac{\ln\left(D_o / D_i\right)}{2\pi L k_{mem}} + \frac{1}{h_o A_o} \tag{2- 11}$$

where the first and third terms on the right hand side of the equation refer to the tube and annulus thermal resistances, respectively, and the second term indicates the membrane thermal resistance. Heat transfer coefficients for shell and tube side thermal resistances are alternatively given as

$$h_z = Nu \frac{k_z}{D_h} \tag{2- 12}$$

with the subscript z designating either the annulus or tube side and D_h referring to the hydraulic diameter. Since the simplified, single tube model is used in Park's study, the latter coefficient is simply the internal diameter of the single equivalent tube for the tube side heat transfer coefficient representation, although for more complicated geometries with various channel shapes or parameters this is often not the case. Also of importance is the choice of Nusselt number, Nu, by which the value h is calculated.

2.3.4.1. TUBE-SIDE

The model for internal flow uses the commonly-cited Dittus-Boelter equation for the derivation of internal *Nu*, given by

$$Nu = 0.023\,\mathrm{Re}_D^{\,0.8}\,\mathrm{Pr}^{0.4} \tag{2- 13}$$

in which the value of Reynolds number, *Re*, and Prandtl number, *Pr* are known from the inlet flow conditions (flow rate and temperature). It is important to note that the Dittus-Boelter equation is applicable for only turbulent flows, where $Re > 4000$ for flows in pipes (i.e. tubes). In fact, due to Park's single tube supposition, with D_h based on the total internal frontal area, the equation is valid over the range of flow rates considered in the research as *Re* remains above 4000 (see Table 1). However, it is also significant to note that a turbulent *Re* for the single-tube situation is due to the relatively high value of D_h exhibited when compared to the multi-tube situation. This effect can be understood by considering the equation for Reynolds number

$$\mathrm{Re}_D = \frac{VD_h}{\nu} \tag{2- 14}$$

where V is the velocity of the fluid. With all other variables held constant, it is evident that the value of *Re* is highly dependent on the selection of D_h. The single tube assumption means that D_h is improbably high since it fails to represent each tube in the internal flow, and instead creates a situation that does not exist within the actual device. That is, the calculated Reynolds number is always above the critical Reynolds number for turbulence. Thus, when the diameter of the single internal tube is based on the sum area of the actual humidifier, some information is inherently lost, although it allows for the use of a convenient and well known correlation.

2.3.4.2. SHELL-SIDE

Similar the tube side heat transfer calculation, the shell-side heat transfer coefficient can be found by again using a specific Nu that relates to the geometry. The external Nu value takes the same form,

$$Nu = x\,\mathrm{Re}_D{}^{y}\,\mathrm{Pr}^{1/3} \tag{2- 15}$$

where x and y are constants that can be determined from a well known correlation, known as the Hilpert correlation, which can be found in Incropera and Dewitt [14]. It is given by

$$Nu_{D,avg} = C \cdot \mathrm{Re}_D^m \cdot \mathrm{Pr}^{1/3} \tag{2- 16}$$

which is applicable for Pr >0.7 and where the values for C and m are given by

Re_D	C	m
0.4-4	0.989	0.330
4-40	0.911	0.385
40-4000	0.683	0.466
4000-40,000	0.193	0.618
40,000-400,000	0.027	0.805

Table 1: Hilpert Correlation [14]

The data is applicable for *external* flow over a single, isolated tube. Figure 13 shows the intended situation for which this correlation is meant to be used, with a purely cross-flow pattern represented. However, as will be discussed in the next chapter, this type of correlation is not particularly useful for representing the actual geometry of the

humidifier. In fact, because of the single-tube approximation, several effects on that type of modeling technique are noted, which introduce unintended, but avoidable error.

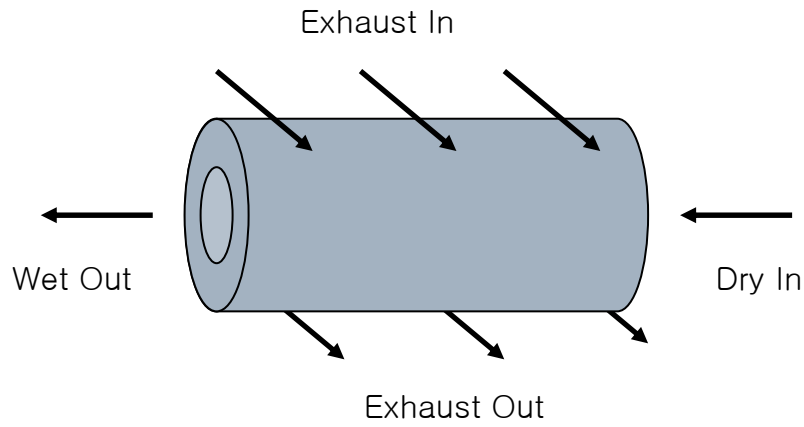

Figure 13: Cross-Flow Representation of Single-Tube Model

Nonetheless, the internal and external thermal resistances are clearly convective terms, which change as flow rate changes. Furthermore, because the heat transfer area, referred to in Equation (2-11), is constant, the main factor in the thermal resistance is the internal or external heat transfer coefficient, h_o, which is itself a function of both the flow rate and temperature difference in the flow.

However, the wall thermal resistance in the membrane is based on conduction rather than convection, making it more of a geometric parameter and material property than a variable, so it is not considered to change during operation. Its thermal resistance is given by the middle term in Equation (2-11) with the value of k_{mem}, the membrane thermal conductivity, being a material property of the Nafion® material. While in fact the thermal conductivity of the membrane may change during the operation of the humidifier, it is much less temperature dependent than the values for air in the convection within the two control volumes. In addition, the exact temperature of the membrane is

difficult to know with certainty since the temperature field varies over its length and under different flow inlet conditions. Hence, it is assumed that the thermal conductivity of the membrane is a constant, with any major discrepancy in the wall thermal resistance being due to geometrical and material characteristics.

2.3.5. VAPOR TRANSFER

Vapor transfer within the humidifier is a result of concentration gradients within the membrane material. Therefore, the amount of vapor transfer exhibited under a specific flow condition is dependent upon the humidity difference between the tube side and the relatively humid shell side. The amount of vapor mass transferred during operation from the annulus to the tube is given by:

$$m_{v,trans} = D_w \cdot \left(\frac{C_{shell} - C_{tube}}{t_{mem}} \right) \cdot m_v \cdot A \tag{2- 17}$$

where C denotes the water mass concentrations in each channel and t is the thickness of the membrane under the proposed single tube representation. The diffusion coefficient describes the propensity of the membrane to transport water as a function of absolute temperature and is consequently described as

$$D_w = D_\lambda \exp\left[2416 \left(\left(\frac{1}{303} \right) - \frac{1}{T_{mem}} \right) \right] \tag{2- 18}$$

in which the temperature is in units of Kelvin, the value 2416 is the activation energy, E_o, and the coefficient D_λ is a constant found using the following piecewise function [20]:

$$D_\lambda = \begin{cases} 10^{-6} & \lambda_{mem} < 2 \\ 10^{-6} \cdot [1 + 2(\lambda_{mem} - 2)] & 2 \le \lambda_{mem} \le 3 \\ 10^{-6} \cdot [3 - 1.67(\lambda_{mem} - 3)] & 3 \le \lambda_{mem} \le 4.5 \\ 1.25 \times 10^{-6} & \lambda_{mem} \ge 4.5 \end{cases} \tag{2- 19}$$

The activation energy is discussed further in Section 3.2.2. Nevertheless, Equation (2-19) was taken from Springer's [17] paper where the value of λ_{mem} refers to the mean water content located in the membrane at any given time, which is used to calculate the empirical constant from Equation (2-19). It is given by

$$\lambda_{mem} = \frac{\dfrac{C_{H_2O,mass}}{M_{H_2O}}}{\dfrac{\rho_{dry,mem}}{M_{mem}} - 0.0126\dfrac{C_{H_2O,mass}}{M_{H_2O}}} \tag{2- 20}$$

In which C is the mass concentration of the water in the membrane, ρ is the density of the dry membrane, and M is the mass of either the membrane or the water located within the membrane. Similarly, the boundary water content, the amount of vapor at the boundary of each side of the membrane, is found by another piecewise function

$$\lambda_i = \begin{cases} 0.043 + 17.8a_i - 39.85a_i^2 + 36a_i^3 & 0 < a_i \le 1 \\ 14 + 14(a_i - 1) & 1 \le a_i \le 3 \\ 16.8 & a_i \ge 3 \end{cases} \tag{2- 21}$$

where the value a is the relative humidity on the shell or tube side.

Once the relative humidity is known on each side of the membrane, it can be plugged into Equation (2-22), outputting the value of the boundary water content. From there, the mean water content in the membrane, water concentration, D_λ, diffusion coefficient, and rate of vapor mass transfer are found in succession by inserting all of the other known values into the given equations.

3. CURRENT HUMIDIFIER MODELING

During the course of this study, several improvements have been made to the heat and vapor transfer model proposed by Park. The most basic and important change to the modeling effort is the consideration of the control volumes, which are central to the determination of the rates of both heat and mass. In fact, as will be shown, this modification has a great impact on the calculation of some of the most important factors such as Reynolds number, Nusselt number, and volumetric flow rate. In the context of the single-phase representation, a parametric analysis is presented that will show the geometric differences between the previous and current modeling and their repercussions, as well as an in-depth look at how they affect the perceived heat and vapor transfer of the system. The limitations of the single-phase model are then discussed and a new two-phase model is introduced that more accurately represents the characteristics of the humidifier under the normal operating conditions. Finally, the effects of pressure drop on the operation of the humidifier are examined to determine if the effects are large enough to affect the outcome of simulations.

3.1. SINGLE PHASE MODEL

In the previous modeling technique, the humidifier is simplified into a single-tube device containing two control volumes corresponding to both the tube side and shell side flows,

separated by the Nafion® membrane. However, because the model no longer consists of a single tube and annulus, the heat transfer scheme is represented differently. The resulting thermal resistance circuit still consists of two convection terms, represented by R_1 and R_3, and a conduction term denoted as R_2. However, R_1 and R_3 now refers to the *total* shell-side and tube-side flows, both of which are actually made up of 780 individual flows because the tube bank consists of that many tubes.

In the previous model, the diameter of the shell and tube-side channels was determined by the total frontal area of all of the individual tubes combined, so that the single tube model and actual humidifier contain the same frontal area, but different flow channel diameters. But as will be shown, because the humidifier consists of several hundred tubes within a single shell, it is most accurately described as a shell-and-tube heat exchanger that also transfers mass in the form of vapor rather than as a single tube and annulus. Despite this, the thermal resistance modeling technique can still be used to calculate the heat transfer, albeit in a slightly different form.

3.1.1. PARAMETRIC ANALYSIS

While the internal and external flow areas, given by the frontal areas of the corresponding flow paths, are not affected by the single-tube assumption, other factors such as the hydraulic diameter and flow rate are not accurately represented. Figure 14 shows the equivalent diameter of the tube side based on frontal area (approximately 0.027 m) and the actual shell inner diameter (0.056 m) in the arrangement of the previous model.

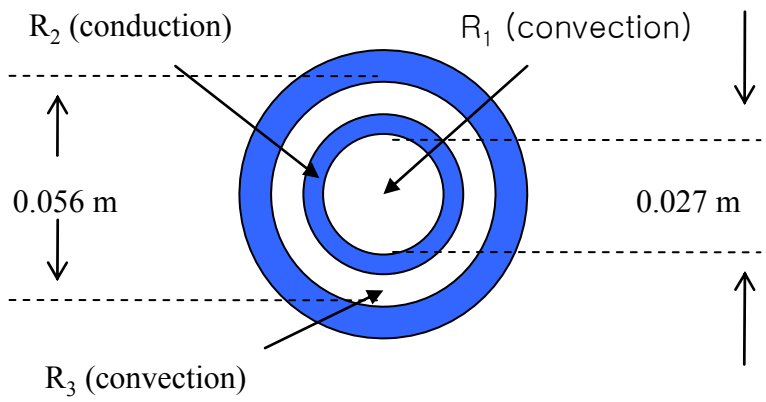

Figure 14: Single-Tube Model Showing Diameters and Thermal Resistances

Despite the fact that the frontal area is unchanged by the single-tube assumption, the equivalent tube diameter is incorrectly used as the hydraulic diameter and therefore does not provide the most accurate Nusselt number of the system. In fact, because the equivalent tube is assumed in the previous model to be the hydraulic diameter, the Reynolds number of the tube side flow is incorrectly assumed to be turbulent. Furthermore, because of this, the Dittus-Boelter equation [14] is inappropriately used.

The effect of this misrepresentation can be clearly seen in tabular form. Table 2 shows that for even the lowest flow rate that is typically seen by the humidifier the flow regime is perceived to be turbulent, easily exceeding the critical Reynolds number threshold value of 2300. The problem with this assumption is that the use of a turbulent correlation for internal flow not only increases the modeled heat transfer coefficient significantly, but also it makes the tube side heat transfer coefficient (and therefore the overall heat transfer) a function of Re_D, which increases with increasing flow rate, and Pr which varies with temperature. Yet, as will become apparent, the heat transfer coefficient,

at least for the tube side flow, actually is not a function of the flow rate but is instead independent of Re_D and remains constant over the typical flow range.

Mass Flow Rate (kg/s)	Approximate Volumetric Flow Rate (slpm)	Approximate Velocity (m s^{-1})	Approximate Re
0.002	101.2	2.927	5091
0.003	151.8	4.390	7636
0.004	202.4	5.854	10,182
0.005	253.1	7.317	12,727

Table 2: Single-Tube Reynolds Numbers at Various Flow Rates

As seen in Figure 15, the actual frontal area of each individual tube is much smaller than the assumed equivalent tube, making the perceived Reynolds number in fact much lower than what is modeled by the single-tube assumption.

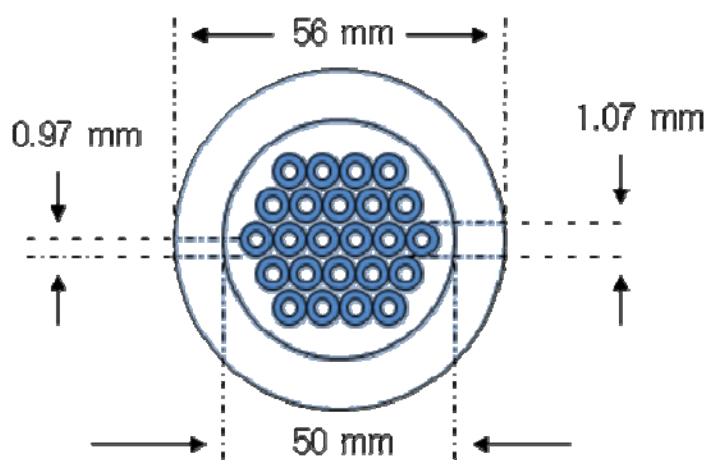

Figure 15: End View Rendering of Humidifier

According to Incropera and Dewitt [14], the correct hydraulic diameter of a flow channel is given by

$$D_h = 4 \cdot \frac{A_c}{S} \tag{3- 1}$$

where A_c is the cross sectional area of all of the tubes combined and S is the wetted perimeter of all the internal tubes, equal to the number of tubes multiplied by the circumference of an individual tube. Using this equation, it becomes clear that the appropriate hydraulic diameter for the tube side flow is simply equal to the inner diameter of a single tube, 0.00097 m. However, most important is the effect of the hydraulic diameter on the modeling characteristics of the system—the primary outcome of the smaller D_h is a lower Reynolds number and resulting change in flow regime from turbulent to laminar. Unlike the single tube assumption, the internal mass flow rate is divided into 780 equal flow rates corresponding to the 780 equally sized internal tubes, making the mass flow rate per tube very small while the velocity of flow within each tube is unchanged. In looking at the Reynolds number equation it is evident that the small value of D_h has a limiting effect on the tube side Re_D

$$\mathrm{Re}_D = V \cdot \frac{D_h}{\nu} \tag{3- 2}$$

with V being the velocity of the fluid at the specific flow channel and ν being the kinematic viscosity, which is a temperature dependent property. Because the tube side velocity, unlike the mass and volumetric flow rates, is equal for all tubes in the flow channel, it can be considered constant for a specific inlet flow rate, making D_h the variable factor in Reynolds equation. As a result of this new, very low assumed hydraulic diameter and resulting Re_D, it is evident that the flow regime for the tube side remains laminar throughout the entire range of mass flow rates. In stark contrast to the results of

the Reynolds number calculations for the single-tube equivalent diameter, Table 3 shows that the value of Re_D for the case of the multi-tube system does not approach the transition threshold for turbulence.

Mass Flow Rate(kg/s)	Approximate Volumetric Flow Rate (slpm)	Approximate Velocity (m/s)	Approximate Re
0.002	101.2	2.927	182
0.003	151.8	4.390	273
0.004	202.4	5.854	365
0.005	253.1	7.317	456

Table 3: Actual Reynolds Numbers at Various Flow Rates

In fact, due to the extremely small hydraulic diameter, a flow rate on the order of 1,300 SLPM would be needed to bring the internal flow to turbulence, which is much higher than the normal operating range seen by the humidifier.

With regards to the parameters of the previous model, another reason that the single-tube assumption is not suitable for the modeling of the humidifier concerns the hydraulic entry length. The entry length describes the distance along the inside of the flow channel that it takes for the flow to become fully developed. Generally, correlations for typical flow problems are only applicable for conditions where the fluid has fully developed and a steady, predictable flow is exhibited. However, if the entry length is long, correlations such as Dittus-Boelter are not very accurate. Unfortunately, in the previous model, the entry length of the single equivalent tube prohibits the use of such a model.

Furthermore, Incropera and Dewitt [14] note that for turbulent flow conditions the entry length is by and large independent of Reynolds number, with fully developed conditions occurring after a length of ten times the diameter of the pipe along the flow channel. Because the internal diameter of the tube in the previous model is approximately 2.7 cm, the entry length is seen to be nearly 27 cm. In addition, because the active length of the tubes is roughly 25.4 cm (see Table 4), the flow would actually never become fully developed, making the use of the Dittus-Boelter equation impractical. Thus, as will be shown in the following sections, the tube bank approximation is much more reasonable due to its much shorter entry length and correlations.

Membrane Thickness	0.00005 m
Inner Diameter of Membrane Tube, D_i	0.00097 m
Active Length of Membrane Tube, L	0.254 m
Overall Length of Humidifier	0.311 m
Number of Tubes, N	780
Inner Diameter of Membrane Housing, D_{shell}	0.056 m

Table 4: Geometric Parameters of Humidifier

3.1.2. HEAT TRANSFER

Another consequence of the dramatic effect on the tube-side Reynolds number is that the modeling of the heat transfer process must be modified to reflect the laminar flow within the channel. Primarily, the use of the Dittus-Boelter equation becomes inappropriate, since the correlation is contingent on the presence of turbulence in the flow

channel. Naturally, this has the result of lowering the heat transfer coefficient on the tube side, since a laminar flow generally involves less energy transfer than turbulent flow. On the other hand, for the shell-side modeling, the issue becomes not one of assuming the correct hydraulic diameter, but instead appropriately choosing a Nusselt number correlation that reflects the true nature of the external channel. Because the tubes are situated in a bundle, they may be modeled more accurately with tube bank correlations. However, more relevant *shell-and-tube* correlations exist for this particular arrangement, which is not purely counter-flow or cross-flow.

3.1.2.1. TUBE-SIDE

Due to the fact that laminar nature of the tube side flow prohibits the use of a turbulent flow relation, it is necessary to extract a useful correlation for Nusselt number whereby the heat transfer coefficient for the tube side can be estimated. Fortunately, this can be easily accomplished through the assumption of either a constant surface temperature or constant heat flux condition on the tube-side, with the Nusselt number for each condition being constant for laminar flow. This can be described as follows for fully developed flow from Kays and Crawford [22]

$$Nu_D = 3.66 \qquad \text{(Constant } T_{mem}\text{)} \qquad (3\text{- }3)$$

$$Nu_D = 4.364 \qquad \text{(Constant Q")} \qquad (3\text{- }4)$$

In the above equations, T_m represents the surface temperature of the membrane while *Q"* denotes surface heat flux. Typically, the values can be applied to a situation in which the geometry is very simple (i.e. a single tube) and when one condition is

dominant. However, due to the complex nature of the tube side flow the prevalence of one condition as opposed to the other is not apparent and so an average value of the two, or some number between the two, may be appropriate in the modeling as the tube side may actually exhibit both conditions. For the purpose of this research, the Nusselt number was assumed to be 3.66, that of a constant membrane temperature situation, which matched the experimental data the best. Nonetheless, because of the evidently dominant laminar flow regime on the tube side, the internal heat transfer coefficient is known to be no longer dependent on Reynolds, varying only with temperature (due to the value of ν). Thus, using the definition of Nu_D, the heat transfer coefficient for the tube side can be given by

$$h_i = \frac{Nu_D \cdot k}{D_i} \tag{3- 5}$$

where k is the thermal conductivity of the tube side fluid, which is simply air.

It should be noted that the Nusselt numbers listed above do not necessarily apply to all laminar flows within tubes. In fact, if the effect of hydraulic entry length is large, then the Nusselt number within the channel will *not* be constant at all locations. In such a situation, other correlations are more appropriate and will give more accurate results. However, as will be shown in Section 3.3.1., the entry length for the internal tubes in the humidifier in question makes up less than 6% of the total length of the tubes. Thus, the influence of the entry length is effectively diminished and the constant Nusselt number values are sufficient for the tube-side modeling.

3.1.2.2. SHELL-SIDE

Modeling on the shell side of the humidifier is quite different from that of the tube side. Previously, the external flow was considered to be that of air flowing over a single tube, with the flow path being the space between the shell inner diameter and the equivalent tube calculated from the frontal area of the tube side. Figure 16 showed the representation that corresponds to the correlation used in the previous research. While the correlation is used in that model to describe the internal annulus flow over the internal tubes, it is actually intended to be used with a purely external flow over a single cylinder. Furthermore, while the heat transfer calculation of the entire system employs a counter-flow log mean temperature difference in that model, the correlation for Re_D is misused due to the fact that it is intended for a single cylinder in *cross-flow* rather than flow in the axial direction and would require a corresponding cross-flow log mean temperature difference.

The corresponding Re_D is based on the hydraulic diameter of the tube in question. However, because the correlation is again dependent on D_h, problems arise when attempting to use it since it is likely that the assumed diameter is not correct. Indeed, due to the single-tube assumption of the previous modeling, the hydraulic diameter is assumed to be based on the outer diameter of the single internal tube, which is simply the inner tube diameter plus the thickness of the membrane. The hydraulic diameter in that situation is given by

$$D_h = D_{shell} - D_{mem} \tag{3- 6}$$

because the flow is essentially an annulus flow and where the first term is the inner diameter of the shell, 0.056 m [22]. The second is the outer diameter of the membrane, assumed to be 0.05 m in the model.

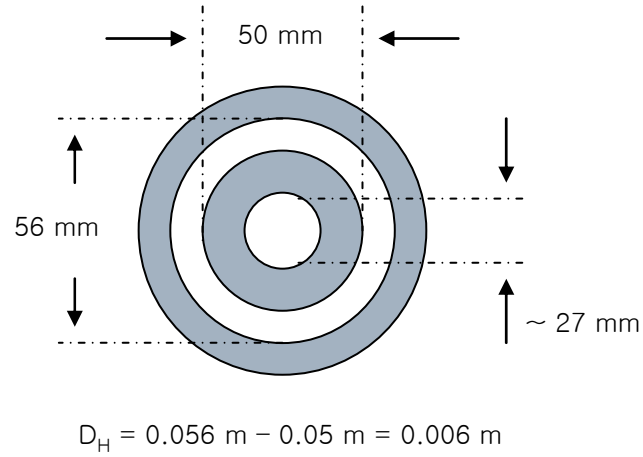

Figure 16: Hydraulic Diameter of Single-Tube Model

The problem with this representation is that there is no knowledge of the thickness of the membrane except for that of each individual tube (t = 0.00005 m) that was provided by the manufacturer. Moreover, the fact that the shell side flow is in reality over and through a bank of tubes rather than simply over an equivalent single tube in cross-flow causes some concern when using that correlation—it is unclear whether a cross-flow correlation such as the Hilpert's is appropriate since the extent to which cross-flow actually exists in the humidifier is unknown.

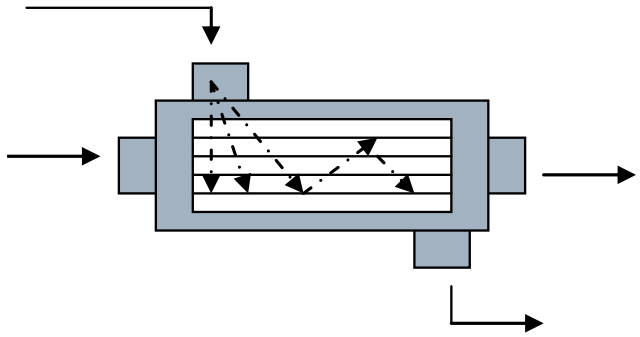

Figure 17: Characterization of Shell-Side Flow

The uncertainty of the flow pattern is best described graphically. Figure 17 illustrates how the shell side flow might travel within the tube bank for the FC 200-780-10 humidifier under normal conditions. There is obviously no single dominant flow pattern present that would enable the use of a cross-flow correlation and rule out a counter-flow correlation. However, it becomes apparent that the cross-flow correlation used in the previous study omits some information about the actual flow within the device. While the flow at the shell inlet and outlet exhibit dominantly cross-flow, Figure 17 shows that the flow between the two ports is either counter-flow or some combination of cross-flow and counter-flow. Notably, however, the assumption of pure cross-flow for the use of the correlation is not realistic for the actual flow within the humidifier since the dominant flow arrangement is variable along the length of the shell side flow channel. It is therefore clear that the use of the Hilpert equation is inappropriate and that some other means of modeling the actual flow must be used.

In order to accomplish this, it is necessary to employ a purely shell-and-tube heat exchanger model, which most accurately represents the humidifier. While the earlier research acknowledges that the device is essentially a bundle of tubes within a single shell, the simplified single-tube model was employed to simplify calculations. However,

as it turns out the heat transfer of the humidifier can be modeled in a very similar way to that of a shell and tube heat exchanger which has a near identical geometry to that of the humidifier. Much effort has been put forth in the attempt to model the heat transfer of these devices, most for industrial scale devices, and two main contributors are discussed presently.

3.1.2.3. SHELL-AND-TUBE CORRELATIONS

Research regarding the approximation of the shell side heat transfer coefficient for shell-and-tube heat exchangers with segmented baffles was done by Bell [23], in which the baffle segments correspond to greater heat transfer coefficients due to forced repeated passes over the tube bank. The method for describing the heat exchange in such a device is known as the Bell-Delaware method and can be employed for devices with baffles. However, because the humidifier is not baffled and relatively little is known about the geometry of the shell side, a more appropriate and easily-used approach is the Kern method [24] for heat exchangers without baffle segments, which describes an equivalent diameter, D_e, of the shell side channel and calculates a representative cross-flow mass velocity, G_m, based on an equivalent cross-flow area, A_{xf}, that can be used to approximate the shell side convection coefficient. The equivalent diameter and cross-flow area is a means of taking into account the fact that the bulk shell side fluid travels mostly in the axial direction along the tubes, but also experiences some cross-flow in the process as in Figure 17 [25].

The approach begins by finding the previously mentioned equivalent diameter for flow on the shell side, which is different for square pitch and triangular pitch tube banks.

But because the tubes within the shell are randomly spaced, it is impossible to know the exact pitch of the tubes for a given location and so the triangular pitch, or staggered tube, arrangement is assumed since it best represents the unaligned layout of the tubes. As is shown in Figure 18, an equiangular triangle is assumed in Kern's method so that all sides are equilateral—this is a reasonable assumption since very little knowledge of the randomly-spaced internal tubes is available.

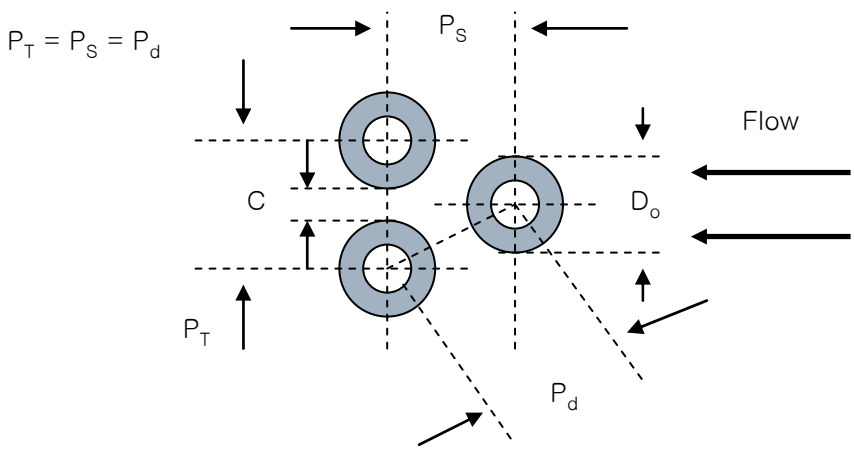

Figure 18: Dimensions of Shell-and-Tube Flow Arrangement

The values of P_T, P_S, and P_d denote the transverse, longitudinal, and diagonal pitches (all equal), respectively. The value of C represents the spacing between the outer diameters of the tubes, which, for the purpose of this research, will be some multiple of the outer diameter of an individual tube, D_o, which provides the overall best heat transfer coefficient for the model. Thus, the equation for P_T can be given by

$$P_T = (y \cdot D_o) + D_o \tag{3- 7}$$

in which y is the multiple and the first term is the value for C. With these values known, or assumed, it is possible to calculate an equivalent diameter through which the external

air will travel, along the length of the humidifier. For the assumed staggered tube configuration, Kern suggested that the equivalent diameter be given by

$$D_e = \frac{1.72 \cdot P_T^2 - 0.5 \cdot \pi \cdot D_o^2}{0.5 \cdot \pi \cdot D_o} \tag{3- 8}$$

which is simply the equation for D_H in the context of Figure 19. As per the Kern method, this is the diameter that should be used in the calculation of Re_D and Nu_D.

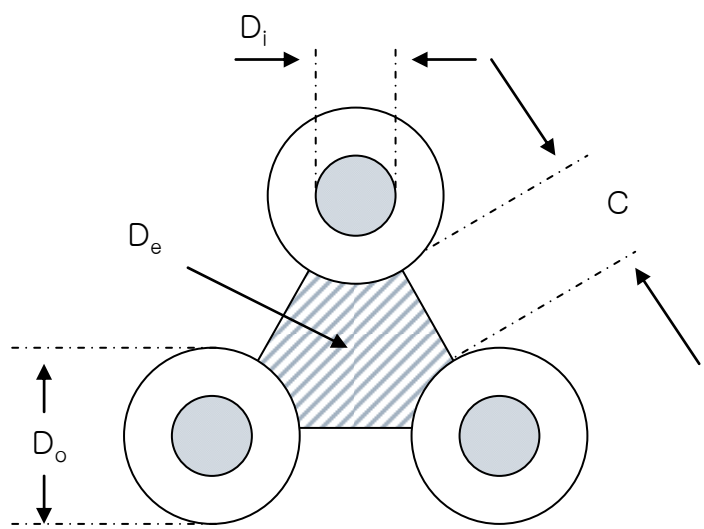

Figure 19: Kern's Equivalent Diameter

The mass velocity of the shell side, G_m, is representative of the maximum fluid velocity through the bank of tubes, which is through the equivalent cross-flow area. It can be represented by

$$G_m = \frac{\text{mass flow rate}}{A_{xf}} \tag{3- 9}$$

where the denominator is given by

$$A_{xf} = \frac{D_{shell} \cdot \mathrm{C} \cdot \mathrm{B}}{P_T} \tag{3- 10}$$

in which D_{shell} is the inner diameter of the shell (0.056 m) and B is the baffle spacing, equivalent to the length of the tube bank (0.254 m) for heat exchangers without baffles. The cross-flow area is not an actual physical dimension, but a type of abstract area proposed by Kern to represent the amount of cross-flow that occurs in a specific shell-and-tube heat exchanger due to the fact that the flow is not purely normal to the tube bank. Furthermore, he proposes that Nu_D be given by

$$Nu_D = 0.36 \cdot \mathrm{Re}_D^{0.55} \cdot \mathrm{Pr}^{1/3} \tag{3- 11}$$

for $2000 < Re_D < 10^6$, which is essentially a turbulent shell side correlation. Unfortunately, as will be shown later, the flow regime for the shell-side under the typical operating conditions is dominantly laminar. Nonetheless, there are other existing cross-flow correlations that can be used to predict the shell side heat transfer coefficient when used in conjunction with Kern's equivalent cross-flow area.

Zukauskas [26] proposed an external Nusselt correlation for tube banks which exhibit either an aligned or staggered configuration. In the correlation, all of the material properties of the fluid are taken to be at the arithmetical mean of the fluid inlet and outlet temperatures. Thus, in the model, as the outlet temperatures are calculated, they can be used to calculate an updated value of the material properties. In addition, the correlation requires the knowledge of Re_D based on true hydraulic diameter (D_o) of the tube bank rather than D_e. While this appears to be a problem for the calculation using Kern's method, Bell [23] notes that the selection of D_h using the Kern method is rather arbitrary and that D_o could just as well be used with minimal loss in accuracy. So, for the purpose of calculating Re_D, the outer tube diameter is used in the calculation (0.00107 m). But in order to calculate Re_D the maximum velocity through the tube bank should also be

known—typically this is the velocity through the small spaces between the tubes. But, due to the fact that the flow is not solely across the bank of tubes, the value of A_{xf} is used to calculate the maximum velocity, G_m, through the shell side since the tube bank is of the shell-and-tube geometry. Thus, a correlation for the shell side heat transfer can be obtained, and, as per Zukauskas, the Nusselt numbers for various flow rates can be estimated by

$$Nu_D = b \cdot \mathrm{Re}_{D,\max}^{m} \, \mathrm{Pr}^{0.36} \left(\frac{\mathrm{Pr}}{\mathrm{Pr}_s} \right)^{\frac{1}{4}} \tag{3- 12}$$

in which b and m are empirically found constants that are given in Table 5.

$Re_{D,max}$	b	m
10-100	0.9	0.4
100-1000	Treat as Single Cylinder	Treat as Single Cylinder
1000-20000	0.27	0.63

Table 5: Constants of Zukauskas Correlation

In fact, there are more values listed in the actual table that correspond to higher Reynolds numbers. But because the Re_D of the flow through the tube bank does not go above 100 at the flow rates considered in the model, the rest of the list is unnecessary. Moreover, Bell noted that the overall flow regime of most tube banks is laminar, except for very high flow rates. Additionally, in the range where Reynolds number is 100-1000, the tube bank can be modeled as a single, isolated tube. This is interesting in the fact that the Hilpert correlation could actually be used for those conditions. However, as stated

before, the highest Re_D seen in the modeling was below 100. Another noteworthy simplification is the omission of the term in parenthesis at the end of the equation. Because the difference between the wall Prandtl number and that of the exhaust air are nearly identical, the term is always near unity for the conditions considered in the experiments. Thus, the fraction is not used in order to simplify calculations.

Finally, in order to have the complete thermal resistance scheme for the system, the membrane thermal resistance is needed. The resistance to heat transfer of the membrane is a function of the radial distance it takes up on the outside of the inner tube, the thermal conductivity, and the length of the tubes in the tube bank. Whereas the previous single-tube model considered the membrane thickness to be the outer diameter of the tube bank subtracted by the inner equivalent tube diameter, there is actually a more convenient way of modeling the membrane in a bank of tubes. In a tube bank, the wall thermal resistance can be given by

$$R_{mem} = \frac{\ln\left(\frac{D_o}{D_i}\right)}{2 \cdot \pi \cdot k_{mem} \cdot L \cdot N} \tag{3- 13}$$

where the subscript *mem* refers to the membrane, *k* refers to the membrane thermal conductivity, D_o and D_i are the outer and inner diameters of an individual tube, and *N* is the number of tubes. Using the values from Park's paper and a k_{mem} value of 0.21 (W/m K), it can be found that the thermal resistance of the membrane is equal to approximately 3.75×10^{-4} (K/W).

3.1.3. LIMITATIONS

Although the single-phase model seems robust for conditions in which vapor exists on either side of the membrane, recent research along with the results of the experimental data from this study have led to the formulation of a more appropriate humidifier model. The single-phase design can be seen as a best case scenario in which the effects of shell-side liquid inundation and condensation do not occur. However, it appears that this type of condition rarely occurs for the actual humidifier in its working environment. Thus, because of the aforementioned effects and the large discrepancy between the single-phase results and those of the experiment, a new two-phase model has been developed to help explain why the previous model cannot completely model the gas-to-gas humidifier.

3.2. TWO-PHASE MODEL

While some recent papers have been published with regards to the modeling of fuel cell humidifiers containing gas flows in the tube and shell-sides of the membrane, few have discussed the effects of two-phase phenomena that often, if not always, exist during normal operation. In Chen, et al's [1], and Park's [20] paper, the active fluids on each side of the membrane within the humidifier are air and vapor with the water activity and heat transfer coefficient reflective of such a situation. Of course, another relevant phenomenon of interest is the existence of both water *and* vapor within the shell-side flow of the humidifier that occurs either as a result of condensation on the membrane tubes or due to water droplet transport from the outlet of the fuel cell as a byproduct of its

operation. This additional consideration causes the heat and vapor transfer on each side of the membrane to be calculated in an alternative manner, which in most cases is a more realistic scenario. However, because the specific cause of the deposition of liquid water on the tube bundle is not easily known, its effect upon the heat and vapor transfer, rather than the reason for its existence within the humidifier, will be presented in detail. Furthermore, a technique for modeling such a scenario will also be discussed presently, with special attention paid to its effect on the external heat transfer coefficient and the external water content and activity.

3.2.1. HEAT TRANSFER

Because the fuel cell exhaust under normal operating conditions is typically near 100% humidity, there often exist some liquid water droplets from the Nafion® membrane within the stack that can deposit on the membrane tubes within the humidifier. However, also possible is the formation of condensate upon the humidifier membrane tubes that occurs as a result of temperature difference between the exhaust gas entering the humidifier and the wall temperature of the tube bank. Although both phenomena likely occur simultaneously during the operation of the device, the effect of the water formation from condensate is much more convenient to model since the deposition of water droplets not due to phase change is all but random and impossible to determine physically. Therefore, for the purpose of simplicity and modeling efficiency, the water formation upon the membrane tubes is considered to occur as a result of condensation alone while

the effect of water droplet transport from the fuel cell is included in the model, where the process of condensation dominates.

The concept behind the newly considered two-phase model is that the condensation forming on the outside of the tube bank within the humidifier eventually forms a liquid film whereby heat and mass transfer from the shell-side occur only due to liquid water, whereas the heat and mass transfer on the tube-side occur as noted in previous papers—due to vapor and air. In regards to the external conditions, the film condensation occurring on the tube walls can be modeled using correlations presented by Nusselt in his paper [27], wherein the liquid condensing on the outside of the upper tubes transfers to the lower tubes due to gravity. Although the condensation rate along the length of the tube bank may in fact be variable due to wall temperature variations lengthwise along the tubes, it is assumed that the rate is more than can be absorbed and transferred to the tube-side so that a liquid film exists at *all* locations along the tube bank.

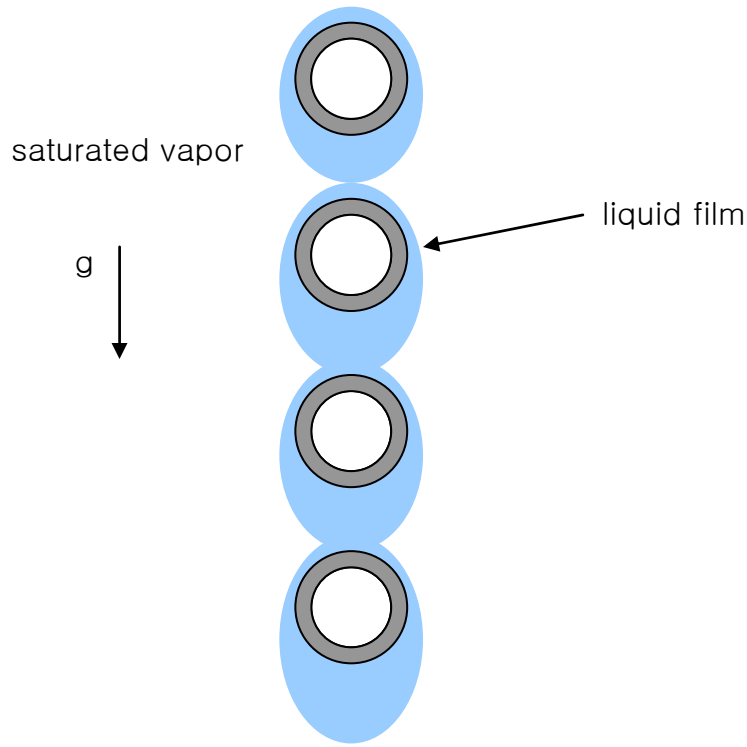

Figure 20: Nusselt's Single-Column, Two-Phase Model

The correlation, from a purely heat transfer point of view, affects the model by introducing an entirely new Nusselt number corresponding to the external liquid film. This value, which takes a slightly different form than the typical value, can be used whenever the Reynolds number of the condensation is less than or equal to 1400. Furthermore, the number corresponds to the liquid *condensing on the tubes* rather than the actual velocity of the air/vapor mixture as in the typical calculation and is given by

$$\mathrm{Re}_{cond} = \frac{4\dot{m}_{cond}}{\mu_l} \tag{3- 14}$$

where $\dot{m}_{cond}$ refers to the condensation rate and μ_l is the dynamic viscosity of the condensate. The condensation rate can be given by

$$\dot{m}_{cond} = 1.924\left[\frac{r^3 k_l^{\,3}\left(T_{sat} - T_{mem}\right)^3\left(\rho_l - \rho_v\right)g}{h_{lv}^{\,3}\upsilon_l}\right]^{1/4} \tag{3- 15}$$

in which r is the outer radius of each tube in the bank, k_l is the thermal conductivity of the liquid water, T_{sat} is the saturation temperature (or the exhaust inlet temperature), T_w is the membrane temperature, ρ_l and ρ_v are the liquid and vapor water densities, g is the gravitational constant (9.81 m/s^2), h_{lv} is the latent heat of condensation, and v_l is the kinematic viscosity of the liquid water.

Assuming that Re_{cond} is less than 1400 (it is for all conditions considered in the model) the Nusselt number can be given by

$$\overline{Nu}_{D,cond} = 0.728\left(\frac{Ra}{Ja}\right)^{0.25} \tag{3- 16}$$

in which the values of Ra and Ja refer to the Rayleigh and Jakob numbers, respectively.

The Rayleigh number is given by

$$Ra = g\frac{\left(\rho_l - \rho_v\right)\mathrm{Pr}_l\, D_o^{\,3}}{\rho_l \nu_l^{\,2}} \tag{3- 17}$$

in which Pr_l is the Prandtl number of the condensate and D_o is the outer diameter of each tube in the bank. The Jakob number is given by

$$Ja = \frac{c_{pl}\left(T_{sat} - T_{mem}\right)}{h_{lv}} \tag{3- 18}$$

where c_{pl} is the constant pressure liquid water specific heat. From the definition of the two-phase Nusselt number, the heat transfer can be given by

$$\overline{h}_{cond} = 0.728\frac{k_l}{D}\left(\frac{Ra}{Ja}\right)^{1/4} \tag{3- 19}$$

in which the diameter, D_o, is again simply the hydraulic diameter of a single tube (0.00107 m) and does not take into account the thickness of the liquid film. In his paper Nusselt applied this correlation to a bank of vertical in-line tubes whereby the condensate from the top tubes in the column would fall down towards the bottom tubes due to gravity and make the film thickness larger for the bottom tubes (see Figure 21). This effect makes necessary a modification to the overall heat transfer coefficient found in Equation (3-19) so that a new, overall heat transfer coefficient can be applied to a column of tubes given by

$$\bar{h}_{cond} = 0.728 \frac{k_l}{ND_o} \left[\frac{g(\rho_l - \rho_v)(ND_o)^3 h_{lv}}{k_l \nu_l (T_{sat} - T_{mem})} \right]^{1/4} \tag{3- 20}$$

where N is the number of tubes in a considered column so that the heat transfer coefficient is the average value for the column.

However, the bank of tubes considered in most heat exchange devices does not consist of merely a single column of tubes. Instead, and is the case with this particular humidifier, the tube bundle more closely resembles a staggered bank in which the condensate from the top tubes does not fall directly onto a tube below it but may instead fall at an angle and may not cover a lower tube completely.

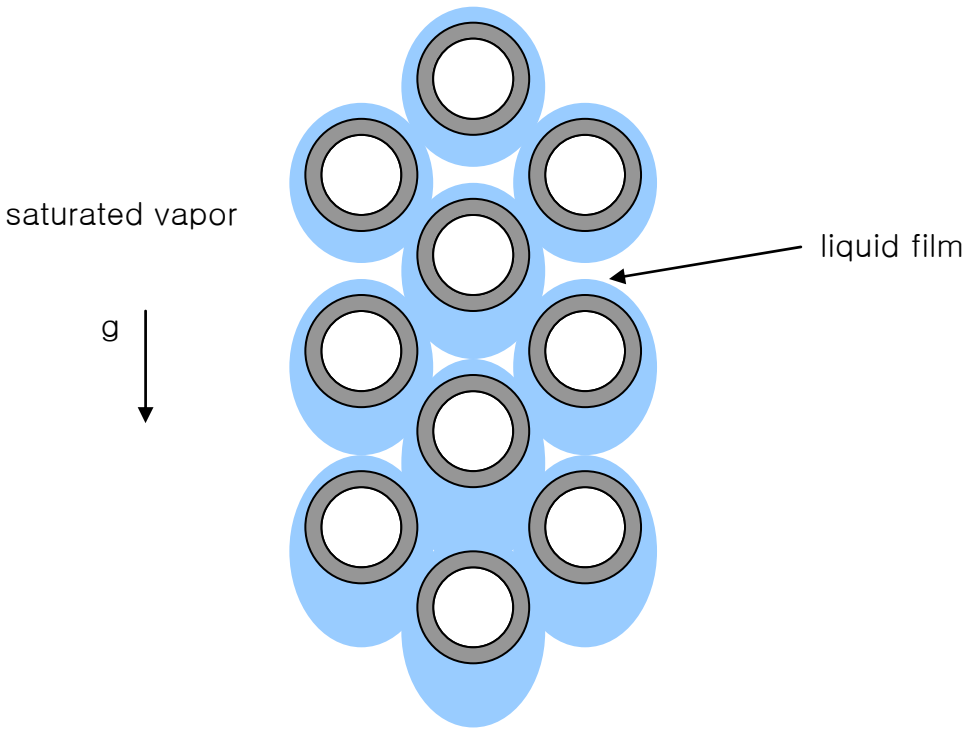

Figure 21: Kern's Two-Phase Model

In this case, the overall external heat transfer coefficient cannot be represented well with the Nusselt correlation and is better modeled using another correlation proposed by Kern [28]. The method takes into account the inundation effect of the condensate upon the tubes in the bank after first calculating the heat transfer coefficient for a single tube in the bundle. Then, the external heat transfer coefficient for the entire tube bank can be found by

$$\bar{h}_{cond,m} = \bar{h}_{cond} N^{-\frac{1}{6}} \tag{3- 21}$$

where N represents the total number of tubes. While the correlation is based on empirical data and should not be taken as absolute, it is noted that some tuning of the coefficient in the Nusselt correlation can be done so that a curve fit with experimental data can be

achieved for the purpose of modeling. This is due to the fact that in some situations the effect of splashing or non-uniform condensation may become large [22]. In fact, Selin [30] noted that a value of 0.61, rather than 0.728, in Nusselt's correlation gives better heat transfer results in most cases. In this study, the value corresponding to the best fit with experimental data was 0.5, but for other humidifier types the value may be larger or smaller.

3.2.2. VAPOR TRANSFER

Not only does the two-phase consideration of the new model have an effect on the overall heat transfer, but it also changes the characteristics of the vapor transfer as well, which, from previous understanding of the vapor exchange process in the humidifier, is closely related to the temperature. From Section 2.3.5., the boundary water content on each side of the membrane is affected by the water activity, which is a function of the temperature-dependent saturation and vapor pressures. Still, the temperature is mostly relevant to calculating *outlet* conditions of the humidifier and a more important effect to the actual transfer of vapor is the boundary water content value that results from the existence of liquid water on the shell-side. In his paper [16], Zawodzinski notes that the presence of liquid water, in the form of droplets or a film, causes the water content on the shell-side to be higher than what is considered in Park's paper. When only air and vapor exist in a certain channel the corresponding water content has a maximum value of 14.4, in which case the air in the control volume would be at saturation [20].

However, due to the condensation assumed in the new two-phase model, the flow on the outside of the membrane is actually above saturation so that the amount of water

that can transfer through it is higher than in the air/vapor model. To account for this fact, it is necessary to give an exhaust inlet humidity that is greater than saturation so that the vapor transfer rate will be increased to match the expected experimental outcome, which is a higher relative humidity at the wet outlet. In the case of the simulations, the exhaust inlet water activity used is 1.5, signifying that the vapor pressure in the exhaust inlet air is well above saturation so that condensation occurs. Furthermore, whenever the water activity on either side of the membrane at the inlet or outlet is above unity, the water content on that side is some number greater than 14.4. The selection of the high exhaust inlet relative humidity rather than the artificial constraint of the water content is more appropriate for matching the simulation data with the experimental data because the water content at all locations along the membrane cannot be known. Therefore, by setting the exhaust inlet humidity at 1.5, the vapor transfer is increased without losing any information to the random assumption of water activity.

An additional important factor of the two-phase modeling of the humidifier concerns the water activation energy, E_o, that was introduced in Section 2.3.5 and used in the calculation of the diffusion coefficient, D_w. The activation energy generally refers to the energy required to make a certain process occur, which, for the humidifier, is the process of the liquid changing phases and transferring across the membrane [18]. That is, in order for the vapor transfer to occur at various levels of membrane humidity, energy is consumed which should be reflected in the modeling. At any rate, the two-phase activation energy should be higher than that of the single-phase model because more energy is needed to transfer the vapor from the shell-side to the tube side. This is due to the fact that any liquid water on the shell side must undergo a phase change before being

transferred because the membrane only transfers vapor. In his paper, Dr. Park uses the well known value of 2416 that was proposed by Yeo and Eisenberg [31] for flows on either side of the membrane that contains air and vapor without any liquid water. While this seems to work well for predicting the vapor transfer under those circumstances, Chen [1] notes that a more appropriate value is available for higher water activities above 50%. In fact, in her paper, she notes that the membrane humidity was greater than 80% due to the existence of liquid on the shell side. The activation energy was experimentally found to be 7378 for that particular case, which is similar to the case of the humidifier in question, because it is modeled with the two-phase effect in mind. Furthermore, because the water condenses on the shell-side in the humidifier studied in this research, the water activity on that side is similar to the case in which there is a liquid flow rather than an air flow. Therefore, in the absence of extensive experimental data to find a unique value, the activation energy used in the two-phase model of this study is 7378 to represent the fact that extra energy is needed to transfer the water content on the shell-side to the tube-side.

3.3. PRESSURE DROP ANALYSIS

Because of the high energy efficiency required by the hydrogen fuel cell under typical operating conditions, it is of importance to attenuate any unnecessarily high power consumption from the rest of the components within the system. As such, and of interest in this paper, the energy efficiency of the humidifier with regards to the rest of the fuel cell must be evaluated to determine its specific detriment to the system's overall energy efficiency. With this in mind, the main cause of inefficiency likely to be encountered with the device (the pressure drop across the membrane) is examined to

determine whether or not it is a main detractor from the overall efficiency of the system. Although the humidifier itself has no moving parts and no electrical requirement from the fuel cell, the effect of pressure drop in the humidifier is significant because it represents an extra load on the stack indirectly from the electric blowers controlling the flow rate within the membrane. The pressure drop across the membrane is an indicator of how much power the blowers must expend to move the air throughout the shell side or tube side and can be included in the energy equation of the humidifier to determine its effect as a portion of the total energy of the device. Furthermore, pressure drop within the membrane tubes can significantly affect the material properties of the air flowing through them if it is large enough. Even so, if the pumping power of the humidifier makes up only a small percent of the total energy, then its effect is considered insignificant and can be neglected. In this study, the effect of pressure drop is not considered to be significant if the pumping power is less than or equal to around 3 percent of the overall energy of the system.

3.3.1. ESTIMATION OF PRESSURE DROP

The pressure drop in the humidifier can be estimated using a well known correlation from Incropera and Dewitt, where the membrane can be thought of as a bundle of tubes. In this modeling, the highest pressure drop within the device is likely to be exhibited by the shell side flow, in which the air travels normal to the several hundred tubes located within the membrane. However, because the tube side pressure drop is the one that will affect the material properties along the length of the device, it is investigated first here. The tube side pressure drop can be given by

$$\Delta p = \frac{f \cdot \rho \cdot V^2}{2 \cdot D} \cdot (x_2 - x_1) \tag{3- 22}$$

in which the value D is the diameter of the tubes, ρ is the density of the air, V is the fluid velocity through the tube side, x denotes the axial location along the tube, and f is the friction factor, which can be found by

$$f = \frac{64}{\mathrm{Re}_D} \tag{3- 23}$$

for fully developed laminar flow conditions. In order to achieve the highest possible pressure drop in the system, a flow rate of 200 standard liters per minute (SLPM) is chosen, which is around the upper limit that the flow meters in the test station can measure and is typical of what is likely to be seen during operation. As noted later, the internal flow is always laminar due to the extremely small hydraulic diameter of the tubes in the membrane. Furthermore, the assumption of fully developed flow in the tube side is also justified by another equation from Incropera and Dewitt [14], which determines the hydrodynamic entry length:

$$\frac{x_{fd}}{D} \approx 0.05 \cdot \mathrm{Re}_D \tag{3- 24}$$

The above equation shows that position along the tube at which fully developed flow is achieved is approximated by

$$x_{fd} = 0.05 \cdot D \cdot \mathrm{Re}_D \tag{3- 25}$$

which is around 1.77 cm in the tube axial direction. Using this value and the fact that the membrane tubes are roughly 0.254 m in length, the hydrodynamic entry length makes up less than 7 % of the total length of the tubes and can therefore be neglected in calculating

the pressure drop along the tubes. In fact this result is similar to that of the previous study in which fully developed flow was also assumed.

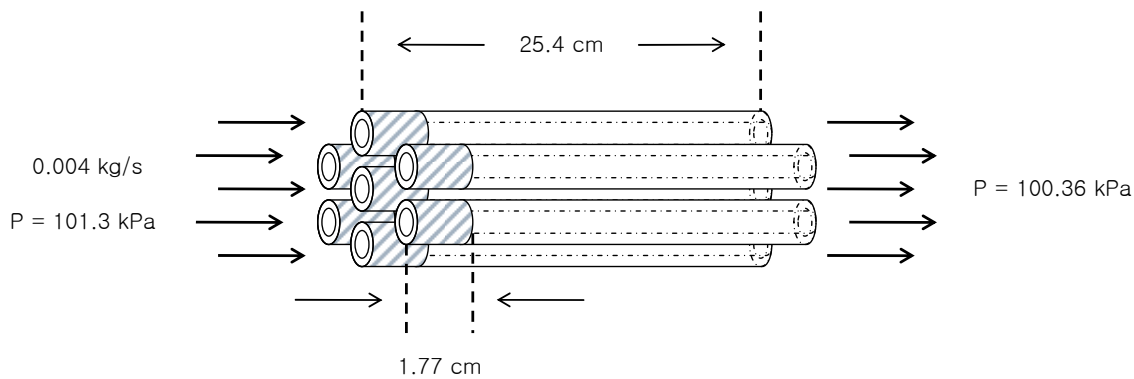

Figure 22: Multi-Tube Internal Entry Length and Pressure Drop

However, the assumption seems more justified in this case due to the correct modeling of the tube side geometry, which consists, of course, of the multi-tube arrangement. Because of the single-tube assumption of the previous model, the hydraulic diameter was around 2.7 cm and the flow was turbulent (see Table 2), affecting the calculation of the entry length. In that situation, the equation for the entry length is approximated by

$$10 \leq \left(\frac{x_{fd}}{D} \right)_i \leq 60 \qquad (3\text{- }26)$$

where, using the value of 10 for the purpose of estimation and the best possible result, the entry length is found to be around 0.27 m in length—more than the total length of the tubes. Thus, the assumption of fully developed flow is much more appropriate for the multi-tube condition, where the entry length is only a small portion of the total length of the tubes.

In order to estimate the pressure drop on the tube side, a reasonable assumption of flow rate must be made so that its effect on the phenomenon can be examined. Because the intent of the analysis is to know the influence (if any) of the pressure drop, it is logical that the highest outcome be used in the calculation to maximize its possible effect on the overall heat transfer. In this case, the maximizing property of the pressure drop is the velocity of the fluid since in the pressure drop equation its value is squared in the numerator. Although the friction factor appears to curb the pressure drop as flow rate increases, its effect is nonetheless dominated by the exponential increase in the velocity term. The velocity of the air at 200 SLPM can be calculated using

$$V = \left(\frac{2001}{\min}\right) \cdot \left(\frac{1\min}{60s}\right) \cdot \left(\frac{1}{A_c}\right) \cdot \left(\frac{m^3}{1000}\right) = 5.783 m/s \tag{3- 27}$$

in which A is the frontal area of the tubes, given by

$$A_c = 780 \cdot \pi \cdot \left(\frac{D_i}{2}\right)^2 = 0.0005764 m \tag{3- 28}$$

The Reynolds number is found to be approximately 360 using its definition, with the velocity being the result of the above equation. From here, the calculation of the friction factor can be done using the aforementioned equation, where the friction factor (f) becomes approximately 0.178. With all of the necessary values known, they can be inserted into the pressure drop equation whereby the total pressure drop per tube of the humidifier can be found by

$$\Delta p = \left(\frac{0.178 \cdot 1.205 \cdot 5.783^2}{2 \cdot D_i}\right) \cdot 0.254 = 939\ Pa \tag{3- 29}$$

in which the total length of the tube is 0.254 m as mentioned above, ρ is the density, and f is the friction factor. The total length is used in the calculation of the pressure drop because it represents the true length along which the tube side flow must travel in order to exit the membrane.

The above equation reveals the pressure drop per tube of the internal flow to be approximately 939 Pa, from atmospheric pressure (101.3 kPa). Interestingly however, the total tube side pressure drop of the system is not the product of the pressure drop per tube by the number of tubes (see Figure 22). In fact, because pressure is an intensive rather than extensive property, the total drop in pressure due to the multi-tube system is still 939 Pa, which is less than 0.93 % of atmospheric pressure.

3.3.2. PUMPING POWER

Although the pressure drop within the tubes is known for this arbitrary case, the intent is to determine the amount of power required to overcome the drop in pressure within the membrane, so the pressure loss must be translated into a quantity that can be used to estimate its effect on the total energy of the system. This can be done by estimating the power necessary to overcome the drop in pressure within the membranes and calculating its contribution to the energy equation.

$$P = 780 \cdot \Delta p \cdot \frac{V'}{780} = 3.13W \qquad (3\text{- }30)$$

where V' is the volumetric flow rate. The above equation shows that the needed power is calculated by multiplying the pressure drop by the volumetric flow rate of the air within the tubes. In addition, the number of tubes is shown to not be a factor in the calculation

because of its being an intensive property by the value of 780 in both the numerator and denominator of the equation.

It is necessary to calculate the pumping power's contribution to the energy equation to determine its significance to the system in terms of power requirements. The energy equation can be used to determine the total energy of the system by

$$E = Q - I - \left(\dot{m}_{dry} \cdot H_1 + \dot{m}_w \cdot H_w\right) + \dot{m}_{dry} \cdot H_2 \tag{3- 31}$$

in which $\dot{m}_{dry}$ is the dry mass flow rate, m_w is the vapor mass flow rate, and H_1 and H_2 are the enthalpies at the inlet and outlet of the tube side flow, respectively. For the purpose of the calculations, the test conditions from Dr. Park's paper [20] will be used to find the values in the equation as well as the heat transfer for finding the total energy of the system at those conditions. The dry mass flow rate can be found using the density of the air at 200 SLPM and the specified temperature:

$$\dot{m}_{dry} = \left(\frac{200 liters}{\min}\right) \cdot \left(\frac{1 m^3}{1000 liters}\right) \cdot \left(\frac{1 \min}{60 \sec}\right) \cdot \left(\frac{1.0335 kg}{1 m^3}\right) = 0.003445 kg/s \tag{3- 32}$$

The vapor mass transfer is found using the humidity ratios of the two flows

$$\dot{m}_w = \dot{m}_{dry} \cdot \left(\omega_2 - \omega_1\right) \tag{3- 33}$$

where W_1 and W_2 are the humidity ratios of the tube side and shell side given by

$$\omega = 0.622 \cdot \left(\frac{p_w}{p - p_w}\right) \tag{3- 34}$$

measured in kg of water per kg of dry air and where p is simply the atmospheric pressure. The value for p_{sat} is the vapor saturation pressure found from common tables whereas the value for p_w is found from the relative humidity given by

$$\phi = \frac{p_v}{p_{sat}} \tag{3- 35}$$

Using these values, $\acute{\omega}_1$ = 0.00573 kg/kg and $\acute{\omega}_2$ = 0.273 kg/kg, and the enthalpy of each flow can be calculated by

$$H = 1.006 \cdot T + \left[\omega \cdot \left(2501 + 1.805 \cdot T\right)\right] \tag{3- 36}$$

in which T is the temperature of the air in Celsius degrees for each flow. Thus, the enthalpies for the tube and shell side are

$$\begin{aligned} H_1 &= 1.006 \cdot 21 + \left[0.00573 \cdot \left(2501 + 1.805 \cdot 21\right)\right] = 35{,}674 J/kg, \\ H_2 &= 1.006 \cdot 70 + \left[0.273 \cdot \left(2501 + 1.805 \cdot 70\right)\right] = 787{,}687 J/kg \end{aligned} \tag{3- 37}$$

Finally, the vapor mass transfer is found to be 9.22×10^{-4} kg/s and the value of h_w is the enthalpy of liquid water at 21°C, approximately 1.88 kJ/kg. Now, these values can be used in the above energy equation, where the heat transfer can be estimated from the new model at 200 SLPM and at the specified conditions—approximately 170 W. The total energy rate is found to be

$$E = -170 + I - \left(0.0034454 \cdot 188{,}000 + 0.000922 \cdot 787{,}687\right) + 0.0034454 \cdot 35{,}674 \tag{3- 38}$$

where the value I is the pumping power that was found from the pressure drop of the tube side flow, found to be 3.13 W. Inserting all the values into the energy equation, the total energy rate of the system is found to be 1.417 kW into the tube side flow. Therefore, of this value, the pumping power required to overcome the pressure drop within the tubes is only around 0.22 % of the total energy of the system, and so it can be neglected.

For the shell side, a similar process can be carried out so that the pressure drop through the tube bank can be estimated. Incropera and Dewitt [14] give the pressure drop as

$$\Delta p = N \cdot \left(0.5 \cdot \rho \cdot V_{\max}^2\right) \cdot f \tag{3- 39}$$

in which N is the total number of tubes in the bank, V_{max} is the maximum velocity through the minimum tube spacing, and f is the correction factor that can be found graphically. Using the staggered tube arrangement with a minimum tube spacing of $C = 0.5 \cdot D_o$, the value for the maximum velocity is found to be 0.703 m/s. Plugging in the known quantities and noting the value for f, the pressure drop is

$$\Delta p = 780 \cdot \left(0.5 \cdot 1.067 \cdot 0.703^2\right) \cdot 10 = 2.057 kPa \tag{3- 40}$$

Using the same procedure as for the tube side, the power consumption due to the pressure drop is around 6.9 watts, where the other parts of the energy equation remain unchanged. However, even without using the enthalpy terms in the energy equation, the percentage of energy of just the heat transfer alone is only 4%. In fact, using the entire energy equation, the percentage of energy is merely 0.5%, which makes the contribution of the shell side pressure drop negligible as well.

4. DESIGN OF EXPERIMENT

This chapter is devoted to the design of experiment, which involves all of the aspects that are required to perform the actual tests on the humidifier that are needed to test the validity of the proposed model. In order to achieve the desired results from the experiments, all of the quantities are important to calculations and the data that needs to be measured have been listed (Section 4.1.). Furthermore, a detailed list of all of the materials needed in the test station for the experiments is given along with an account of how specific components were selected for the experiment based on their performance and acceptable errors. In addition, the general arrangement of all of the equipment in the test is described. Finally, the actual experimental procedure is discussed at length whereby the test plan and expected outcomes are introduced.

4.1. PRINCIPAL QUANTITIES

The main quantities that are important to the experiment are the flow rates, temperatures, and humidity involved. In all of the equations listed in the previous chapters, concerning the previous model and the current modeling techniques, these three values are the key quantities that are necessary to characterize a certain condition within the humidifier. For the input into the model, all three values are needed to be known. However, for the output of the model and during the experiment, only the humidity and

temperature are considered since it is assumed that the outlet flow rate will be very close (although not identical) to that of the inlet. For the modeling and in the experiment, temperature is measured in the SI system (degrees Celsius), while the humidity is in percent. Furthermore, the flow rate is volumetric with the units being in standard liters per minute (SLPM).

4.2. TEST STATION

The test station was provided by Schatz Energy Research Center in Arcata, California. Although its intended use is to primarily perform experiments on PEM fuel cell components, it was modified for this study to do the testing regarding the humidifier, which shares many of the same testing components as that of the PEMFC. The following sections are devoted to the physical materials employed by the test station, the selection and principles of operation of those materials, and their arrangement within the test station by which the measurements are taken.

4.2.1. MATERIALS

The physical materials involved in the experiment can be classified into three categories corresponding to their purpose within the test station: fluid/air flow devices, heat and humidification devices, and the processing units. Another may be the actual humidifier itself—it is an FC-200-780-10 gas-to-gas humidifier with a typical operating range of 50-300 SLPM and up to 80°C [14]. The unit contains 780 individual tubes

through which the dry air travels and around which the exhaust air from the fuel cell would travel.

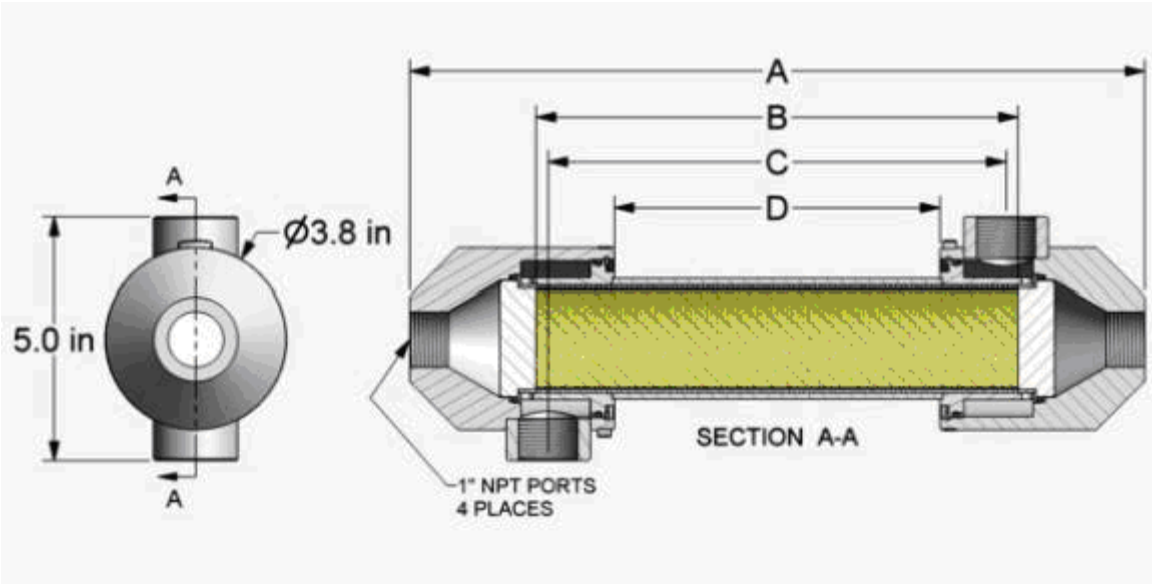

	Dimension			
Model	**A**	**B**	**C**	**D**
FC200-780-10PP	**15.25”**	**10”**	**9.5”**	**6.8”**

Figure 23: Dimensions of Humidifier [14]

4.2.1.1. AIR FLOW

The fluid/air flow devices consist of the blowers, power supplies, piping, and flow meters that are used to produce, carry, and monitor the air within the humidifier. The external and internal flow rates are controlled by three 800 W Windjammer™ 5.7” (145mm) BLDC Bypass Blowers capable of producing up to approximately 67 cubic feet per minute (>1800 SLPM) of flow under no-load conditions. They are controlled either

electronically or manually with a speed control of 0-10V DC. Although originally the blowers were controlled via the Labview™ program that was installed in the test station, they were eventually converted to be controlled manually for greater precision and range. The power supplies are standard DC components with a range of 0-30V. They were used only for the speed control, as the power for the blower actually comes from an AC outlet.

Furthermore, the piping, by which the air is contained and directed, is all PVC, which was chosen due to its resistance to heat loss and corrosion, as well as its low cost. Finally, the flow meters are two TSI 4226-01-01 gas flow meters with a range from 20-220 SLPM and an accuracy of ± 2% of reading and an output of 4-20mA. Their response time is less than 0.025 seconds for 95 % of steady state change, making them very good for determining quick changes in flow rate. Furthermore, it should be noted that the flow meters are intended to be used for *dry* gas due to the fact that high humidity may damage electrical components within the device. For this reason, the flow meters are located after the blowers but *before* the humidification and heating of the air so that no damage is incurred. This will be discussed in Section 4.2.2. in detail.

4.2.1.2. HEATING AND HUMIDIFICATION

On the other hand, the heat and humidification devices are made up of all of the components used to heat, humidify, and monitor the temperature or humidity of the gas flows during the experiments. For the shell-side flow the heating and humidification is taken care of by a 600 watt liquid-to-gas humidifier, which consists of the same membrane material as the gas-to-gas type. The device, which is controlled via the Labview™ program, works by pumping in heated water through the membrane while

simultaneously passing air through it as well. The resulting air at the outlet is capable of being fully saturated so that the exhaust inlet can mimic the flow conditions of an actual fuel cell. Moreover, the humidifier has a flow rate of 0.2-0.4 gallons per minute (0.757-1.514 SLPM) and a high temperature range of 50-65°C, although temperatures as low as 30°C can be achieved in practice.

For the tube-side channel, the only variable that is able to be controlled is the inlet temperature, which is done by using an Omegalux™ SRT051-020 heater coil capable of producing 52 watts per inch of heat. The heater coil simply uses resistance in the wire to create the necessary heat flux to the pipe, around which it is wrapped. Similar to the blowers, while it was originally controlled via the PC, the heater coil for the exhaust and tube-side flow was controlled manually via a Variac® variable voltage output for the experiments in the study. In order to measure the temperature of the shell and tube-side flows, four Omega T-type thermocouple probes are employed that have accuracies of ± 5°C. As opposed to other types of thermocouples, the T-type has a limited range (-200-350°C) but better accuracy. Furthermore, the highest temperature to be measured was no more than 65°C, so a very high temperature range was unnecessary. The probes are different from normal thermocouple wire in that they contain a protective stainless steel sheathing to protect the wires from damage in harsh environments. Nonetheless, they maintain very reasonable accuracy and typically last for long periods of time.

There were three different humidity sensors used in the experiment. For the shell-side, a Rotronic® SC05 humidity sensor and probe were employed. The sensor has an accuracy of ±2 % for 10 to 90 % R.H. and ±3 % for 0 % < RH < 10 % and 90 % < RH < 100 %. Although the response time is a little slow (4s), the repeatability is ±1% R.H., and

the response time has little effect when doing steady state tests. Furthermore, if the humidity does not change by much, the effect of the response time is diminished.

At the wet outlet, an Ohmic Instruments™ HX/HT-748 miniature probe was used. The probe is capable of measuring in temperatures up to 300°C, has a linear output from 0-1V for a range of 0-100% R.H., and an accuracy of ±2 %. However, the working range is from 10% to 90%, where the accuracy above that range is ±3% R.H. Because of the probe's small size, it was easy to locate in the wet outlet pipe so that no large obstruction of the flow resulted.

The dry inlet humidity was measured using an Omega HX71-V2 humidity sensor and transmitter. The combined devices have a total accuracy of ±3.5 % from 15 to 85% R.H. and ±4% below 15% and above 85% at 23°C. The output is 0 to 1V corresponding to 0-100% R.H. and the repeatability of the sensor is ±1%. Noticeably, this sensor is the least accurate among the humidity sensors, and is one of the reasons it is located at the dry inlet. The other significant reason for locating the sensor at that particular point is the fact that it has no software that can record the data output. But because the conditions at the dry inlet are constant throughout the tests, the ability to record is not a problem. As it turns out, the humidity at the dry inlet for a particular run rarely varied by 1% RH once the temperature and flow rate were set.

4.2.1.3. DATA PROCESSING

The final category of components used in the test station concern the processing of the temperature, humidity, and flow rate data that is measured by the devices. Because of the need to record the data, several hardware and software components were used so

that the data could be stored and averaged electronically. Moreover, for the dynamic tests, the data was recorded with time so that the response to the various inputs could be tracked and analyzed. As will be discussed further in Section 4.3.3., the purpose of the dynamic tests is to find out the time-dependent response to a dynamic step input to the system, such as a step increase in flow rate.

All of the thermocouples in the experiment were recorded with an Omega™ HH147 handheld thermocouple reader with four channels for the four thermocouples used. The resolution of the device is 0.1°C and was used in the tests to monitor the temperature at all four ports simultaneously. Furthermore, the accuracy of the reader was ±0.1% of reading for T-type thermocouples, which were used in the tests. As well as being able to monitor the temperatures, the device is capable of recording up to 10,000 data points via an RS-232 cable, by which it connects to its own recording software.

Figure 24: Thermocouple Reader

Similar to the thermocouple temperature recording, the data sets from the humidity sensors were monitored and recorded via Labview™ software installed on the computer. This is due to the fact that the sensors were not identical and could therefore not benefit from using software that was specifically designed for them. Nonetheless, the humidity, as well as the flow rate data, was still successfully recorded albeit with some extra steps needed for scaling of the sensor data. In order to collect and record all of the humidity and flow rate data in the test station, a National Instruments SCB-68 data acquisition board was used. The advantage of such a module is that it is capable of taking various analog signals, such as those from the humidity sensors and flow meters, and converting them into a measurement via a scale that the user defines. This makes the use of several different types of sensors possible, as all of them can be of different types without requiring separate software for each of the sensors.

4.2.2. ARRANGEMENT

As seen in Figure 25, the blowers (b) and power supplies (e) are located on the right side of the test station whereby the exhaust inlet flow can be humidified by the liquid-to-gas humidifier (h) and the dry inlet flow can enter from the right side. This setup gives the humidifier (a) a counter-flow configuration due to the shell-side flow entering from the top left. Note that the exhaust flow employs two blowers (X 2) as opposed to one due to the back pressure generated in the liquid-to-gas humidifier. As stated before, the in-line flow meters (c) are situated directly after the blower so that the temperature at each sensor is equal, ensuring that the same volumetric flow rate is read by

each flow meter. On the dry side, the flow passes through piping that is heated by the heater coil (d) and variable voltage output.

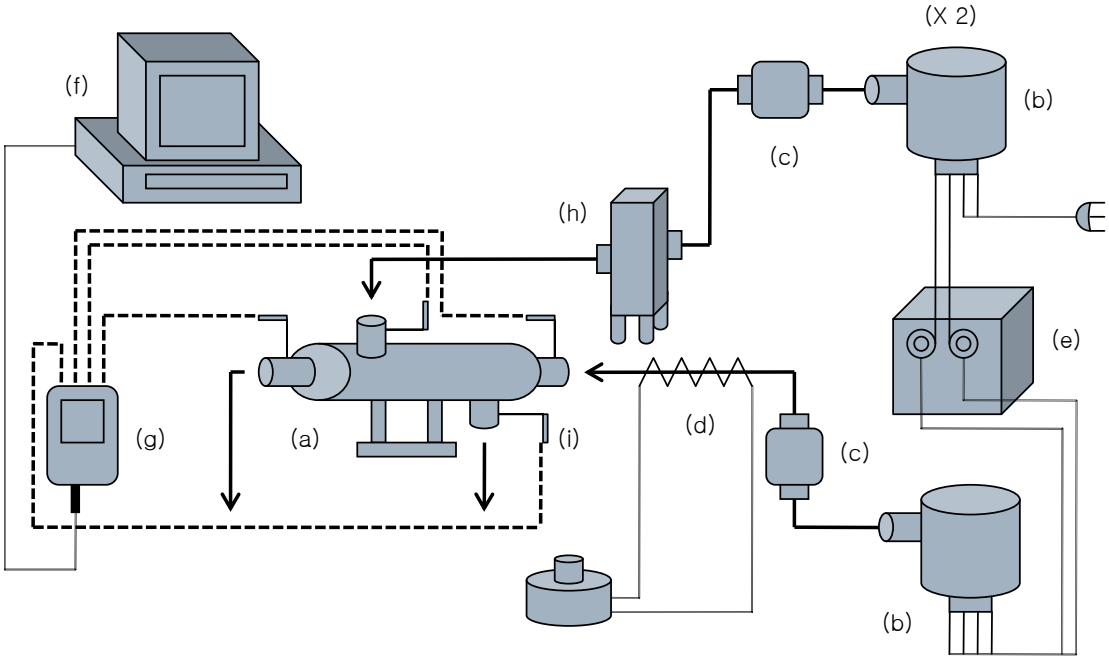

Figure 25: Layout of Test Station

The thermocouples and humidity sensors (i) are located at the inlets and outlets of the humidifier, where the temperature and humidity *directly before* entering the device can be known and so that measurement error due to heat loss may be minimized. Due to the relatively high cost compared to the temperature sensors, a humidity sensor was not placed at the exhaust outlet. However, because the humidity condition at this point is not important to the modeling of the heat and vapor transfer (which concerns the *wet outlet* conditions), it can be neglected. Finally, the thermocouples are connected to the thermocouple reader (g), which is consequently connected to the PC where all of the data is recorded. Although not shown in Figure 25, the humidity sensors are also connected to the other PC, which was not a part of the original test station.

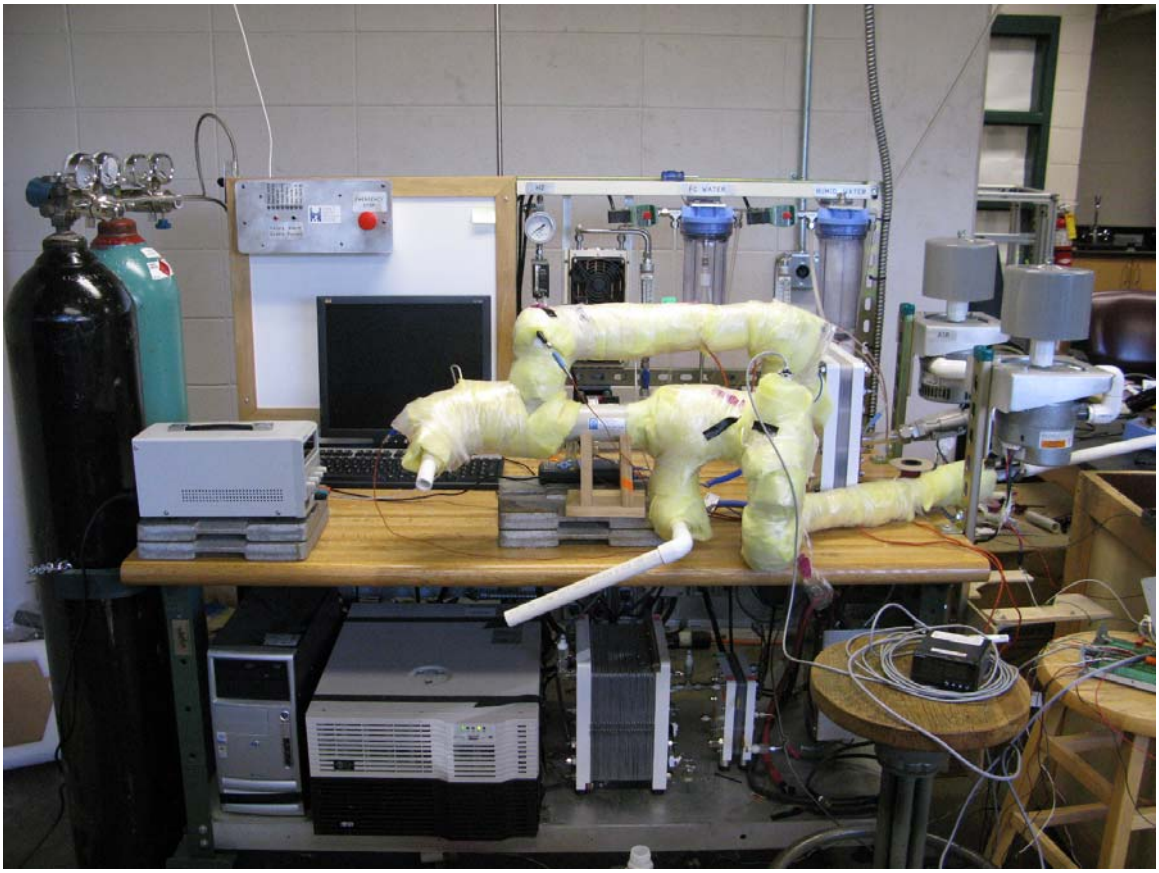

Figure 26: Test Station Layout

4.2.3. SENSOR SELECTION AND DETAILS

The correct selection of sensors in the test station is crucial to precisely determining the rate of both heat and mass transfer in the humidifier under the typical operating conditions. In this regard, care must be taken to ensure that the sensors used do not leave out any information that is necessary to achieve this goal. For measuring the temperatures at the inlet and exhaust ports of the humidifier, four T-type thermocouples were selected. Although other technologies exist for this purpose, the thermocouple is one of the most commonly used in the industry because it is relatively cheap and

effective when compared to other alternatives. The selection of the humidity sensors is more complex—various technologies are common throughout industry and high accuracy is often unachievable without very expensive sensors and calibration. Thus, some compromise was made during the selection process so that a respectable measurement could be had without incurring exorbitant costs.

4.2.3.1. THERMOCOUPLES

The main advantages of using thermocouples for temperature measurement are its reliability, durability, and simplicity when compared to some other technologies. While thermocouples do not offer the greatest accuracy of all temperature measurements, they are quite robust in the fact that they are able to be immersed in liquids and placed in other environments that may damage other types of sensors, while giving reasonably good measurements. Thus, because the sensors in the study needed to be located in locations with high humidity, the thermocouple probes and reader were selected to measure the temperatures at the inlets and outlets of the humidifier.

4.2.3.2. HUMIDITY SENSORS

There are three main technologies by which humidity measurement can be achieved: capacitive, resistive, and thermal conductive.

The *capacitive humidity sensor* uses a capacitor that changes output based on the relative humidity in its vicinity. As it turns out, the capacitance varies nearly linearly with the humidity being measured.

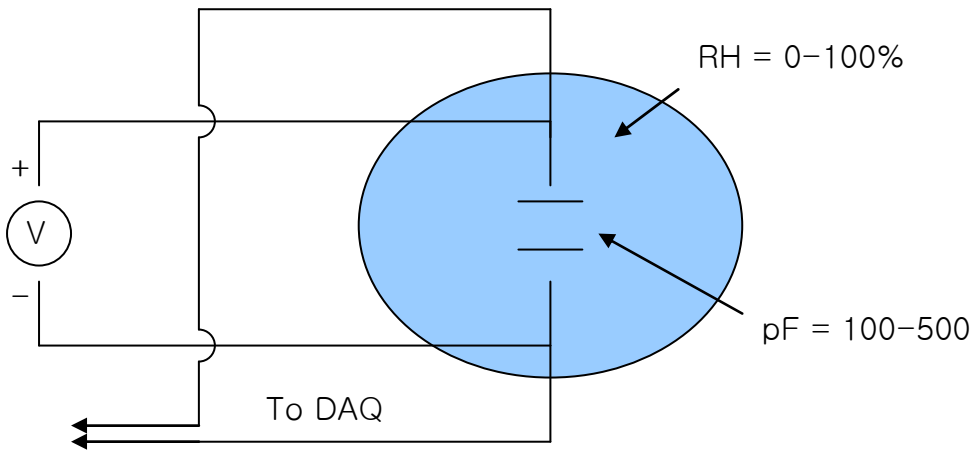

Figure 27: Circuit Diagram of Capacitive Humidity Sensor

The *resistive humidity sensor* works in a similar manner—the sensor absorbs water depending on the local humidity whereby the resistivity of the material is changed and the voltage output also changes. However, unlike the capacitive sensor, the resistive sensor's output is often nonlinear, resulting in an inverse exponential relationship with humidity (electrical conductivity increases geometrically with humidity).

Lastly, the *thermal conductivity humidity sensors* use a DC bridge circuit with two thermistors to output a voltage that is proportional to the local humidity. One of the two thermistors is located in a sealed chamber containing dry nitrogen while the other is exposed to the ambient air. During use, a current is passed through the two thermistors which creates temperatures in excess of 200ºC so that heat is transferred from them at different rates. The idea is that the thermistor located in dry nitrogen allows less heat transfer to ambient because the nitrogen around it is thermally less conductive than the humidified air near the other one. Thus, the more humidity is in the air, the larger the heat transfer rate and operating temperature is between the two thermistors. However, it

should be noted that this type of humidity sensor yields the absolute humidity of the air rather than the relative humidity like the others. This, along with its rather difficult calibration procedure led to its not being used in the experiment.

For the experiments in this study, all of the chosen sensors used the capacitive technology due to its nearly linear output, simple operating principle, and relatively low cost when compared to the others. While the long-term stability of the capacitive sensors will require calibrations every so often, the short time period involved with the tests in this paper allowed that the sensors needed to be calibrated only once. This is discussed in detail in the next section.

4.3. EXPERIMENTAL PROCEDURE

The experimental procedure refers to all of the steps that were taken to collect the required data from the tests. In this study, the procedure involved three main parts, which can be further divided into subcategories: they are the calibration of the sensors, the static, or steady-state, tests, and the dynamic tests. The calibration of the sensors involves all three main sensors (thermocouples, humidity sensors, and flow meters) after which the reading of each of the sensors should be the same or very nearly the same for the same condition (i.e. temperature). The static tests involve the measurement of the outlet temperatures and humidity with specific inlet conditions after a steady-state was reached, which is typically several minutes. These experiments tend to take longer than the dynamic tests, which are time-based and are performed to determine the response of the system to various dynamic inputs (step, ramp, etc.)

4.3.1. CALIBRATION OF SENSORS

4.3.1.1. THERMOCOUPLES

Because the temperature measurements are critical to the measurement of the total heat transfer, the sensors were calibrated in an oil bath using a reference thermocouple as the known temperature. The temperature of the oil bath was varied so that the temperature output of the four thermocouples could be graphed as a function of input temperature of the reference thermocouple. Then, using the values from the graph, a best fit line was generated so that the output temperatures of the thermocouples are known as a function of the input temperature of the environment.

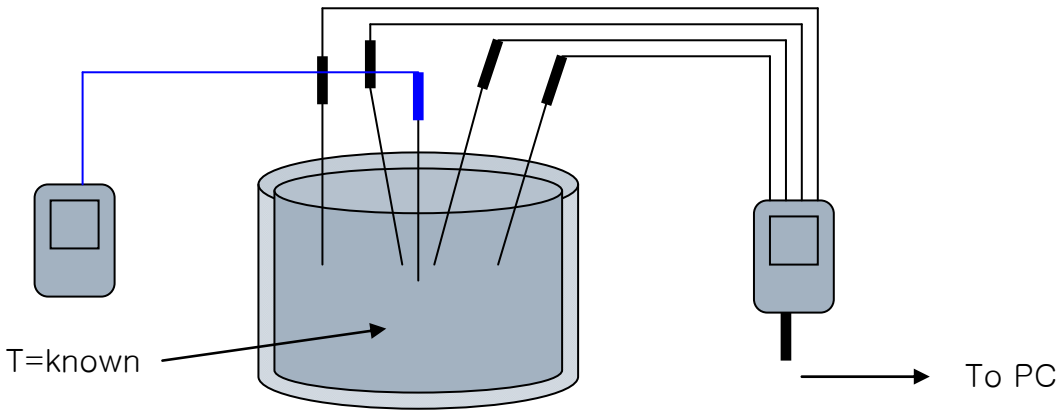

Figure 28: Calibration of Thermocouples Using Oil Bath

According to the Figure 29, the thermocouples have very linear temperature output trends, evident by the near unity or exactly unity R^2 value indicated on the chart (all of the thermocouples' graphs were similar to Figure 29). This indicates that the temperature measurement is likely to be very repeatable over the course of the

experiment for all of the thermocouples. When the appropriate temperature was reached in the oil bath, the thermocouple reader was used to take a thirty second recording with one record per second. Then, the values of each thermocouple were averaged during that time interval so that the effects of small fluctuations would be minimized.

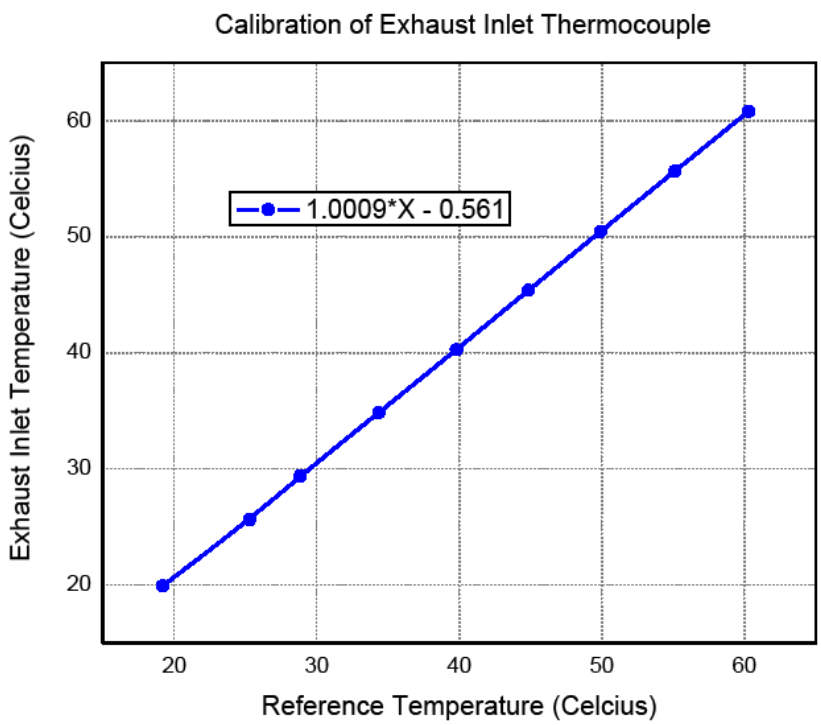

Figure 29: Equation of Line for Exhaust Inlet Thermocouple Calibration

4.3.1.2. HUMIDITY SENSORS

The procedure for calibrating the relative humidity sensors is similar to that of the thermocouples in that the sensors can be scaled to some "known" value, except that in this case the known values are much more difficult to maintain and are very sensitive to the location of the sensors during the test. The cheapest and simplest way to get a

somewhat accurate relative humidity condition is through the use of various saturated salts, which have the tendency produce relatively constant and predictable humidity values when mixed with water. The idea behind the technique is that when a certain salt is mixed with water to form a wetted salt solution the air directly above it is maintained at a specific humidity level. This happens because the different salts are able to absorb different amounts of water in the air in the vicinity of the solution. By using two different salts that have different (high and low) humidity, the sensors in the test station can be calibrated to the known humidity levels and a linear fit can made so that the sensors will accurately predict other humidity values.

In order to achieve the desired humidity, the chosen salt must be mixed with water in a container until the salt appears to be moist; only enough water to wet the salt must be added so that the salt does not become diluted by the water. Then, the container and sensors to be calibrated can be placed inside of a sealed chamber (a freezer bag was used in this case) so that equilibrium humidity can be reached after a period of time, which is typically from 6-12 hours. At this point, each of the sensors, while still in the container, can be located directly above the salt one at a time while their respective outputs are noted. The two salts used in this project were Lithium Chloride (LiCl), which gives a humidity of approximately 11.3%, and table salt (NaCl), which is capable of producing a humidity of around 75.3%, both of which depend only on the temperature adjacent to the solution.

Salt Bath	RH Value at 25°C (%)
Lithium Bromide	6.37
Lithium Chloride	11.30
Potassium Acetate	22.51
Magnesium Chloride	32.8
Potassium Carbonate	43.16
Magnesium Nitrate	52.89
Sodium Bromide	57.57
Potassium Iodide	68.86
Sodium Chloride	75.30
Potassium Chloride	84.34
Potassium Sulfate	97.30

Table 6: Humidity Corresponding to Specific Salts [32]

The voltage outputs of each of the humidity sensors in the experiment were noted and compared to the voltage outputs that should exist for the certain conditions that exist. For example, using the NaCl as the calibrating salt the relative humidity directly above the saturated solution would be 75.3 %, meaning that a sensor with an output of 0 to 1 volt should output a signal of 0.753 volts. However, due to some sensor error, the output may be less than or greater than that value so that for each predetermined condition the expected output and actual output can be graphed with respect to each other. Thus,

similar to the calibration of the thermocouples, the equation used for determining the actual values is known from the slope and intercept of the line created.

4.3.1.3. FLOW METERS

The calibration of the flow meters is not entirely different from the calibration of the other types of sensors. In fact, calibrating the flow meters is much easier than the procedure for doing so for the thermocouples, and especially for the humidity sensors. In the experiment, what was done was to take the two flow meters and connect them back-to-back on the same pipe so that air can be passed through both flow meters at the same rate. This is shown in Figure 30, where the sensors are located far enough away from one another so as to not cause any error for the flow meter that is downstream of the other. For the experiment the diameter of the pipe was 0.75”, so the sensors were located at least 7.5” from each other during the calibration.

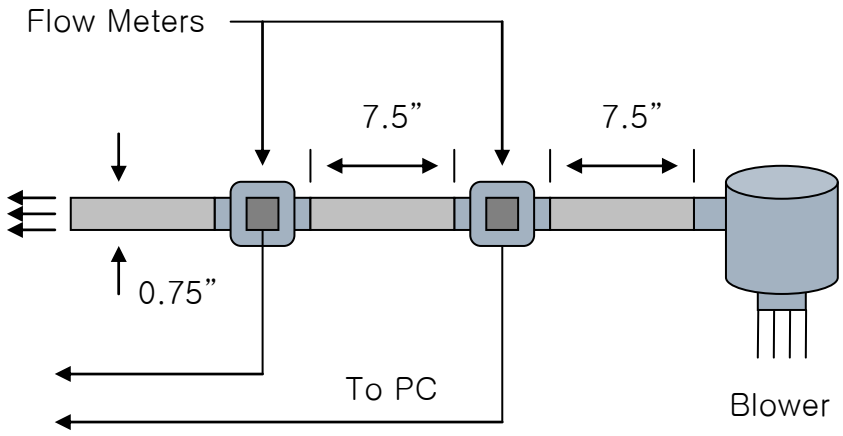

Figure 30: Flow Meter Calibration

The blower was run at a specific flow rate so that the measurements of both sensors could be taken and analyzed. Then, the difference in readings of the flow meters

was taken into account so that, during the actual experiment, the measurements would be the same for the same flow rate. As it turns out, though, the readings were nearly identical for all of the flow rates used (because they were calibrated upon initial installation of the fuel cell test station), so extra calibration was not necessary besides some scaling in Labview™ that is used to record the data.

4.3.2. STATIC TESTING

The static, or steady-state, tests are important for verifying the model in that they concern the data produced after the humidifier, in response to the inputs, has come to some equilibrium or steady state. If the model is very effective it should be able to predict the outlet conditions based on those specific inputs. Thus, what is typically done is to vary one input variable at a time while keeping all others constant and noticing the outcome. In this study, the static experiments conducted can be classified into two main groups, *passive* and *active control* simulation, in which one variable in each experiment in the group was intentionally varied—all others inputs were intended to be constant.

The concept of the passive control experiments is to simulate how the humidifier would operate in a fuel cell system when no automated control is used. The important feature of this category is that the exhaust and dry flow rates are always equal. There were two experiments performed in this group: the first involved varying the shell-side and tube-side flow rates while all other variables (inlet temperature and humidity) were held constant; the second involved varying the exhaust inlet temperature while the flow rates were held constant and equal. Although the other inputs were intended to be held constant, in actuality this was not the case. In fact, for all of the experiments, all three

inputs varied at some point due to the changing of one. Nevertheless, the steady-state outputs can still be measured and modeled with confidence, as long as a record of the inputs is kept.

For the active control experiments, a different procedure was used. Because the purpose of active control is to change the exhaust flow rate, the process of these experiments involved setting flow rates equal to each other and then keeping the tube-side flow rate constant while incrementally decreasing the exhaust flow rate. The theory is that as the exhaust flow rate is decreased, the wet outlet temperature and humidity would decrease as well, which is the purpose of the actively controlled humidifier. This procedure was performed for three different tube-side flow rates in order to see if the magnitude of the dry flow is influential to the active control of the humidity and temperature.

4.3.3. DYNAMIC TESTING

The idea in the dynamic experiments is to determine the response of the system with time to some dynamic input of one variable to determine how the actual humidifier might react when used with a fuel cell stack. While in actuality the input may be various types, such as a ramp or sine wave, the dynamic input for the tests in this study were step functions. The reason for is due to the difficulty in practice of making complicated inputs such as the sine wave. The step input lends itself to being relatively easily done with a switch or set of switches that can turn on or off simultaneously, thereby increasing or decreasing an input. Furthermore, this type of input has a practical basis, since the PEM fuel cell is likely going to experience a situation similar to a step increase in power

requirement whenever the vehicle goes uphill or demands extra speed. In that case, the flow rate would increase in a step-like fashion to deal with the higher power output of the stack. In fact, in this study only the flow rate was varied dynamically due to the fact that changes in humidity and temperature are generally very slow in comparison. Thus, two tests were performed to test the system's response to step changes in flow rate—one in which only the exhaust flow rate changed and the other in which both flow rates changed simultaneously. In both experiments, a pulse pattern was used so that the flow rates were stepped up and down at specific time intervals in order to repeat the process of interest several times.

In order to get the desired flow rate step input, several power supplies were used in conjunction with switches to get an instantaneous increase or decrease flow. Because the blowers are controlled via voltage input, the switch enabled two power supplies to be turned to two different voltages so that as the switch is thrown the voltage input to the blower(s) changed. The concept is shown in Figure 31 in which the flow rates that correspond to the particular voltage input were found before beginning the experiment.

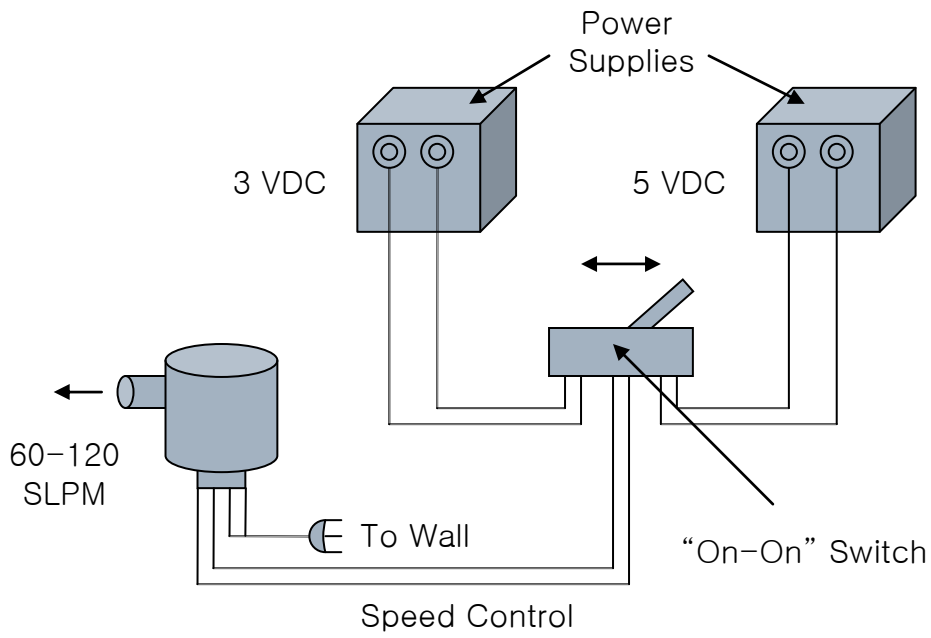

Figure 31: Step Input Setup with Switch

For the first experiment the exhaust inlet flow rate alone was varied while the tube-side flow rate was kept constant. Conversely, for the second experiment both flow rates were changed at the same time so that the flow rates were roughly equal throughout the experiment. In addition, to reduce the total number of power supplies needed for the second dynamic experiment, a potentiometer and switch were used for the exhaust in flow control while the dry flow used the above configuration. This change simply eliminated the need for four power supplies while at the same time reducing the complexity of the flow control.

5. RESULTS

In order to verify the modeling efforts of the study, the experimental results have been compared to the simulation results of the model for the same inputs. Of course, the data that is of interest in determining the strength of the model is the wet outlet temperature and humidity, which are crucial to determining the condition of the air going into the fuel cell stack. With this in mind, the main two graphical comparisons that will be made are the wet outlet temperatures and humidity for the experiments and the two-phase simulation, as well as a comparison in several cases of the experimental data versus the single-phase and two-phase model results. Although it is hoped that the simulations match the experimental data with accuracy, in practice this is all but impossible. Thus, discussions are presented with each set of data and discrepancies are explained wherever appropriate.

5.1. UNCERTAINTY ANALYSIS

Because one of the main goals of the research is to determine how accurate the model is, it is imperative that the uncertainty of the physical measurements also be known with confidence. In order to do this, an analysis of the uncertainty of the measurements is presented so that the total uncertainty of all of the components

combined can be known. Typically, for a measurement the total uncertainty of the combined devices is the root mean square of all of the component uncertainties given by

$$F_{total} = \sqrt{(F_A)^2 + (F_B)^2 + (F_C)^2} \tag{5-1}$$

in which F is the uncertainty and A, B, and C are three different components in a hypothetical case. However, there are two measurements of interest in this research, and which are presented as results—the wet outlet temperature and relative humidity. The uncertainty in wet outlet temperature can be estimated by first considering the accuracies of the thermocouples. According to their data sheets, each thermocouple has an uncertainty of ±0.5°C for the temperature range used in these experiments. Thus, the total uncertainty of all four thermocouples combined is given by

$$F_{TC,total} = \sqrt{(0.5)^2 + (0.5)^2 + (0.5)^2 + (0.5)^2} = 1°\,\mathrm{C} \tag{5-2}$$

whereby the best overall measurement of the wet outlet temperature can be known with confidence to be less than or equal to 1°C above or below the measurement. Similarly, because the three relative humidity sensors have accuracies of ±3%, ±1.5%, and ±2% the total uncertainty of the relative humidity at the wet outlet can be given by

$$F_{TC,total} = \sqrt{(3)^2 + (1.5)^2 + (2)^2} = 3.9\,\% \tag{5-3}$$

so that the best measure of humidity at that point is less than or equal to approximately 3.9% above or below the measured value. With this in mind, it is important to note that for the modeled and measured wet outlet temperature the single-phase and two-phase models are within the uncertainty of the measured values. However, in the modeling of the wet outlet relative humidity, the two-phase model is most often within the uncertainty

of the measured values, while the single-phase model is most often outside of the measured values' uncertainty.

5.2. STATIC EFFECTS

As noted in Sections 5.1.1.1., 5.1.1.2., and 5.1.2., the static tests show, in general, very good agreement between the model and the experimental data. Furthermore, the trend of the outlet data appears to be repeatable for the most part. However, important to note is the fact that the inlet conditions for the humidifier under subsequent runs of the same experiment were not identical to the previous one. The result of this is that the experimental conditions could not be accurately replicated, making *exact* repeatability unachievable. Still, the input conditions were approximately equal during repeated tests and therefore give similar wet outlet results. (In addition, because the two modeled variables of interest are the wet outlet relative temperature and humidity, two sample calculations have been given in the Appendix section to show how they were found. They are used in all of the wet outlet temperatures and relative humidity data points in all of the graphs listed, static and dynamic.)

Although the typical flow rate of the humidifier is in the range from 50 to 300 SLPM, the highest flow rate able to be attained in this study was 160 SLPM. This is due to the large amount of back pressure incurred by the liquid-to-gas humidifier in the exhaust gas channel. Even with two blowers used on that side, the maximum flow rate was limited to the lower flow rate. Nonetheless, while this does not include all of the testable flow range of the humidifier, it makes up the lower half of the range and is

therefore useful for determining the characteristics of the humidifier at those flow rates and the validity of the model as well.

5.2.1. SIMULATION OF PASSIVE CONTROL

5.2.1.1. VARIABLE FLOW RATE

The first experiment in the tests involved varying the shell-side and tube-side flow rates by 20 SLPM incrementally, which is useful for determining how the humidifier responds to changes in flow rates. The exhaust inlet conditions were to be set at 62°C at 40 SLPM and 100% R.H. However, as the flow rate increased to 160 SLPM, the temperature fell to as low as 47°C, while the humidity dropped to around 85%. On the other hand, the dry inlet conditions were much steadier, with the temperature staying around 30°C and the humidity near 39%. This is due to the direct control of the temperature via the heater coil that was mentioned earlier. While the humidity of the room was likely near 50% at room temperature, the humidity at the elevated temperature was in fact lower due to the higher saturation pressure.

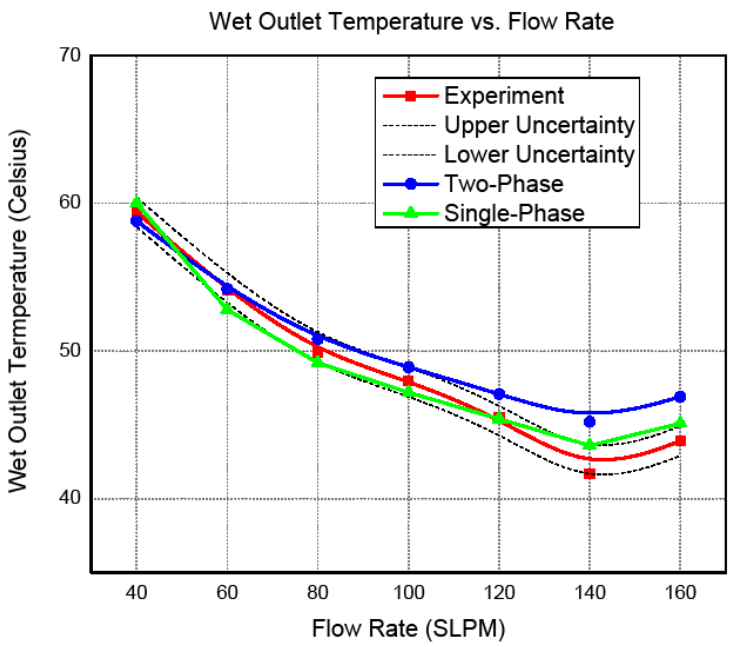

Figure 32: Temperature Plot for Variable Flow Rate Showing Uncertainty

The data in Figure 34 shows how the wet outlet temperature varied with the input flow rate. As is evident, the trend of the model is very similar to that of the experiment, which exhibited slightly lower temperatures at the higher flow rates than the model predicts. Furthermore, the uncertainty in the measured data is represented by the dashed lines above and below the experimental data. As is evident, the single-phase model appears to be inside of the uncertainty region, whereas the two-phase is not. This suggests that the single-phase heat transfer is a better predictor in this test. Nevertheless, the largest error in the two-phase model occurred at 160 SLPM where the simulated wet outlet temperature was 6.4% higher than the experimental temperature. However, at the lowest flow rate (40 SLPM), the simulation actually shows a wet outlet temperature of lower than that of the experiment. In contrast, the single-phase simulated wet outlet

temperature showed a maximum error of 4.9% at 160 SLPM. Moreover, at 160 SLPM, the graph indicates an anomalous increase in wet outlet temperature. This incident was caused by an increase in exhaust temperature (recall that the inlet conditions fluctuated unexpectedly occasionally) likely due to a change in flow rate of the liquid-to-gas humidifier. In any event, it appears that the model followed the trend reasonably.

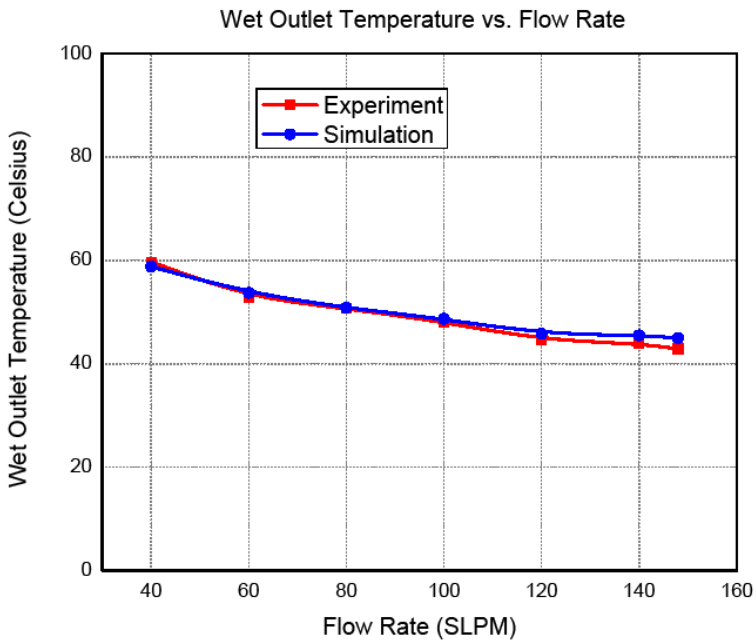

Figure 33: Temperature Plot for Variable Flow Rate (Run 2)

The main difference in the second run (Figure 33) outlet temperature data is that the "tail" at the end of the first run is not exhibited. But other than that, the graph seems to follow the same trend as in the first experiment with little discrepancy between the simulated wet outlet temperature and the experimental one. In fact, the highest difference between the expected two-phase and real values was less than 5%, showing that the heat transfer model works quite well for predicting the wet out temperature of the humidifier,

although in this case the single-phase heat transfer seems superior in predicting the wet outlet temperature.

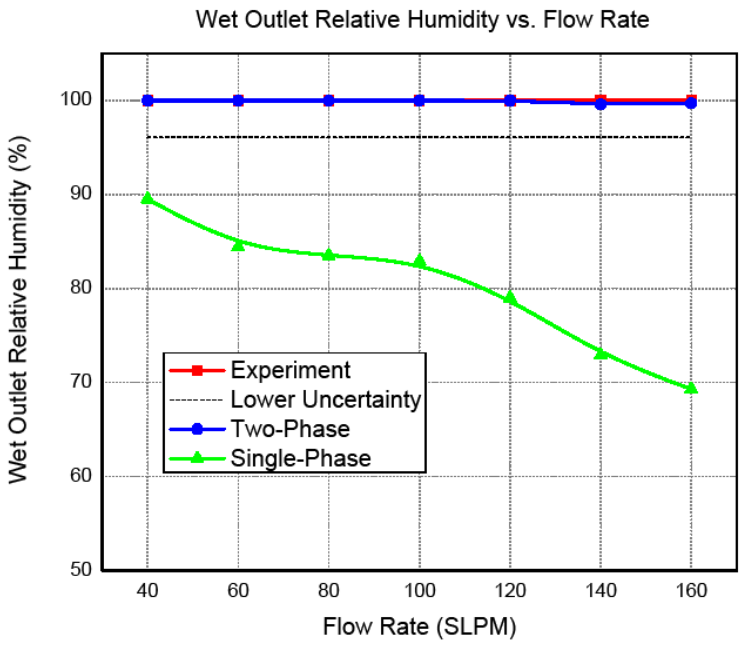

Figure 34: Humidity Plot for Variable Flow Rate Showing Uncertainty

The real difference of the single-phase and two-phase model is shown when analyzing the wet outlet humidity. In Figure 34, the agreement between the two-phase predicted wet outlet and the experimental data was excellent, with the simulation matching the experimental data very well for nearly all flow rates and the highest error of 0.4% difference at 140 SLPM and the predicted values falling well within the uncertainty range, again shown by the dashed line (recall, it was ±3.9% RH). On the other hand, the single-phase simulated wet outlet humidity was seen to not correlate very well at all to the experimental data. In fact, at a flow rate of 160 SLPM, the discrepancy was higher than 30%. It is interesting to note that the actual humidity measured at the outlet during

the experiment was always at saturation. In fact, this is the case for the wet outlet humidity throughout all of the experiments, static and dynamic. Even in situations where the model predicts humidity below saturation, the experimental data showed that the humidity did not change. The physical mechanism for this may possibly be explained by condensation within the pipe at the outlet. Because the humidity at the wet outlet may be 90% or above, the vapor pressure is very near the saturation pressure, meaning that at slightly cooler temperatures the vapor in the air could possibly condense out. It is likely that the pipe at the wet outlet is at a little lower temperature than the air within the humidifier, despite being insulated heavily. Because the humidity sensor is located near the wall of the pipe, the vapor in the very humid air may in fact begin to condense onto it causing the perception of saturation. Nonetheless, by the time the air reaches the fuel cell stack in the actual system, it is very likely that it will be at 100% humidity due to the even lower temperature from heat loss along the pipe.

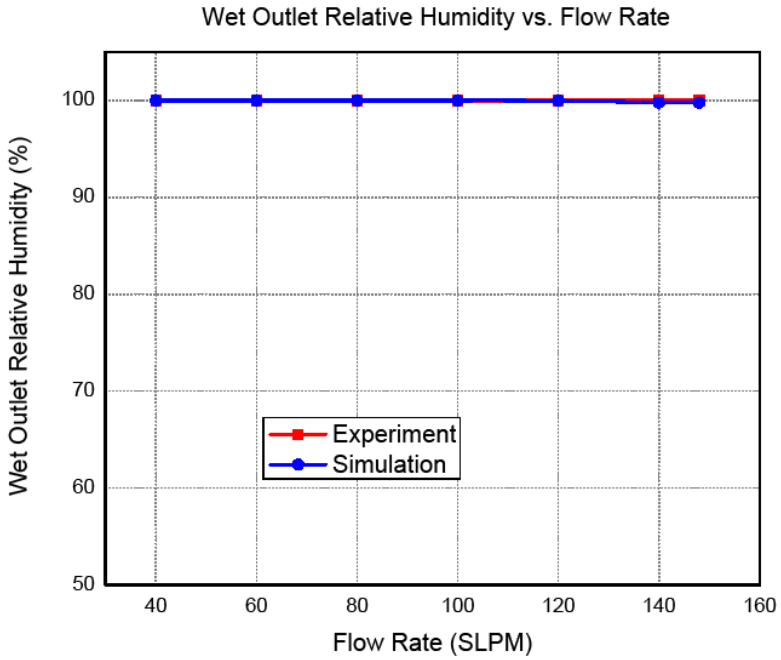

Figure 35: Humidity Plot for Variable Flow Rate (Run 2)

The data for the outlet humidity during the second run was much the same as the first, with the difference between the simulation output and the experimental values even less, at exactly 0.2% for both 140 and 160 SLPM. However, the actual humidity was again consistently 100%, which the model was unable to replicate completely near the upper flow rates.

5.2.1.2. VARIABLE EXHAUST INLET TEMPERATURE

In the second type of experiment, the inlet temperature of the exhaust inlet was varied so that the humidifier's response to changes in fuel cell exhaust temperature could be analyzed. As opposed to the first set of experiments, the flow rate for this test was kept at 100 SLPM, while the exhaust inlet temperature was decreased in increments from near

57°C to 38°C. The consequence of this pattern of inlet conditions is that exhaust inlet relative humidity was not constant during the experiment—because a secondary heater coil was used on the exhaust side to reach a higher starting temperature at 100 SLPM, the humidity entering the humidifier was decreased so that, at the high temperature of 57°C, the humidity was only 70%. The reason for this is because heating the air in this method does not add any more vapor to the system. Because the heater coil heats the air *after* the humidification in the liquid-to-gas humidifier, the saturation pressure is increased, while the vapor pressure remains the same. The result is that the perceived humidity is lower than what is desired. Despite this, the two-phase wet outlet temperature model data shows good agreement with the experimental values, except for the beginnings of variance at the upper flow rate and a maximum error of less than 11% at the highest exhaust inlet temperature.

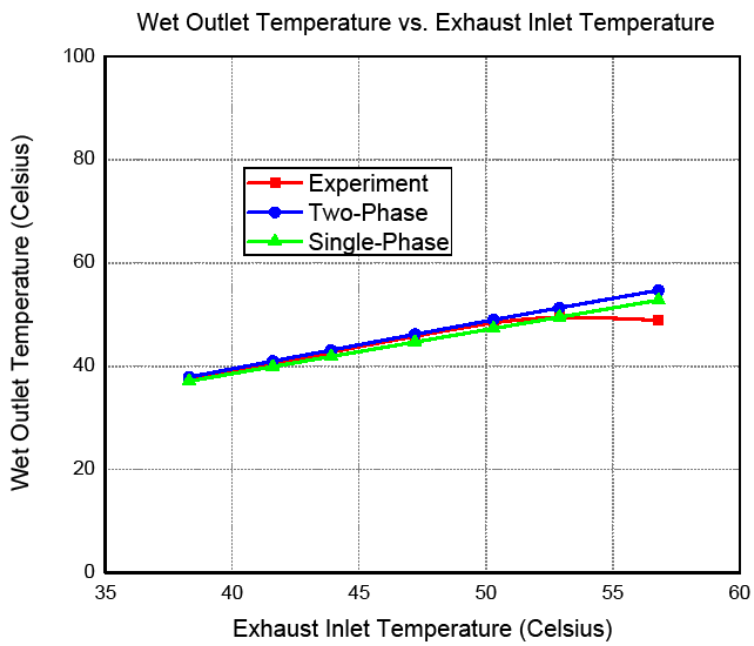

Figure 36: Temperature Plot for Variable Exhaust Inlet Temperature

Similarly, the single phase model predicts the wet outlet temperature well, again predicting slightly better than the two-phase model with a maximum difference of around 7.5% from the experimental data at the highest exhaust inlet temperature. The experimental data appears to show a decreasing wet outlet temperature as flow rate increases, while the model predicts a nearly linear trend. The reason for this likely originates in the modeling criteria.

Recall that for the tube-side channel, the Nusselt number is constant due to laminar flow. This tends to have a limiting effect on the amount of heat transfer possible for the given inputs. Because the internal Nu is constant, it does not increase as flow rate is increased, making the calculated wet outlet temperature increase in a linear fashion. Moreover, the two-phase wet outlet is slightly higher than that of the single phase probably due to the fact that the shell-side heat transfer coefficient was higher due to the existence of water on that side. Finally, the tail that is shown in the experimental wet outlet temperature is not exhibited by either of the models. The cause for this may be some phenomenon that is not completely modeled by either simulation such as splashing of the liquid film on the shell-side.

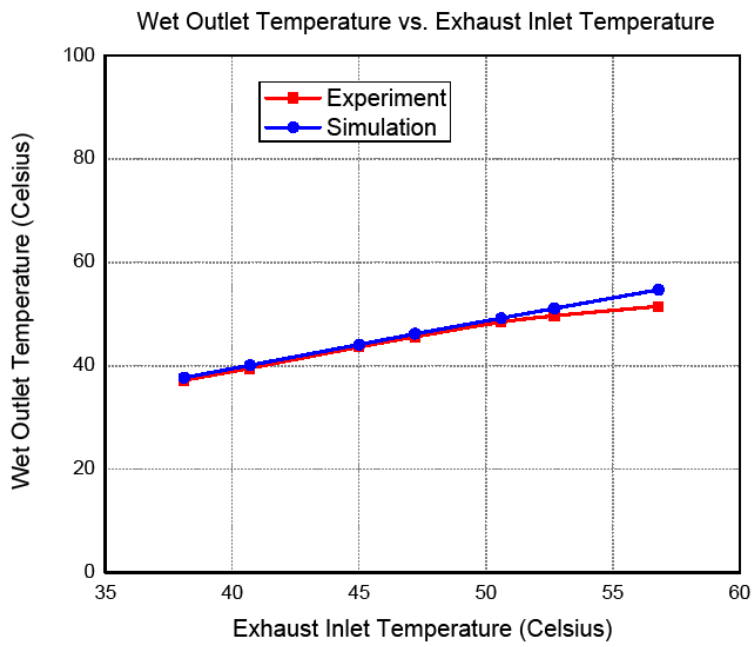

Figure 37: Temperature Plot for Variable Exhaust Inlet Temperature (Run 2)

Similar to the variable flow rate experiment the second experiment was also repeated to make sure a similar trend was exhibited. The results are that the wet outlet temperature again shows very good agreement with the experimental data. In fact, the "tail" that was noticed from the first run seems to be smaller, indicating that the conditions at that point may have been slightly different from the original time the experiment was done. The maximum error between the two-phase model and the experimental data in this case was decreased, at just under 6% difference at an exhaust inlet temperature of 56.8°C.

As for the testing of outlet humidity, the simulated two-phase wet outlet humidity under variable exhaust inlet temperature again appears to match very well with the

experimental data. Figure 37 shows a nearly identical match with the outlet test data, with only a 1% difference from the experimental data at the lowest exhaust inlet temperature.

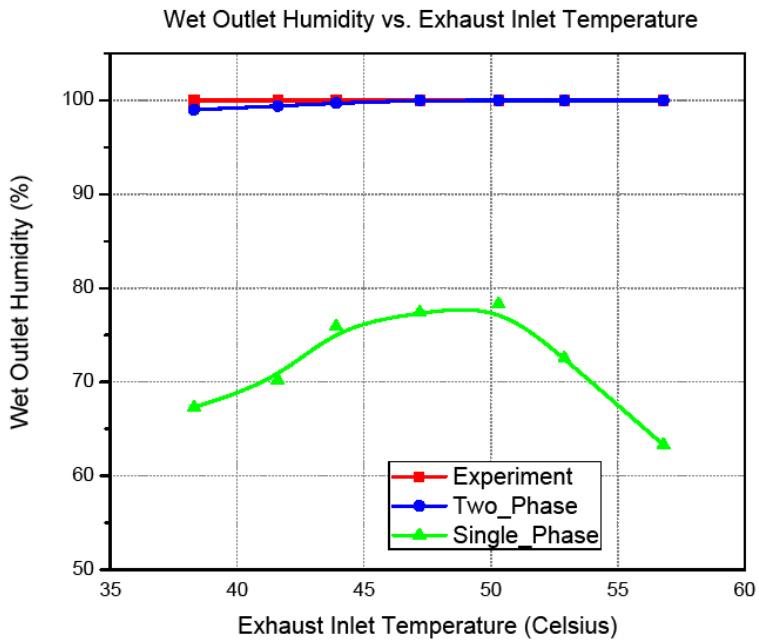

Figure 38: Humidity Plot for Variable Exhaust Inlet Temperature

Whereas the model in the simulation sometimes predicted relative humidity values above unity, in the experiment the highest humidity that could be measured was 100%. This is due to the fact that the definition of the relative humidity does not allow for values above 100% because whenever the vapor pressure of the air is higher than the saturation pressure the air would be saturated, meaning *liquid* water would exist. Thus, in the simulation of these experiments, a relative humidity above saturation at the outlet is simply rounded down to 100% since above that value no there is no experimental data for how high above saturation the air actually is. The single-phase model again proved to be unsuitable for predicting the relative humidity at the outlet with a large error of 36.7% at an exhaust inlet temperature of 56.8°C. The cause of the curve for the single-phase is

most likely due to temperature effects, whereby if the temperature was changed significantly while the vapor pressure remained constant, the humidity could see drastic changes.

Another thing to note about this figure is the fact that there was a decrease in wet outlet humidity as the exhaust inlet temperature was lowered, which would seem to not make sense. Because the temperature corresponding to 38°C is the lowest temperature in the data set, one would expect that the relative humidity is highest there. However, perhaps due to a change in water flow rate within the liquid-to-gas humidifier, the exhaust inlet relative humidity at 38°C and 42°C decreased from 98% to around 93%. While this does not seem like very much, the fact that the humidity decreased as the temperature dropped indicates that the total water amount to the system was lowered.

On the other hand, the simulated two-phase wet outlet humidity for the second run results shows nearly an identical output as that of the first run with the only difference being at the low exhaust inlet temperature. This appears to support the idea that the model data, as well as the experimental test results, are repeatable, with the largest error in this case being 1% again at the exhaust inlet temperature of 38°C.

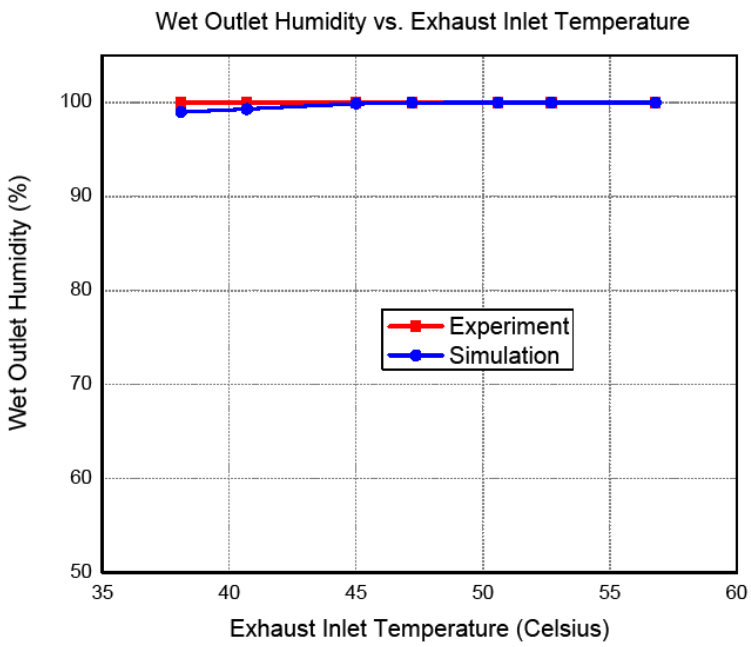

Figure 39: Humidity Plot for Variable Exhaust Inlet Temperature (Run 2)

5.2.2. SIMULATION OF ACTIVE CONTROL

In regards to testing the humidifier under conditions that simulate active control, the relevant quantity that is to be varied is the external flow rate, which may be able to provide some control of the wet outlet temperature and possibly humidity. Thus, for each of the following experiments, the dry air was held at some constant, while the exhaust flow rate was stepped down in increments from the same flow rate as the dry side in the beginning. The results were then plotted similarly to the previous experiments. In addition, these experiments are still *static* tests due to the fact that their response with time is not considered—only the steady state effects of the varying temperatures is of interest here.

For the first test, the dry air flow rate was kept at a low flow of 60 SLPM, while the exhaust flow rate was dropped from that same value to 40 SLPM. Furthermore, the dry air inlet R.H. was around 38%.

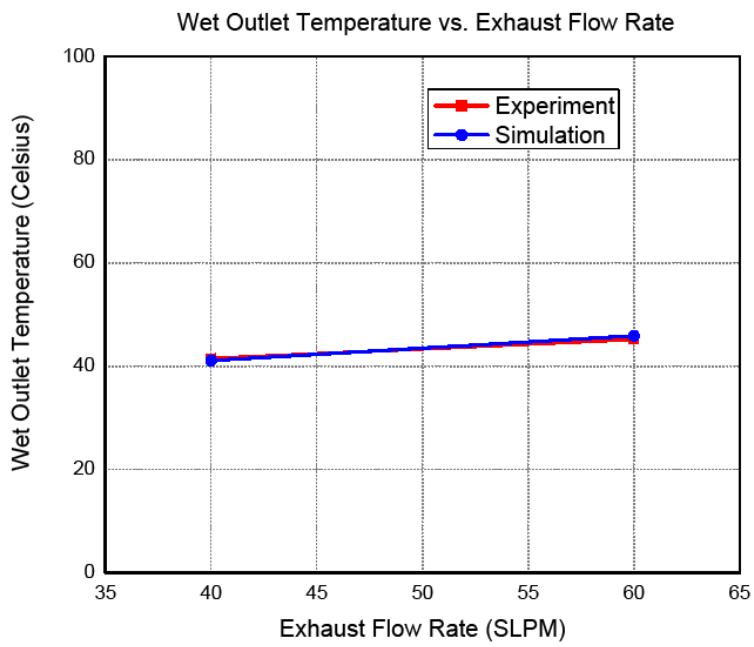

Figure 40: Temperature Plot for Variable Exhaust Flow Rate (DI = 60 SLPM)

As is evident from the figure, there was virtually no discrepancy between the experimental values and the simulated values for the single step down in exhaust flow rate, with the highest error being approximately 1.5% at 60 SLPM. However, only two results were noted, and a more extensive analysis of the response to the decrease in temperature will be seen in the subsequent graphs.

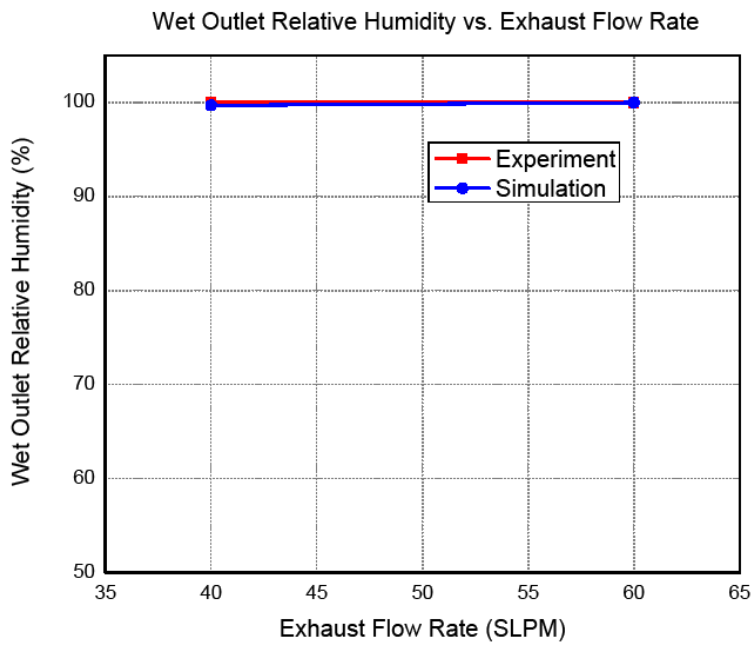

Figure 41: Humidity Plot for Variable Exhaust Flow Rate (DI = 60 SLPM)

The wet outlet humidity in the simulation and experiment also proved to agree quite well, with the simulated value reaching only 99.7% due to the drop in exhaust flow rate. It is very interesting to note that the humidity, which is intended to be changed by the change in flow rate, does not appear to be affected by the input. The fact that it does not change throughout the entire set of experiments indicates that the membrane may be saturated due to the water inundation from the exhaust side. The flow rate was increased to 100 SLPM for the second test in the group, where the exhaust inlet temperature was around 46.5°C at the beginning of the experiment. As the external flow rate decreased from 100 to 40 SLPM, the exhaust temperature did not vary by much and the humidity remained constant at 100%.

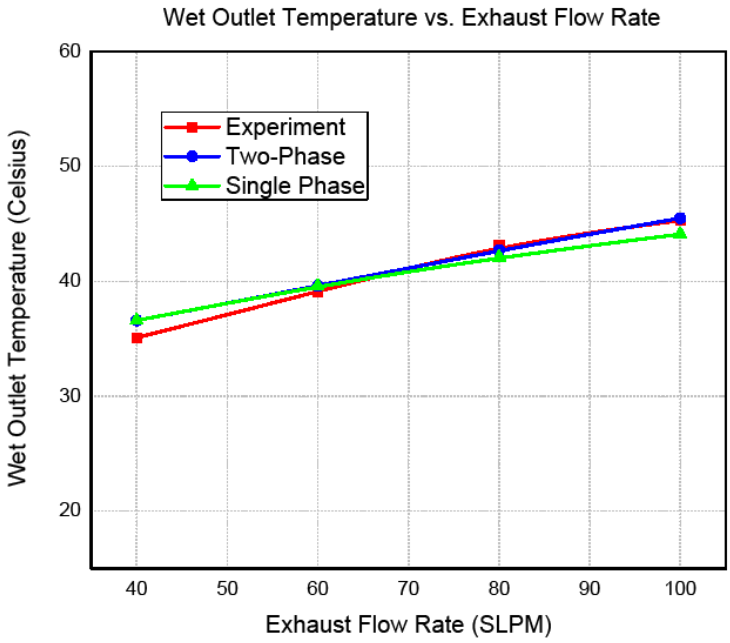

Figure 42: Temperature Plot for Variable Exhaust Flow Rate (DI = 100 SLPM)

Much the same as the previous temperature graph, the figure shows that the model agrees well with the experimental wet outlet temperature. The two-phase and single-phase wet outlet temperatures from an exhaust flow rate of 40 to 60 SLPM were almost the same, with the two-phase model matching closest from around 60 SLPM and higher to the experimental data. In the case of the two-phase prediction, the maximum error occurred at an exhaust flow rate of 40 SLPM and was 4%, which consequently was the location of the largest error for the single-phase model.

The reason for the temperature drop is due to the fact that as the exhaust flow rate is decreased, the amount of tube-side flow in comparison to the exhaust flow becomes larger. The result is that the heat from the shell-side is very effectively transferred to the tube side while the temperature of the tube side is increased less. This has to do with the

heat capacity of the air—because the mass flow rate of the tube-side air is large relative to the shell-side, the heat from the shell-side is less able to increase the temperature along the tubes. The effect is the perception of a drop in wet outlet temperature.

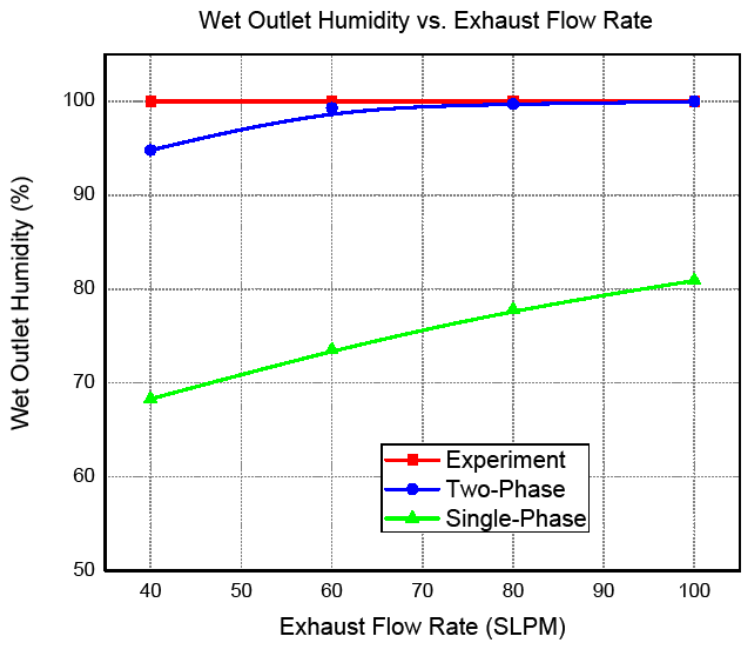

Figure 43: Humidity Plot for Variable Exhaust Flow Rate (DI = 100 SLPM)

However, the comparison of the simulation and experimental results for the wet outlet humidity was more interesting. It turns out that the two-phase model predicts the humidity will drop significantly as the shell-side flow rate is decreased, while the experimental humidity again shows no change in magnitude. In fact, the full effect of the flow rate on the simulated wet outlet humidity is not shown in this graph. In the actual results of the simulation, the expected wet outlet humidity at 100 SLPM was well above saturation and dropped significantly to around 95% at 40 SLPM. One effect that may be taking place in the actual humidifier is the humidity at that point increasing due to the

decrease in temperature from approximately 46°C to 36°C, whereby the saturation pressure would be lower. Despite the discrepancy, the overall agreement between the experimental and simulated data is still very good, with an error of 12.5% at an exhaust flow rate of 40 SLPM. The single-phase model is much lower in magnitude than that of the two-phase model, with an error of nearly 32% at 40SLPM. However, it appeared to follow the same general trend as the humidity outlet of the two-phase simulation.

Finally, the last experiment in the active control simulation group was done with the dry flow rate set at 140 SLPM, while the exhaust flow rate was decreased for each data point in 20 SLPM increments. This category of experiments, in which the exhaust inlet temperature remains near 46°C, is characterized by a similar change in temperature and simulated humidity at the outlet as the previous test. However, as opposed to the previous experiment, the exhaust inlet relative humidity was 94% and 97% for the first two data points due to the higher flow of air than the others.

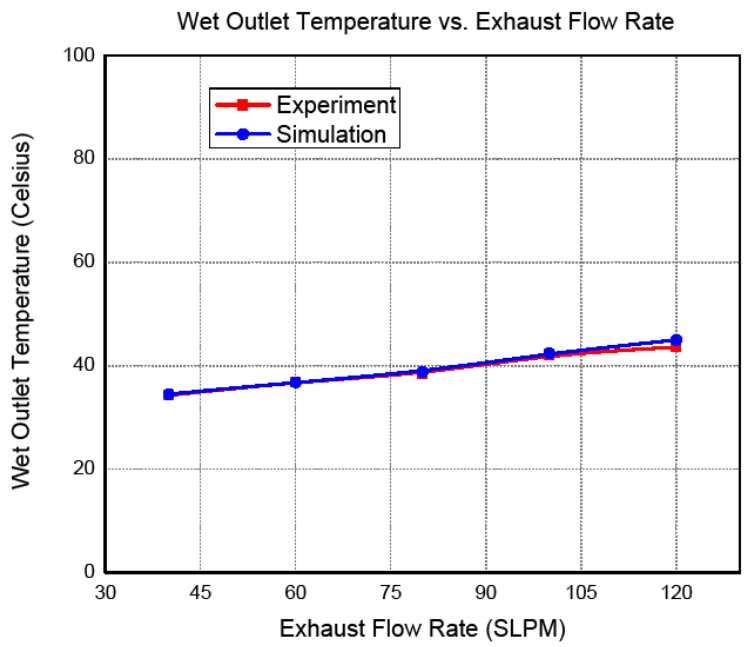

Figure 44: Temperature Plot for Variable Exhaust Flow Rate (DI = 140 SLPM)

The wet outlet temperature comparison shows a slightly different trend than the other two previous experiments. Whereas the earlier two showed larger discrepancy at the lower exhaust flow rate, the third experiment shows slight difference at the higher flow rate, near 120. Similar to Figure 33 and Figure 36, this is likely due to the increased flow causing some splashing of the liquid film on the shell-side which is not completely modeled in the two-phase simulation. However, in contrast to the other two graphs, the simulation shows near identical data points at the low flow rate of 40 SLPM. Furthermore, because the data shows no more than 3% error at 120 SLPM, the model appears to be well suited for predicting the temperatures under these circumstances.

The wet outlet humidity for the dry air flow at 140 SLPM was similar to that of the 100 SLPM case, only with slightly larger difference.

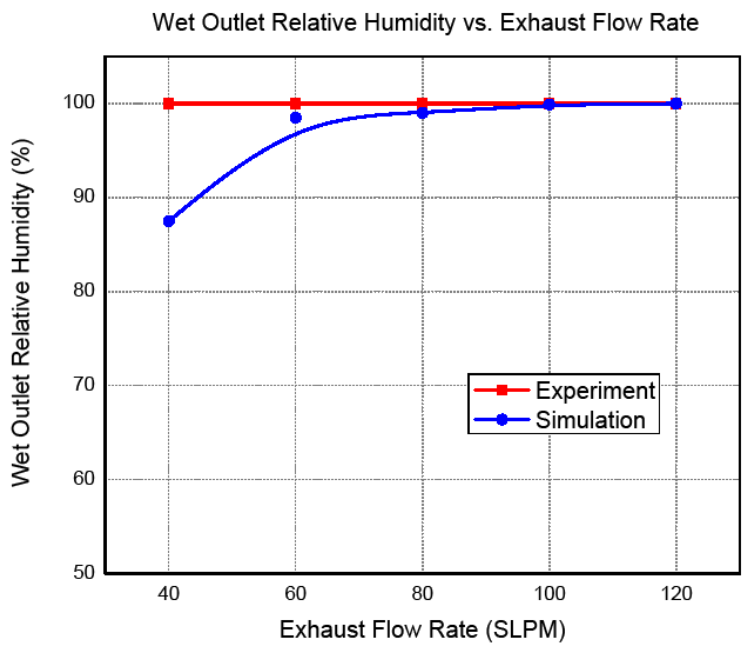

Figure 45: Humidity Plot for Variable Exhaust Flow Rate (DI = 140 SLPM)

Figure 45 shows the response of the wet outlet humidity to the change in flow rate on the shell-side. As is apparent, the simulated wet outlet humidity is even lower than that of the previous experiment in which the dry air flow rate was 100 SLPM. This can be explained due to the fact that the ratio of tube-side flow rate to exhaust-side flow rate was even higher than for the previous experiment. Thus, the model predicts, and one expects, that the wet outlet humidity would be decreased further as a result. However, there was no experimental data to support a drop in humidity for the wet outlet, with the magnitude being 100% throughout the whole run. Nonetheless, even with the larger discrepancy, the magnitude of the difference between the simulation and experiment was only 13%

5.2.3. DYNAMIC EFFECTS

For the dynamic experiment, the dry flow rate was maintained at approximately 120 SLPM while the exhaust flow rate was stepped up and down between 70 and 120 SLPM. The idea is to allow the system enough time to approach some steady-state value before changing the flow rate again. Thus, in this experiment, 15 minutes (except for the first 5) were allowed for each flow rate and the total length of the run was one hour. Because the exhaust inlet temperature changed as the flow rate was changed, a record was kept of all of the data that could be recorded so that, when running the simulation, the record could be mapped into the inputs of the model and run.

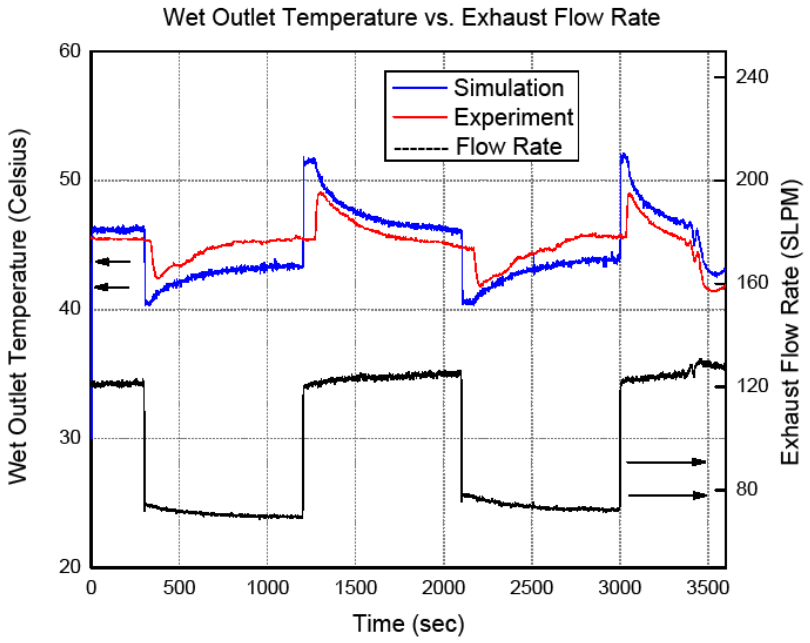

Figure 46: Dynamic Temperature Plot for Step Exhaust Flow Rate

Figure 46 shows the response of the wet outlet temperature with time corresponding to the simulation and experiment. As can be seen from the graph, the

simulation and experiment appear to follow the same trend, although the experimental data appears to be slightly delayed after the flow rate is increased or decreased and is slightly lower (or higher) in amplitude depending the point in time in which the graph is being analyzed. In contrast, the simulation data appears to react almost simultaneously to the step increase or decrease in flow rate and reaches higher amplitudes in value.

This can possibly be explained by two factors. First, the actual temperature response of the humidifier may indeed be slow due to some process within it that is not represented in the model. However, more likely is the fact that the thermocouple and reader contain some delay which makes the readings react more slowly when compared to the model. Whereas a thermocouple with an exposed junction would have the fastest response time, the type used in this study were *thermocouple probes* which, because of their metal sheathing, take longer to sense the changes in temperature. Thus, the damping effect of the wet outlet temperature results, whereby the experimental temperature takes longer to change and does not reach the same amplitude as that of the model. Unfortunately, there is no response time of the thermocouples or the thermocouple reader listed from the manufacturer. However, it is very likely that these components are causing the delay in the graph. Furthermore, it is likely that if the delay was removed from the measurement the amplitude of the experimental wet outlet temperature would be near to the simulated value. It is likely because of the delay the measured values are never able to reach the same amplitudes as the model predicts.

Moreover, one graph that illustrates the fact that the thermocouples may be to blame is the figure for wet outlet humidity as a function of time. Notice that as the flow

rate is varied, the simulated wet outlet humidity appears to change at the same time, suggesting that it did not suffer from the same slow response time.

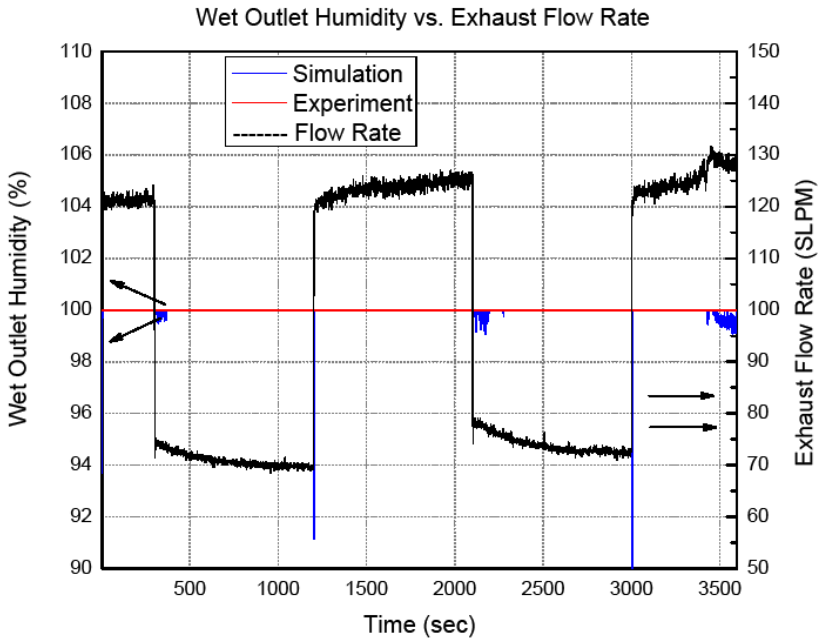

Figure 47: Dynamic Humidity Plot for Step Exhaust Flow Rate

While this figure is inherently less interesting due to the lack of data above 100% humidity, the graph is nonetheless useful in proving the validity of the model. Due to the fact that the only discrepancy between the simulation results and the experimental ones occurs at the onset of the step input, the model appears to predict the wet outlet humidity data very well.

6. GENERAL FINDINGS

The general conclusion of the study is that a new model has been proposed and developed for the purpose of modeling complex heat and vapor transfer processes in gas-to-gas membrane humidifiers. Due to the shortcomings of the single-phase modeling that has heretofore been used, a more appropriate two-phase model has been introduced in order to account for discrepancies that exist between experimental and modeled data. Whereas the prediction of experimental outlet temperatures using the two-phase scheme is equal to or moderately better than that of the single-phase model, the prediction of outlet humidity is greatly improved, with maximum errors in the prediction being less than 15% for all cases considered in the study.

For the wet outlet temperature results for the static, variable flow rate tests, the two-phase model does not appear to have a great advantage over the single-phase model, with the single-phase model being near to or within the uncertainty region of the measurements and the two-phase model results being outside of it. This indicates more than 5% error at the higher flow rates for the two-phase model. However, when looking at the wet outlet relative humidity plots, the two-phase model is obviously superior, with 1% error or less throughout the test (0.2% or less in the second run), while the single-phase model showed more than 30% discrepancy with the experiment. Likewise, for the variable exhaust inlet temperature tests, the single-phase model showed a better

agreement with the experimental data, with a maximum discrepancy of only 7.5%, whereas the two-phase model showed a slightly higher 11% error at the highest exhaust inlet temperature. Still, for the wet outlet humidity results, the two-phase model showed far better agreement, with only 1% difference from experimental data at the low exhaust inlet temperature while the single-phase model showed more than 36 % error.

When simulating the active control experiments, the wet outlet predicted temperature by the two-phase model with the dry flow rate at 60 SLPM appeared to have nearly identical values with the experimental data, with the discrepancy less than 2% at 60 SLPM. Similarly, the wet outlet predicted humidity of the two-phase model was within 1% of the experimental value. For the same experiment at 100 SLPM, the predicted wet outlet temperature of the two-phase and single-phase models was within 4% of experimental values, showing that they were almost equal in regards to predicting temperature. For predicting the wet outlet relative humidity, however, the two-phase model again proved to be the best, with its largest error being at 5% from experimental values, while the single-phase model showed approximately 32% for the same conditions. Finally, when the dry air flow was set at 140 SLPM, the two-phase model showed approximately 3% error at an exhaust flow rate of 120 SLPM, whereas the maximum error in wet outlet humidity was approximately 13% at the low exhaust flow rate of 40 SLPM. This indicates that there is some phenomenon that is occurring that the two-phase model does not account for, especially at the low flow rates. However, as for the rest of the experiment, the data and the simulation appear to match up well.

Finally, for predicting the wet outlet temperature and humidity dynamic responses, the two-phase model appears to show very close agreement, especially with the experimental wet outlet temperature. It was noted, however, that the experimental values showed some delay when compared to the simulation, which does not have to deal with sensor response time. It was further noted that the experimental values, without the delay, would likely match even better with the simulation data due to the fact that the sensors would have more time to react completely to the step increase or decrease in exhaust flow rate. However, without repeated experiments, this claim cannot be fully verified. For the wet outlet humidity dynamic response, however, the simulation proved to not show any interesting dynamic phenomenon, with some humidity variation occurring just after the step increase or decrease. Nonetheless, the actual output of the model appears to be within 1% or 2% in most cases, showing that it too is a good predictor of outlet conditions.

In conclusion, the two-phase humidifier model can be regarded as an alternative to the more conventional single-phase approach when conditions such as condensation or liquid inundation exist on the shell-side of the humidifier. Furthermore, while the experimental dynamic data appeared to exhibit some delay in response to step inputs, the two-phase model trend showed very good correlation throughout the length of the run, indicating that the model's use as a possible predictor of temperature and humidity time response may be possible.

7. FUTURE WORK

The future work of the study includes the perfecting of the two-phase model so that it can be applied to other types and sizes of humidifiers. In addition, it is hoped that some of the discrepancy exhibited in the model are explained through better understanding of the two-phase phenomenon that may be occurring within the device, but that is not necessarily visible.

At the forefront of these types of phenomena, and of interest in the future, is the effect of phase change from liquid to vapor on the shell-side of the membrane. Because the membrane works by transferring vapor rather than water, the liquid on the outside of the tubes must be converted into vapor in order to be carried to the tube side. However, in the process, heat is lost due to the latent heat of vaporization and it is possible that this may have some effect on the transfer of heat, and ultimately vapor, within the humidifier. Additionally, some more dynamic data is likely to be analyzed so that the exact reason for the delay in experimental temperature data is realized.

REFERENCES

[1] Ahn, J.W., "Design and Analysis of Air and Coolant Control for a Polymer Electrolyte Membrane Fuel Cell." MS Thesis Auburn University, Aug. 2007.

[2] Kumar, A. and Reddy, R.G. "Materials and Design Development for Bipolar/End Plates in Fuel Cells," Journal of Power Sources, 129 (2004) 62-67.

[3] Nguyen, T.V., White, R.E. and Water, A. "Heat Management—Membrane Fuel Cells," Journal of Electrochemical Society, 140 (8) (1993) 2178-2186.

[4] Watanabe, M., Uchida, H., et. al. "Self-Humidifying Polymer Electrolyte Membranes for Fuel Cells," Journal of the Electrochemical Society, 143 (12) (1996) 3847-3852.

[5] Ge, S.H., Li, X.G., and Hsing, I.M. "Water Management in PEMFCs Using Absorbent Wicks," Journal of the Electrochemical Society, 151 (9) (2004) 523-528.

[6] "Humidifier for Fuel Cell Using High Conductivity Carbon Foam." U.S. Patent 7147214, 12 Dec. 2006.

[7] "Compact lightweight Autothermalreformer Assembly for Automotive Applications, Fetauring Catalyst Bedformed from Cylindrical Monolithicopen-cell Foam Body to Reduce Size and Weight." UTC Fuel Cells, USA. R.R. Lesieur. US Patent 6969411, Nov. 2005 (Filed: 22 Sep. 2004).

[8] Evans, J.P. "Experimental Evaluation of the Effects of Inlet Gas Humidification on Fuel Cell Performance," MS Thesis, Virginia Polytechnic and State University Sep. 2003.

[9] Wood, D.L. III, Yi, J.S., and Nguyen, T.V. "Effect of Direct Liquid Water Injection and Interdigitated Flow Field on the Performance of Proton Exchange Membrane Fuel Cells," Electrochimica Acta, 43 (24) (1998) 3795-3809.

[10] Carlson, E.J., Kopf, J.S., Sriramulu, S. and Yang, Y. "Cost Analysis of PEM Fuel Cell Systems for Transportation," Subcontract Report Sept. 30, 2005. Cambridge, MA.

[11] Radov, M., "The Enthalpy Wheel: The Most Efficient Energy Recovery System," San Jose State University, Dec. 8, 2008.

[12] R.E. Sonntag, C. Borgnakke and G.J. Van Wylen, "Fundamentals of Thermodynamics," Sixth Ed. John Wiley & Sons, Inc., 2003.

[13] Dongmei Chen and Huei Peng. "A Thermodynamic Model of Membrane Humidifiers for PEM Fuel Cell Humidification Control," Transactions of the ASME, Vol. 127, Sep 2005, 424-432.

[14] Perma Pure, LLC. http://www.permapure.com, Oct. 2009.

[15] Zhang, L.Z. and Niu, J.L. "Effectiveness Correlations for Heat and Moisture Transfer Processes in an Enthalpy Exchanger with Membrane Cores," Journal of Heat Transfer, 124 (5) (2002) 922-929.

[16] Zawodzinski, Jr., T.A., Derouin, C., Radzinski, S., Sherman, R.J., Smith, V.T., Springer, T.E., et al. "Water Uptake by and Transport through Nafion ® 117 Membranes," Journal of Electrochemical Society, 140 (4) (1993) 1041-1047.

[17] Springer, T.E., Zawodzinski, T.A. and Gottesfeld, S. "Polymer Electrolyte Fuel Cell Model," Journal of Electrochemical Society, 138 (8) (1991) 2334-2342.

[18] Chen, D., Li, W. and Peng, H. "An Experimental Study and Model Validation of a Membrane Humidifier for PEM Fuel Cell Humidification Control," Journal of Power Sources, 180 (2008): 461-467.

[19] Chen, D. and Peng, H. "Non-Minimum Phase Behavior of PEM Fuel Cell Membrane Humidification Systems," ASME Journal of Dynamic Systems, Measurement, and Control.

[20] Park, S.K., Choe, S.Y. and Choi, S.H. "Dynamic Modeling and Analysis of a Shell-and-Tube Type Gas-to-Gas Membrane Humidifier for PEM Fuel Cell Applications," International Journal of Hydrogen Energy, 33 (2008) 2273-2282.

[21] Incropera, F. P. and DeWitt, D.P. "Introduction to Heat Transfer," Sixth Ed. John Wiley & Sons, Inc., 2007.

[22] Kayes, W.M., Crawford, M.E. and Weigand, B. "Convective Heat and Mass Transfer," Fourth Ed. McGraw-Hill, 2005.

[23] Bell, K.J. "Final Report of the Cooperative Research Program on Shell and Tube Heat Exchangers," University of Delaware Engineering Experimental Station Bulletin 5. Jan. 1963

[24] Kern, D.Q. and Kraus, A.D. "Extended Surface Heat Transfer," McGraw-Hill, Inc. 1972.

[25] Kern, D.Q., in: "Process Heat Transfer," McGraw-Hill, Inc., New York, 1950, p. 266.

[26] Zukauskas, A. "Heat Transfer from Tubes in Cross Flow," in Advances in Heat Transfer 8, ed. J.P. Hartnett and T.F. Irvine, Jr., pp. 93-160, Academic, New York, 1972.

[27] Nusselt, W. "Die Oberflachenkondensation des Wasser dampfes," Zetschrift des Vereins deutscher Ininuere, 60 (1916) 541-575.

[28] Kern, D.Q. "Mathematical Development of Loading in Horizontal Condensers," Journal of the American Institute of Chemical Engineering, 4 (2) (1958) 157-160.

[29] Murase, T., Wang, H.S. and Rose, J.W. "Effect of Inundation for Condensation of Steam on Smooth and Enhanced Condenser Tubes," International Journal of Heat and Mass Transfer, 49 (2006) 3180-3189.

[30] Selin, G. "Heat Transfer by Condensing Pure Vapors Outside Inclined Tubes," Proceedings of the International Heat Transfer Conference, University of Colorado, Boulder, CO, Part II, pp. 279-289, 1961.

[31] Yeo, S.C. and Eisenberg, A. "Physical Properties and Supermolecular Structure of Perfluourinated Ion-Containing (Nafion) Polymers," Journal of Applied Polymer Science, 21 (1977) 875-898.

[32] http://www.nkhome.com/pdfs/calkit_web05.pdf Oct. 2009.

[33] http://en.wikipedia.org/wiki/Nafion Nov. 2009

APPENDIX

The wet outlet temperatures of each of the graphs in the study are found using the heat transfer models discussed in Chapter 3. The following are sample calculations intended to show how the data points on the graphs were found. The conditions used correspond to the temperature data point found for the first run of the variable flow rate static experiments (Figure 32). In this test, the exhaust inlet conditions were as follows: T = 48.4°C, RH = 85.1%, and flow rate = 160 SLPM. The dry inlet conditions were likewise: T = 29.4°C, RH = 38.5%, and flow rate = 160 SLPM. The first step in the heat transfer model is to calculate the total heat transfer. This can be done by using Equation (2-11), which can be given by

$$\frac{1}{UA} = \frac{1}{h_i A_i} + \frac{\ln\left(D_o / D_i\right)}{2\pi L k_{mem}} + \frac{1}{h_o A_o} \tag{A-1}$$

again in which the first and third terms refer to the tube-side and shell-side flows, respectively. The values for D_o and D_i refer to the outer and inner diameters of an individual tube, which are 0.00107m and 0.00097m. The length, L, is the total length of the membrane tubes, known to be 0.254m, and the value k_{mem} is the thermal conductivity of the Nafion, taken to be 0.21 W/mK. The areas A_i and A_o are the heat transfer areas of the tube for the tube-side and shell-side, which are known by

$$A = N\pi DL \tag{A-2}$$

where N is the total number of tubes in the bank. Thus, the middle conduction term in Equation (A-1) is found to be 0.0003753 K/W, which does not change throughout the simulation for the given conditions. The tube and shell-side heat transfer coefficients can be found using the definitions of their respective Nusselt numbers. For the tube-side, Nu was assumed to be a constant 3.66, which gave the best results. Thus, h_i is given by

$$h_i = \frac{Nuk_i}{D_i} = \frac{(3.66)(0.02642)}{0.00097} = 99.69\frac{W}{m^2K} \tag{A-3}$$

in which k_i is the thermal conductivity of the dry air, which is based on the dry inlet temperature. Likewise, the shell-side two-phase h_o is found using Equations (3-19) and (3-21) whereby

$$h_o = \frac{Nuk_o}{D_o} = 780^{-1/6}\left[0.5\frac{k_l}{D_o}\left(\frac{Ra}{Ja}\right)^{1/4}\right] = 145.9\frac{W}{m^2K} \tag{A-4}$$

where 0.5 is the tunable coefficient and *Ra* and *Ja* are given by

$$Ra = g\frac{(\rho_l - \rho_v)\mathrm{Pr}_l\, D_o^{\,3}}{\rho_l \nu_l^{\,2}} = 0.07308 \tag{A-5}$$

from Equation (3-17) and

$$Ja = \frac{c_{pl}(T_{sat} - T_{mem})}{h_{lv}} = 0.01545 \tag{A-6}$$

from Equation (3-18). Both *Ra* and *Ja* are dimensionless and the quantities in their calculations can be found in lookup tables. T_{sat} in Equation (A-6) is the vapor and liquid temperature of the exhaust inlet and T_{mem} is the membrane temperature, which is the average of the inlet and outlet temperatures given by

$$T_{mem} = \frac{48.4 + 29.4 + 46.85 + 31.78}{4} = 39.1°\,\mathrm{C} \tag{A-7}$$

where the last two terms in the numerator are the wet outlet and exhaust outlet temperatures that have been found from the previous iteration of the model. The shell-side heat transfer coefficient is found by the Zukauskas Nusselt number correlation

$$Nu_D = b \cdot \mathrm{Re}_{D,\max}^{m}\,\mathrm{Pr}^{0.36}\left(\frac{\mathrm{Pr}}{\mathrm{Pr}_s}\right)^{\frac{1}{4}} \tag{A-8}$$

originally given by Equation (3-12), where *Pr* is dependent upon the exhaust inlet temperature and $Re_{D,\ max}$ is found by using the Kern cross-flow area and the mass velocity. Of course, the Kern cross-flow area was given by Equation (3-10) as

$$A_{xf} = \frac{(0.056)(0.00214)(0.254)}{0.00642} = 0.0047m^2 \tag{A-9}$$

Where the second value in the numerator is the tube spacing (assumed to be 5 times the outer diameter of a tube), the denominator is the tube pitch (half the outer tube diameter plus the tube spacing), and the last term in the numerator is the baffle spacing, assumed to be the total length of the tubes. The mass velocity is given by

$$G_m = \frac{\text{mass flow rate}}{A_{xf}} = \frac{0.003107}{0.0047} = 0.661\frac{m}{s} \tag{A-10}$$

where the mass flow rate is found from the conversion of the volumetric flow rate known at the beginning of the simulation. The value of $Re_{D,\,max}$ is then found by

$$\mathrm{Re}_D = G_m \cdot \frac{D_h}{\nu} = 0.661\frac{0.00107}{0.00001784} = 14.23 \tag{A-11}$$

Where G_m is now used in place of V, the velocity, and ν is the kinematic viscosity of the exhaust flow, a temperature dependent property. When Re_D is plugged into Equation (A-8), the shell-side heat transfer calculation can be given by

$$h_o = \frac{Nuk_o}{D_o} = \frac{(0.6422)(0.9)(14.23)^{0.4}(0.7097)^{0.36}}{0.00107} = 59.55\frac{W}{m^2K} \tag{A-12}$$

in which the denominator is again the outside diameter of an individual tube in the bank. With either the single-phase or two-phase heat transfer coefficient selected, the value of UA from Equation (A-1) can be calculated. The two-phase calculation is shown here, where

$$\frac{1}{UA} = \frac{1}{(99.69)(0.6037)} + 0.0003753 + \frac{1}{(59.55)(0.666)} = 0.04221$$

and where the value UA is 23.69. This can be multiplied by the log mean temperature difference (LMTD) for a counter-flow condition so that

$$\dot{Q} = UA\frac{(T_{o,in} - T_{i,out}) - (T_{o,out} - T_{i,in})}{\ln\left[\frac{(T_{o,in} - T_{i,out})}{(T_{o,out} - T_{i,in})}\right]} = 52.92W \tag{A-13}$$

which can be used to calculate both the wet outlet temperature and the exhaust outlet temperature. Plugging in the heat transfer into Equation (2-1), the First Law can be expressed by

$$\dot{m}_{out} H_{out} = \dot{Q} + \dot{m}_{in} H_{in} - (\dot{m}u + \dot{u}m) + \dot{m}_{trans} H_{trans} \tag{A-14}$$

which can be split into respective air and vapor terms, depending on the vapor transfer rate and the relative humidity of the air at the time. The final tube-side form is given by

$$T = \frac{\dot{Q} + \dot{m}_{a,in} c_{p,a,in} T_{a,in} + \dot{m}_{v,in} c_{p,v,in} T_{v,in} + \dot{m}_{v,trans} c_{p,v} T_{mem} - \dot{m}_{a,out} c_{p,a,out} T_{a,out} - \dot{m}_{v,out} c_{p,v,out} T_{v,out}}{m_{a,out} c_{v,a,out} + m_{v,out} c_{v,vout}} \tag{A-15}$$

so that, when all of the values are plugged in, gives $T_{i,out}$ = 46.21°C. The calculation of the shell-side outlet temperature is much the same, only mass is considered to flow *out* of the control volume, so the heat transfer and the third term in the numerator have opposite signs.

For the calculation of the wet outlet relative humidity, a similar iterative procedure is used. It is started by assigning a water content value to the tube and shell-side flows based on the relative humidity of each (recall that the assumed RH of the shell-side for the two-phase model is 1.5, or 50% above saturation). This is given by Equation (2-21)

$$\lambda_i = \begin{cases} 0.043 + 17.8a_i - 39.85a_i^2 + 36a_i^3 & 0 < a_i \le 1 \\ 14 + 14(a_i - 1) & 1 \le a_i \le 3 \\ 16.8 & a_i \ge 3 \end{cases} \tag{A-16}$$

which gives a water content of 13.2 for the tube-side and 14.96 for the shell-side. Next, each value is plugged into Equation (2-19)

$$D_{\lambda} = \begin{cases} 10^{-6} & \lambda_{mem} < 2 \\ 10^{-6} \cdot \left[1 + 2\left(\lambda_{mem} - 2\right)\right] & 2 \le \lambda_{mem} \le 3 \\ 10^{-6} \cdot \left[3 - 1.67\left(\lambda_{mem} - 3\right)\right] & 3 \le \lambda_{mem} \le 4.5 \\ 1.25 \times 10^{-6} & \lambda_{mem} \ge 4.5 \end{cases} \tag{A-16}$$

so that $D_{\lambda,I}$ and $D_{\lambda,o}$ are 0.00000125. Each value can then be inserted into the equation for the diffusion coefficient, given by

$$D_w = 1.25 \times 10^{-6} \exp\left[7378\left(\left(\frac{1}{303}\right) - \frac{1}{312.5}\right)\right] = 2.625 \times 10^{-10} \frac{m^2}{s} \tag{A-17}$$

after a conversion from cm^2/s to the above units. Next, the membrane dry density is divided by the membrane dry equivalent weight and multiplied by the water content of the tube-side, membrane, and shell-side to give

$$\frac{mol}{m^3} = \frac{1000 \frac{kg}{m^3}}{1 \frac{kg}{mol}} 13.92 = 1.392 \times 10^4 \frac{mol}{m^3} \tag{A-18}$$

where the value from each side of the membrane is added to that of the membrane and then multiplied by 2 and divided by the membrane thickness to get moles of water per m^4. However, this has no meaning until it is multiplied by the value found from Equation (A-17) to get $mol/(m^2s)$. The total water diffusion for the tube and shell-side is then found to be 0.005415 $mol/(m^2s)$ from the shell-side to the tube-side.

The diffusion can be multiplied by the membrane area (assumed to be the shell-side membrane area) to get the total mass of water diffused by the humidifier. This is given by

$$\dot{m}_v = 0.005415\frac{mol}{m^2 s} \times 0.666m^2 \times 0.018\frac{kg}{mol} = 6.491\times10^{-5}\frac{kg}{s} \tag{A-19}$$

which is the total vapor transferred from the shell-side to the tube-side. The total vapor transferred from the membrane is simply two times this, or 0.00012982 kg/s. For the tube-side, this value can be summed with the water vapor at the inlet and the water vapor at the outlet as in

$$\dot{m}_{v,total} = 0.00001889\frac{kg}{s} - 0.0001487\frac{kg}{s} + 0.00012982\frac{kg}{s} = 1.011\times10^{-5}\frac{kg}{s} \tag{A-20}$$

where the first and second terms are the inlet and outlet vapor masses (the second term is found from a previous iteration). Equation (A-20) can then be integrated to get the total vapor mass at the outlet. After this is done, the value is then multiplied by the outlet temperature (in Kelvin) and the vapor gas constant in order to give the energy of the mass in Joules. This is shown by

$$\left(1.011\times10^{-5}kg\right)\left(461.5\frac{J}{kgK}\right)\left(319.4K\right) = 1.49J \tag{A-21}$$

in which the last value on the left hand side is the temperature at the wet outlet, which was found from the aforementioned heat transfer calculations. The value from Equation (A-21) is divided by the tube-side volume

$$p_v = \frac{1.49J}{0.0001464m^3} = 10{,}170Pa \tag{A-22}$$

to get the vapor pressure at the outlet. The saturation pressure of the air at the outlet is then calculated from a fourth-order approximation, but can just as easily be interpolated from lookup tables. Nonetheless, the vapor saturation pressure at 319.4K is approximately 10,190 Pa, which is above the vapor pressure slightly. Finally, the wet outlet RH is calculated by

$$RH = \frac{p_v}{p_{sat}} = \frac{10{,}170\ Pa}{10{,}190\ Pa} \times 100 = 99.8\% \tag{A-23}$$

which corresponds to the wet outlet humidity data point in Figure 32.